Geochemistry, Geophysics, Geosystems

Supporting Information for

Slow-to-Fast Deformation in Mafic Fault Rocks on an Active Low-Angle Normal Fault, Woodlark Rift, SE Papua New Guinea

Marcel Mizera[1], Timothy Little[2], Carolyn Boulton[2], David Prior[3], Emma Watson[4], James Biemiller[5], Joseph White[6], Norio Shigematsu[7]

[1]Faculty of Geosciences, Utrecht University, Utrecht, The Netherlands.
[2]School of Geography, Environment and Earth Sciences, Victoria University of Wellington, Wellington, New Zealand.
[3]Department of Geology, University of Otago, Dunedin, New Zealand.
[4]GNS Science, Lower Hutt, New Zealand.
[5]Institute for Geophysics, Jackson School of Geosciences, University of Texas at Austin, Austin, Texas, USA.
[6]Department of Earth Sciences, University of New Brunswick, Fredericton, Canada.
[7]Research Institute Eathquake and Volcano Geology, Geological Survey of Japan, AIST.

Contents of this file

Text S1 to S10

Text S1. EDS-based Elemental Compostions of Mafic Fault Rocks (p. 4)
Text S2. Additional Backscatter Electron Images and EDS Maps of Mafic Fault Rocks (p. 8)
Text S3. EBSD Data Processing (p. 13)
Text S4. EBSD-based Fabric Strength and Grain-Size Estimates of Mafic Fault Rocks (p. 13)
Text S5. Temperature-Dependent Magnetic Susceptibility Experiment on Ultracataclasite (p. 47)
Text S6. TEM Analysis of a Mirror-like Facet on Gabbroic Clast (p. 53)
Text S7. Identification of Mineral Phases in Representative Mai'iu Fault Rocks using XRD (p. 53)
Text S8. Bulk Whole rock Major Element Compositions of Mafic Fault Rocks Using XRF (p. 63)
Text S9. Chlorite and Albite Compositions Using EPMA (p. 66)

Figures S1 to S7

Figures S1.1-1.2. EDS-based layered elemental images of polyphase clasts (pp. 4-5).
Figures S2.1-2.5. Additional Backscatter Electron Images and EDS Maps of Mafic Fault Rocks (pp. 8-12).
Figures S4.1-4.25. EBSD data for mylonites, foliated cataclasites, ultracataclasites, gouges and non-mylonitic mafic schists (pp. 22-46).
Figure S5.1. Curves of temperature versus magnetic susceptibility for ultracataclasite sample (p. 48).
Figure S5.2. Backscatter electron images of magnetite-bearing veins and clasts in ultracataclasite sample (p. 49).
Figures S5.3-5.4. EDS-spectra of magnetite-bearing veins and clasts (pp. 50-51).
Figure S5.5. EDS analysis of a single magnetite grain in the ultracataclasite matrix (p. 52).
Figure S7.1. Whole rock, Ca-saturated X-ray diffraction patterns (pp. 54-61).

Tables S1 to S8

Table S1.1. EDS-based elemental compositions of different fault rock units (p. 6).
Tables S1.2-1.3. EDS-based elemental composition (wt%) of polyphase clasts in gouge samples (pp. 6-7).
Tables S4.1-4.4. EBSD-derived grain-size statistics and fabric strengths (J-index, S-index and M-index) for actinolite (pp. 14-15), epidote (pp. 16-17), albite (pp. 18-19) and titanite (pp. 20-21).
Table S7.1. Mineral Phases in Mai'iu fault rocks determined by X-Ray Diffraction (p. 62).
Table S8.1. Chemical analyses of Mai'iu fault rock samples comprising a non-mylonitic, almost undeformed Goropu Metabasalt, a mylonite and two gouge samples (p. 64).

Additional Supporting Information (Files uploaded separately)

Table S9.1 ***(Albite_EPMA_Data.xlsx).*** Feldspar compositions in mafic mylonites and foliated cataclasites.
Table S9.2 ***(Chlorite_EPMA_data.xlsx).*** Chlorite compositions, calculated temperatures and proportions of chlorite to swelling component (X) in analysed mylonite, foliated cataclasites and chlorite veins.

Introduction

This Supporting Information provides bulk rock and mineral-specific compositional and microstructural data on metabasaltic fault rocks exhumed by the Mai'iu fault in the footwall of the Suckling-Dayman Metamorphic Core Complex. The supplementary data were obtained from several analytical techniques, including: (1) field emission gun scanning electron microscopy (FEG-SEM) including energy dispersive spectroscopy (EDS) and also electron backscatter diffractometry (EBSD) to quantify elemental compositions and crystallographic orientation data in collected fault rock samples; (2) temperature-dependent magnetic susceptibility experiments on a Bartington MS2 furnace system in order to determine the Curie temperature(s) of the constituent ferromagnetic/ferrimagnetic phase(s) and the magnetic mineralogy of an ultracataclasite sample; (3) transmission electron microscopy (TEM) to analyze the mirror polish of one fault-truncated dolerite cobble in order to describe the composition, thickness and grain-size of the shiny, fault-truncated surface, and the origin of striation on these surfaces; (4) X-Ray fluorescence (XRF) in order to determine major element bulk rock compositions of Goropu Metabasalt, a mylonite and two gouge samples; (5) X-Ray Diffractometry (XRD) to identify mineral phases in 15 fault rock samples comprising ultracataclasites and gouges; and (7) electron probe micro-analyzer (EPMA) to determine the chemical composition of chlorite and albite in mylonites and foliated cataclasites. Chlorite and albite compositions can be found in the separate files *'Chlorite_EPMA_data.xlsx'* and *'Albite_EPMA_Data.xlsx'*, respectively.

In addition to the presenting analytical results derived from these method in a series of Tables, we also present EDS-derived element and EBSD-derived phase maps; EBSD-derived pole figures showing crystallographic orientation distributions of the phases actinolite, epidote, titanite, and albite; and EBSD-derived grain-size statistics for these phases. The Supporting Information also includes optical photomicrographs and SEM imagery.

Text S1. EDS-based Elemental Compostions of Mafic Fault Rocks

Elemental compositions of whole thin section (~2x1 cm) are shown in Table S1.1. Elemental compositions of polyphase clasts in gouge samples are shown in Table S1.2 and Table S1.3. The elemental data shown in Table S1.1 of the different fault rock units indicate a decrease in sodium (Na) and an increase in potassium (K) in the ultracataclasites relative to the mylonite and foliated cataclasite samples. EDS-based elemental compositions of polyphase clasts in the gouges indicate that these clasts are similar in composition to the structurally underlying fault rocks (mylonite, cataclasite and ultracataclasite).

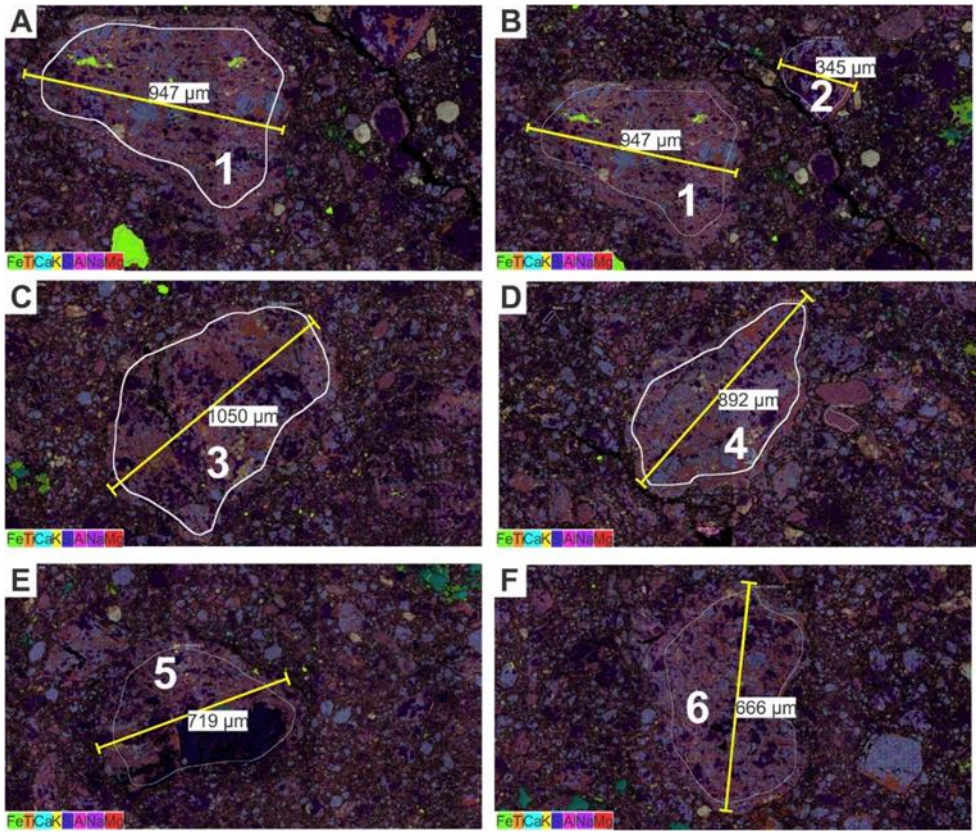

Figure S1.1. EDS-based layered elemental images of polyphase clasts embedded in fault gouge (PNG16-142A). Color scheme: iron (Fe)–green; titanium (Ti)–orange; calcium (Ca)–cyan; potassium (K)–yellow; silicon (Si)–blue; aluminium (Al)–pink; sodium (Na)–purple; magnesium (Mg)–red. Yellow scale bars in micrometers indicate diameter of polyphase clasts. A-F) Different sized polyphase clasts. EDS-based elemental compositions of these clasts are shown in Table S1.2. The elemental compositions of these clasts are similar to mylonites and foliated cataclasites. A) Polyphase clast (1). B) Polyphase clasts (1) and (2). C) Polyphase clast (3). D) Polyphase clast (4). E) Polyphase clast (5). F) Polyphase clast (6).

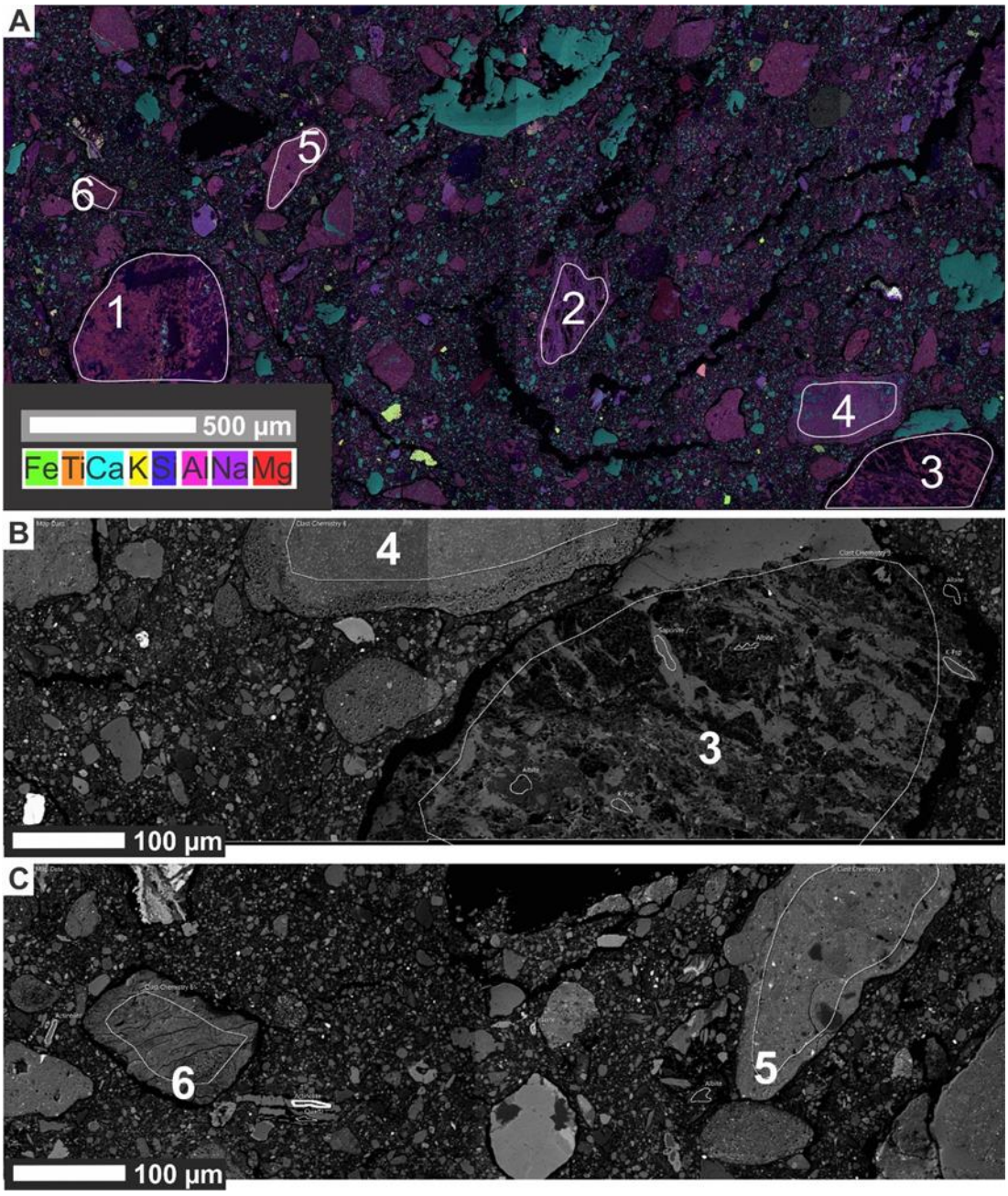

Figure S1.2. Layered elemental image and backscatter electron (BSE) images of polyphase clasts embedded in fault gouge (PNG16-142B). EDS-based elemental compositions of the analysed clasts are shown in Table S1.3. A) EDS-based layered elemental image. Clasts 1-3 are similar to mylonites and foliated cataclasites in elemental composition; clasts 4-6 are similar to ultracataclasites in elemental composition. Color scheme: iron (Fe)–green; titanium (Ti)–orange; calcium (Ca)–cyan; potassium (K)–yellow; silicon (Si)–blue; aluminium (Al)–pink; sodium (Na)–purple; magnesium (Mg)–red. B) BSE image of clast 3 and 4 (A). Clast 3 is a foliated cataclasite lithic fragment; clast 4 is a porous ultracataclasite lithic fragment. C) BSE image of clast 5 and 6 (A). Both clasts resemble the ultracataclasite in texture and composition.

Spectrum Label	Mylonite	Cataclasite	UCAT-D2	UCAT-D1	Green Gouge	Grey Gouge
	PNG16-142C	PNG16-142E	PNG16-142D2	PNG16-142D1	PNG16-142A	PNG16-142B
O	42.65	41.99	37.68	41.61	36.35	29.28
Na	2.23	2.71	0.47	0.52	2.08	0.72
Mg	4.57	3.23	4.38	4.36	3.41	3.41
Al	8.04	6.87	6.49	6.97	6.77	5.09
Si	22.55	21.14	20.26	21.31	19.13	14.68
K	0.18	0.23	4.62	5.39	0.2	1.29
Ca	8.46	9.6	4.96	5.44	6.15	7.59
Ti	0.64	0.84	1	1.04	1	0.61
Mn	0.15	0.17	0.12	0.12	0.14	0.13
Fe	7.35	7.18	7.44	7.36	8.12	6.19
Zn	0.13	0.16	0.04	0.03	0.13	0.05
Total	**96.95**	**94.17**	**87.48**	**94.16**	**83.65**	**69.27**

Table S1.1. EDS-based elemental compositions (wt%) of the different fault rock units (collected at the active Mai'iu fault trace, PNG16-142). Highlighted fields in the ultracataclasites show a strong elemental decrease (red) of Na and Ca and a strong increase (green) of K.

Green Gouge (PNG16-142A)

Spectrum Label	Clast-Chemistry 1	Clast-Chemistry 2	Clast-Chemistry 3	Clast-Chemistry 4	Clast-Chemistry 5	Clast-Chemistry 6
O	42.26	45.8	41.92	42.5	41.14	42.03
Na	1.58	5.57	2.56	1.58	1.57	2.01
Mg	3.71	1.69	3.73	3.49	3.03	3.58
Al	8.2	10.39	7.61	8.42	4.59	7.71
Si	19.27	26.14	21.18	19.43	27.25	21.34
K	0.14	0.13	0.29	0.16	0.2	0.3
Ca	8.47	3.94	6.49	8.84	4.42	7.43
Ti	1.3	0.17	1.21	1.37	0.53	1.04
Mn	0.16			0.12	0.13	0.14
Fe	10.4	5.6	8.35	9.92	6.25	8.63
Total	**96.08**	**99.42**	**93.35**	**95.84**	**89.19**	**94.19**

Table S1.2. EDS-based elemental composition (wt%) of polyphase clasts in a gouge sample (PNG16-142A), ~5 cm beneath the active Mai'iu fault plane. Analysed clasts are shown in the EDS maps of Figure S1.1 (see above).

Grey Gouge (PNG16-142B)

Spectrum Label	Clast Chemistry 1	Clast Chemistry 2	Clast CHemistry 3	Clast Chemistry 4	Clast Chemistry 5	Clast Chemistry 6
O	43.53	36.6	36.16	42.3	40.18	40.45
Na	3.73	1.13	2.73	1.31	0.66	0
Mg	3.54	3.71	3.87	1.75	4.41	6.8
Al	10.07	7.88	7.11	7.37	7.91	7.34
Si	22.52	16.69	20.66	23.45	21.74	19.65
K	0.08	0	1.49	6.19	5.66	3.88
Ca	2.39	7.38	2.1	8.07	2.01	2.59
Ti	1.02	1.33	1.21	0.57	1.06	0.74
Mn	0.16	0	0	0	0	0
Fe	7.8	7.54	5.68	3.03	9	8.67
Total	**94.84**	**82.43**	**81.22**	**94.04**	**92.63**	**90.12**

Table S1.3. EDS-based elemental compositions (wt%) of polyphase clasts in a gouge sample (PNG16-142B) immediately beneath the active Mai'iu fault plane. Analysed clasts are shown in the EDS map and SEM back-scatter image of Figure S1.2 (see above).

Text S2. Additional Backscatter Electron Images and EDS Maps of Mafic Fault Rocks

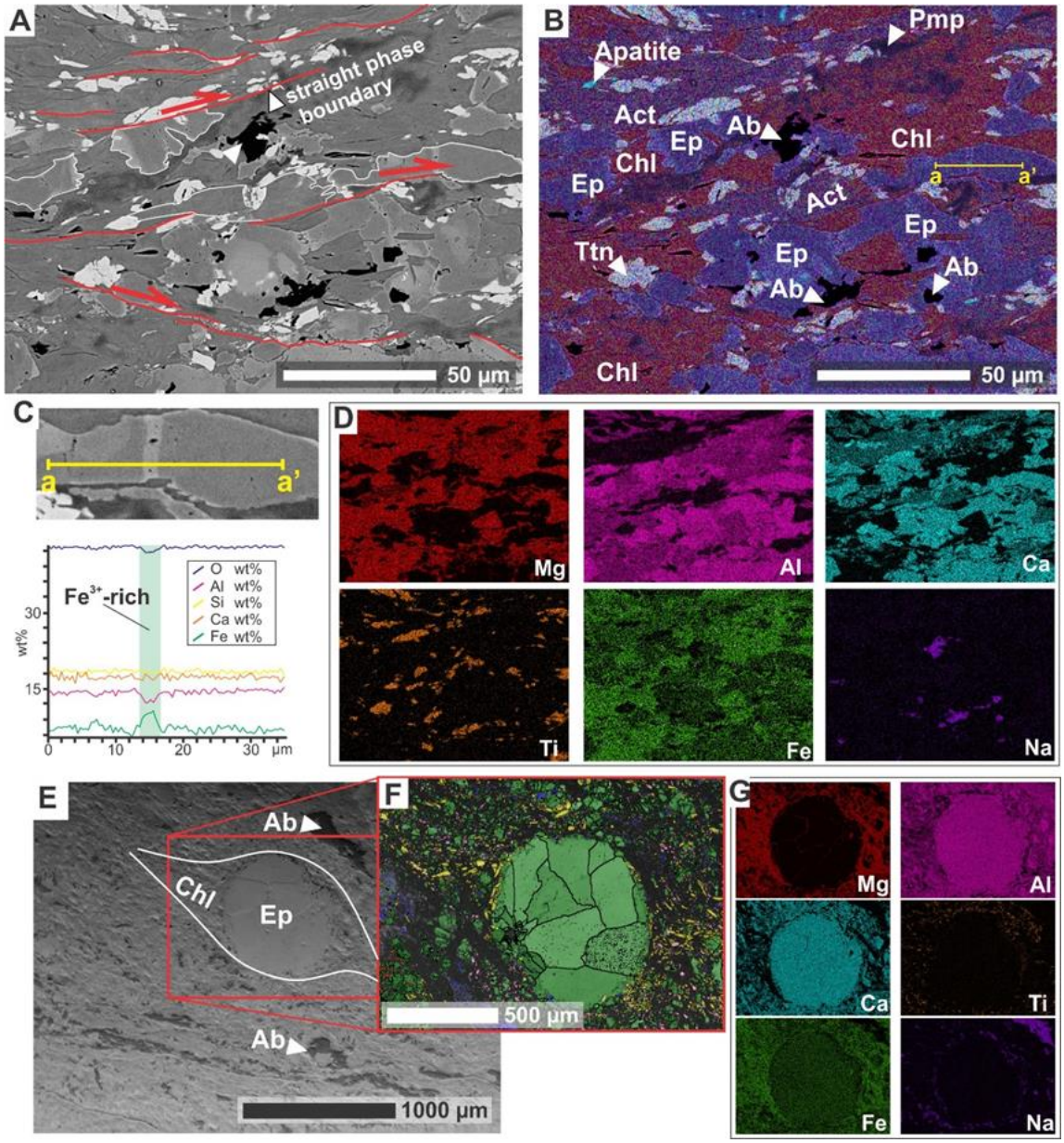

Figure S2.1. Mafic mylonite (PNG15-59A). Parts A, B, and D all depict the same part of this sample. Figures are arranged with the normal slip sense of the Mai'iu fault shown top-to-the-right. A) Backscatter electron (BSE) image of the fine-grained mylonitic matrix. Epidotes are zoned and have Fe-rich rims. B) Layered elemental image (individual element maps in D). Dark red colours highlights chlorite. Albite (dark "inkspots") appears in relation with epidote. C). Elemental-profile through epidote-clast. D) Individual element maps of the area in part (A) and (B). E) BSE image of epidote amygdule in fine-grained mafic matrix (same sample). F) EBSD phase map. Green–epidote; yellow–actinolite; blue–albite; pink–titanite. G) Element maps of the area in part (F). Dark red areas in the magnesium map correspond to chlorite, which we interpret to be neo-formed.

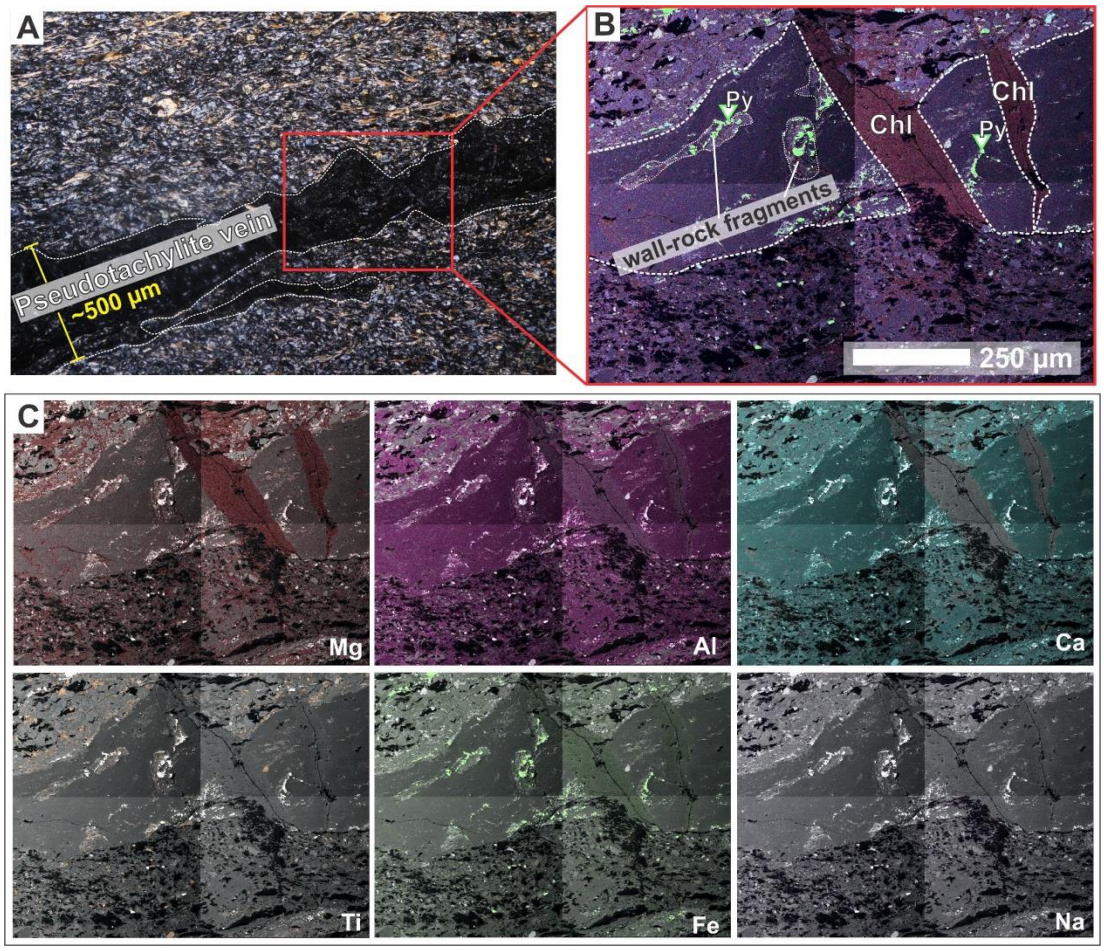

Figure S2.2. Pseudotachylite vein in mylonite sample (PNG16-142C). A) Optical photomicrograph (crossed polarizers). Yellow scale bar in micrometers indicates thickness of pseudotachylite vein. B) Layered elemental image of pseudotachylite vein with abundant pyrite (Py) grains and wall-rock fragments. Dark red areas cross-cutting the pseudotachylite vein indicate chlorite (Chl). C) EDS-based element maps for Mg, Al, Ca, Ti, Fe, and Na. Dark red areas in the magnesium map indicate chlorite.

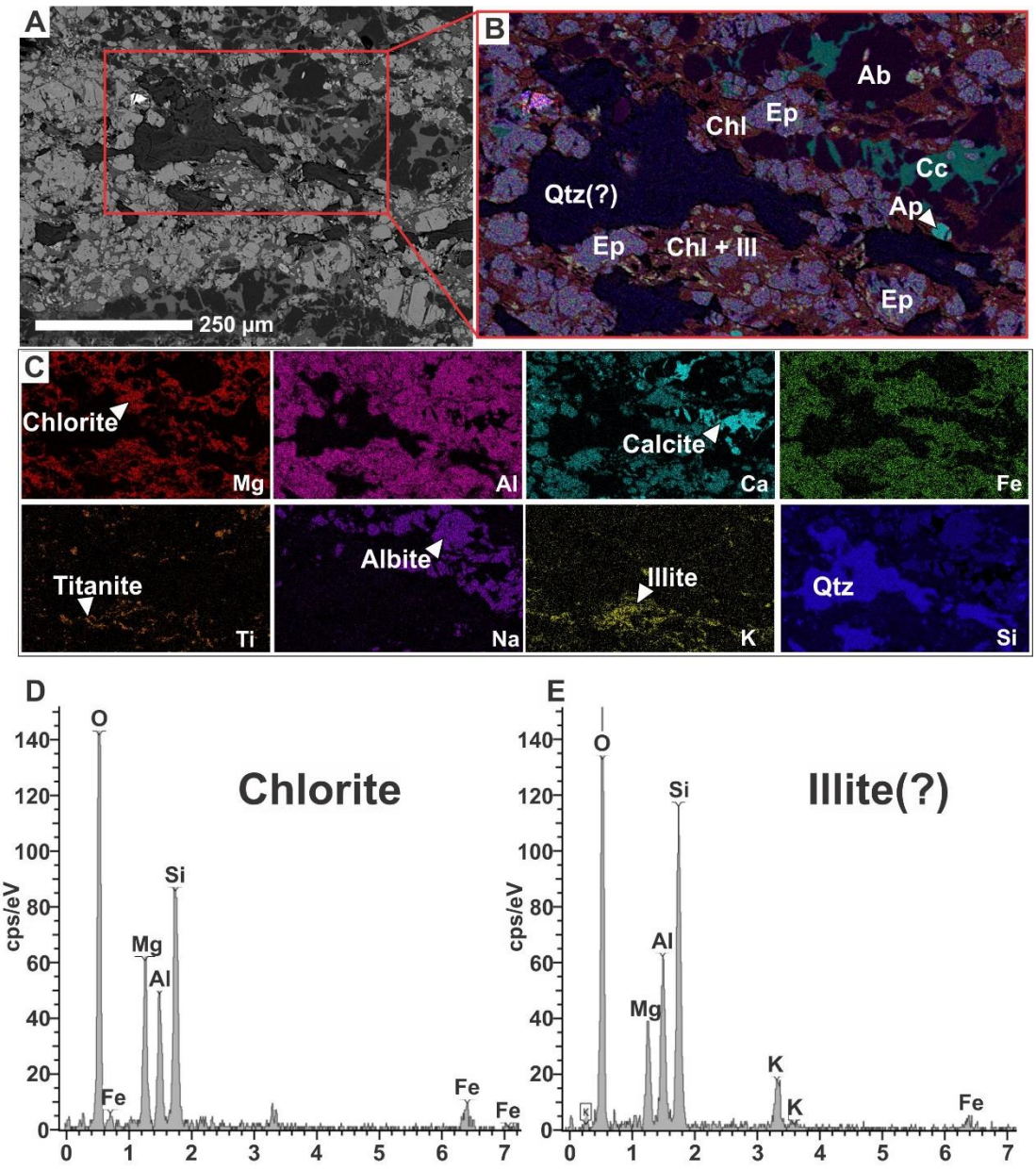

Figure S2.3. Foliated cataclasite (PNG16-17H). Figures are arranged with the normal slip sense of the Mai'iu fault shown top-to-the-right. A) Backscatter electron (BSE) image of dark folia in the cataclasite. B) Layered elemental image based on EDS analysis of the dark folia. Dark, brick red colours indicate chlorite. We infer that chlorite grew and was passively concentrated during a reaction that consumed epidote (purple colour) and actinolite (purple-red colour). C) Elemental maps for Mg, Al, Ca, Fe, Ti, Na, K and Si. D) and E) EDS spectra, respectively, of chlorite and presumably Illite. Note that the presence of 1Md and 2M1 illites in this sample was verified by XRD analyses (see Little et al., 2019).

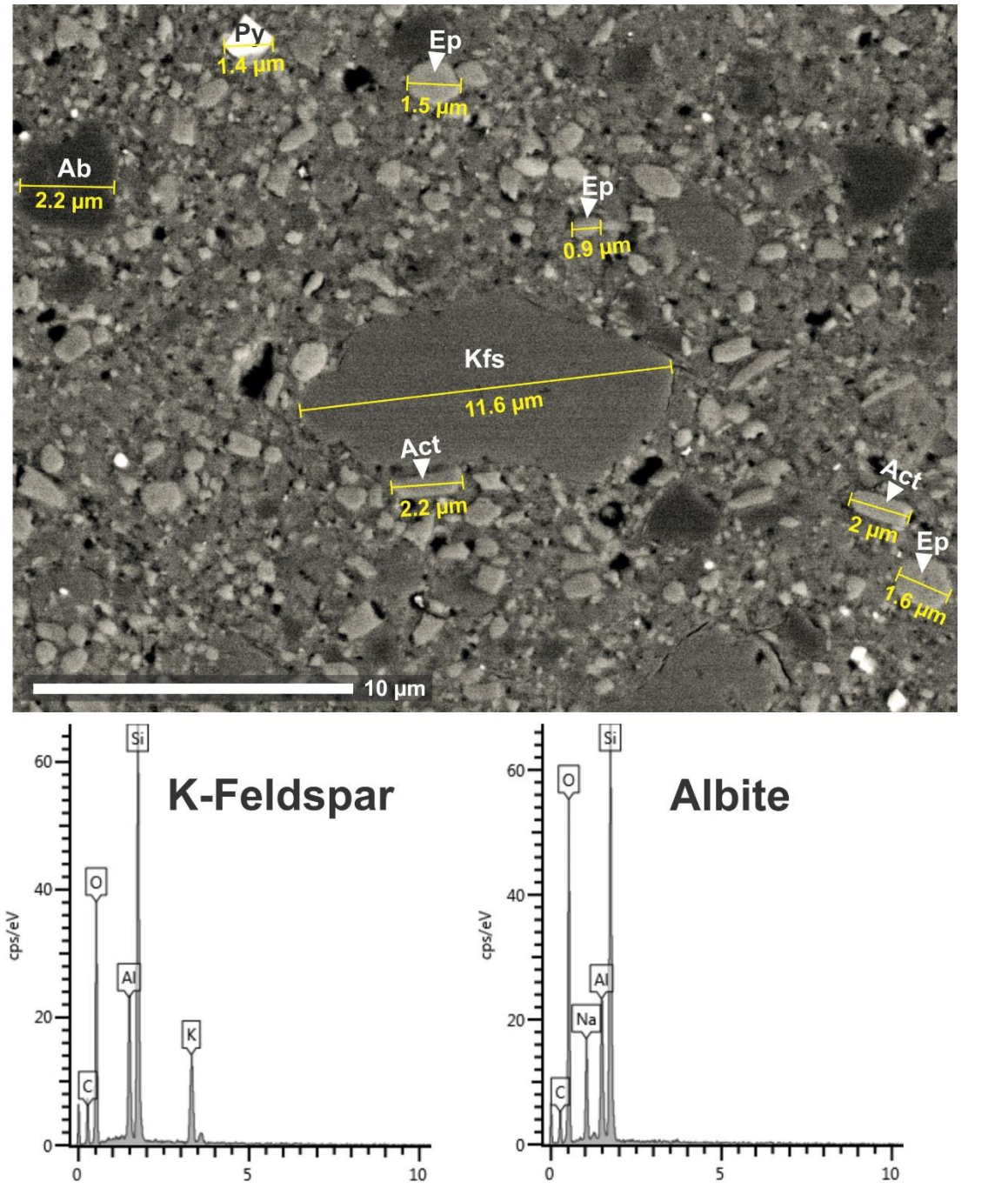

Figure S2.4. Sample PNG15-50DR: Backscatter electron (BSE) image of ultracataclasite and EDS spectra of albite and K-feldspar grains in the matrix. The BSE image includes yellow scale bars in micrometers that indicate the diameters of particular grains, including relict mafic lithic grains and K-feldspar grains.

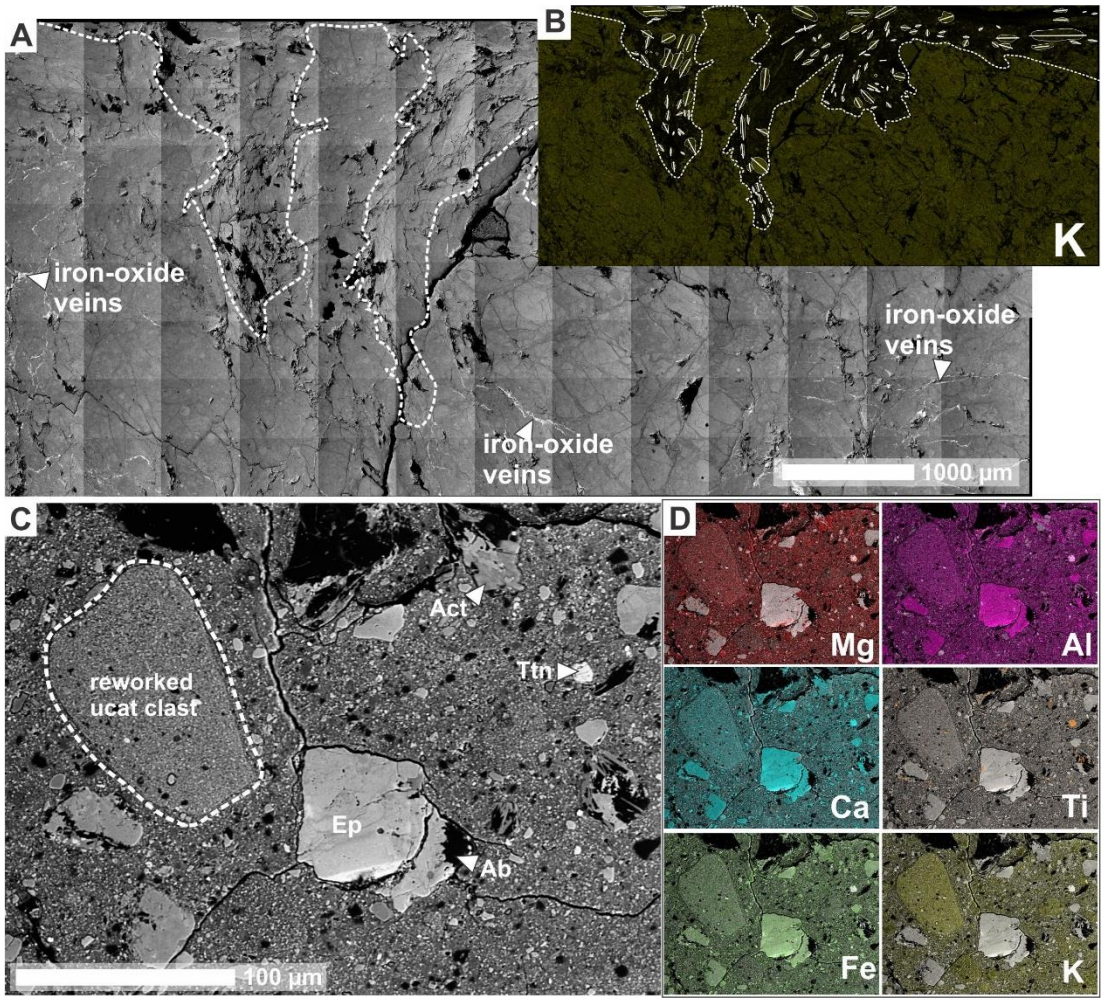

Figure S2.5. Backscatter electron (BSE) images and EDS maps of sample PNG16-142D2 (ultracataclasite). A) BSE image of the whole thin section. On this image, light-colored veins are iron-oxide veins. B) Potassium (K) map of (A) indicates elemental zonation (a K enriched domain—bottom; K depleted domain—top). White glyphs indicate orientation of long-axis of K-rich fragments in the K-depleted domain. C) Back-scatter image of ultracataclasite matrix. Older ultracataclasite-clasts are reworked in the matrix and show an apparent higher concentration of potassium relative to the surrounding matrix. D) Elemental maps for the same area as in C.

Text S3. EBSD Data Processing

Raw EBSD data were processed with the MTEX toolbox for MATLAB (Bachmann et al., 2010) after the approach of Cross (2015). In MTEX, raw EBSD data of indexed pixels are converted to grains based on a Voronoi decomposition method. The script populates the whole map area with grains (defined as areas encompassed by boundaries of >10° misorientation), whereas non-indexed phases are removed in a later step. Identified "grains" smaller than 2 x 2 pixels in size were removed from the acquired EBSD map as they are likely the result of misindexing. A smoothing factor of 2 was applied to the mapped grains. Furthermore, poorly constrained grains were removed based on the fraction of their area covered by raw data (f_i), (Cross, 2015):

$$f_i = \frac{n_i \cdot d_{step}^2}{A_{grain}}, \qquad \text{(Eq. S3.1)}$$

where n_i is the number of indexed pixels in a grain, d_{step} is the step size (width of each pixel), and A_{grain} is the area a grain covers based on the Voronoi decomposition. Because some fault rocks were poorly indexed (especially ultracataclasites, fault gouge, and weathered schists), a critical threshold value for f_i was estimated for every sample based on trade-off curves for the indexed fraction of grains versus the cumulative number of grains. The knee of this curve represents the threshold value between poorly constrained and well constrained grains (Cross, 2015). The grains that fall under the category "poorly constrained grains" were removed from the EBSD map. Step sizes and threshold values for f_i are given for each sample in Table S4.1 to Table S4.4 of S4 ('EBSD-based Fabric Strength and Grain-Size Estimates of Mafic Fault Rocks'). Fabric strength is herein quantified by calculating both the J-index of Bunge (2013) and the M-index of Skemer et al. (2005). The latter parameter measures the difference between the observed distribution of uncorrelated misorientation angles and the distribution of uncorrelated misorientation angles for a random fabric—the stronger the fabric, the greater the M-index ranging from 0 (random fabric) to 1 (single crystal; Skemer et al., 2005; Mainprice et al., 2015). All MTEX scripts for the data processing can be found in the contribution by Mizera (2019).

Text S4. EBSD-based Fabric Strength and Grain-Size Estimates of Mafic Fault Rocks

The following tables and figures summarize the results of the processed EBSD data from the different mafic fault rocks. The results presented in the following tables include mean grain size estimates and fabric strength of actinolite, epidote, albite and titanite in the different fault rock units. The tables are followed by figures of all analysed and processed EBSD maps starting with mafic mylonite samples and continuing with foliated cataclasite, ultracataclasite, gouge and non-mylonitic mafic schist. All crystallographic pole diagrams shown in these figures are Schmidt lower hemisphere equal-area projections.

Actinolite

Sample#	Rock Type	Domain	Tradeoff-Curve	Step Size (μm)	N_O	N_P	N_G	Mean GS	(1σ)	Min	Max	All Grains J (ODF)	All Grains J (MDF)	All Grains S	All Grains M	1 point per Grain J (ODF)	1 point per Grain J (MDF)	1 point per Grain S	1 point per Grain M
15-43	Mylonite	Mafic Matrix	0.4	2.0	80860	57671	523	25.0	±16	4.1	103.8	3.707	1.260	-0.851	0.105	2.762	1.179	-0.700	0.080
16-142C	Mylonite	Montaged Mafic Matrix	0.5	2.0	364636	303953	8140	13.4	±8.6	3.3	117.9	5.317	1.856	-1.097	0.225	4.796	1.708	-0.995	0.204
15-52A	Mylonite	Mafic Matrix	0.3	2.0	44740	29633	433	22.2	±14	5.3	96.9	8.628	2.649	-1.547	0.300	8.013	2.537	-1.498	0.291
16-17E	Mylonite	Mafic Matrix	0.4	1.0	61041	27372	587	9.1	±5	2.3	38.2	1.768	1.058	-0.325	0.041	1.812	1.056	-0.349	0.038
15-73A	Mylonite	Whole Sample	0.5	1.0	275101	163625	2359	10.2	±5.7	2.0	64.5	8.172	2.785	-1.514	0.317	7.838	2.769	-1.508	0.291
15-73A	Mylonite	Actinolite Layer	0.5	1.0	208327	153596	1916	10.7	±6	2.2	64.9	9.217	3.127	-1.649	0.346	8.558	3.092	-1.628	0.316
15-73A	Mylonite	Fine Grained Matrix	0.5	1.0	77930	37409	763	8.7	±4.7	2.0	35.7	6.438	2.132	-1.257	0.261	6.575	2.096	-1.263	0.246
15-59A	Mylonite	Mafic Matrix	0.5	2.0	625853	532722	14657	12.7	±8.7	3.3	162.2	2.479	1.181	-0.515	0.087	2.184	1.122	-0.421	0.072
15-59A	Mylonite	Mafic Matrix	0.4	5.0	34121	19267	1606	23.3	±11	10.0	120.4	3.546	1.430	-0.800	0.149	3.656	1.452	-0.822	0.151
15-59A	Mylonite	Mafic Matrix	0.3	5.0	21434	16443	1335	23.3	±9.6	10.0	97.4	4.320	1.656	-0.984	0.181	4.487	1.687	-1.001	0.185
15-59A	Mylonite	Dark Matrix	0.3	5.0	5681	3585	281	25.0	±9.8	9.2	65.1	3.492	1.335	-0.779	0.139	3.543	1.317	-0.813	0.142
16-125B	Cataclasite	Mafic Matrix	0.3	1.0	25779	17011	262	10.3	±7.4	2.0	70.1	6.814	1.590	-1.050	0.194	4.214	1.280	-0.846	0.144
16-125B	Cataclasite	Mafic Matrix	0.2	0.5	8798	6471	89	7.3	±4.8	1.0	18.4								
16-142E	Cataclasite	Montaged Mafic Matrix	0.5	2.0	239868	189670	5296	12.7	±8.7	3.6	107.8	1.621	1.034	-0.272	0.051	1.523	1.028	-0.233	0.045
16-142E	Ultramylonite	Ultramylonite Layer	0.5	2.0	2900	2227	119	9.1	±4.4	3.3	29.7	2.508	1.021	-0.498	0.022	2.070	1.014	-0.478	0.021
15-50E	Cataclasite	Mafic Matrix	0.3	1.0	15082	9090	149	11.5	±5.8	2.4	37.7	3.551	1.313	-0.783	0.145	3.014	1.157	-0.702	0.093
16-50RD	Cataclasite	Mafic Matrix	0.3	2.0	24298	12356	236	22.1	±11	5.5	61.2	2.152	1.056	-0.410	0.062	2.117	1.043	-0.441	0.051
16-151E	Cataclasite	Dark Matrix	0.4	1.0	71118	54041	1465	7.4	±4.2	1.8	48.5	4.792	1.615	-0.957	0.212	4.653	1.615	-0.935	0.200
16-151E	Cataclasite	Dark Matrix	0.4	2.0	20381	12054	373	13.3	±8.8	4.2	95.7	4.686	1.382	-0.961	0.157	5.017	1.560	-0.988	0.196

Table S4.1 (continued).

											All Grains				1 point per Grain			
Sample#	Rock Type	Domain	Tradeoff-Curve	Step Size (μm)	N_O	N_P	N_G	Mean GS	(1σ)	Min	Max	J (ODF)	J (MDF)	S	M	J (ODF)	J (MDF)	S	M
16-125A	Ultracataclasite	UCAT matrix	0.1	0.5	136359	1715	141	2.3	±0.9	1.3	12.8	1.102	1.000	-0.049	0.003	1.798	1.007	-0.378	0.016
16-142D	Ultracataclasite	UCAT matrix	0.2	0.6	27443	334	27	2.5	±1.1	1.8	10.0	4.019	1.053	-0.738	0.034	14.575	2.477	2.477	0.212
16-142B	Gouge	Matrix	0.3	0.6	28686	8103	250	3.5	±2.5	1.2	22.9	1.256	1.001	-0.098	0.005	1.641	1.013	-0.300	0.018
16-142A	Gouge	Matrix	0.4	0.5	156216	77242	1368	3.8	±2.8	1.0	39.9	1.234	1.001	-0.094	0.006	1.121	1.001	-0.058	0.004
16-126A	Schist/Mylonite?	Mafic Matrix	0.3	0.8	190428	120029	726	12.9	±8.1	1.4	68.6	3.276	1.300	-0.725	0.115	2.747	1.222	-0.625	0.093
16-126B	Schist	Mafic Matrix	0.35	1.5	45274	21704	754	11.3	±5.9	3.2	52.3	2.257	1.127	-0.469	0.071	2.313	1.128	-0.487	0.076
16-169	Schist	Mafic Matrix	0.3	1.5	98667	79461	1918	11.9	±7.9	2.9	80.6	3.305	1.382	-0.771	0.108	3.188	1.358	-0.742	0.114
16-176	Schist	Mafic Matrix	0.3	2.0	40561	12060	288	19.3	±11	4.6	81.5	4.394	1.661	-0.978	0.163	4.849	1.792	-1.116	0.165
16-182	Schist/Mylonite?	Mafic Matrix	0.3	2.0	150845	109770	1042	25.7	±19	3.6	157.5	3.544	1.418	-0.829	0.127	3.939	1.650	-0.923	0.151

Table S4.1. EBSD-derived grain-size statistics and fabric strengths (J-index, S-index and M-index) for actinolite. N_O—number of orientations; N_P—number of pixels; N_G—number of grains; Mean GS—mean grain size; 1σ—standard deviation; Min, Max—minimum and maximum measured grain sizes, respectively.

Epidote

Sample#	Rock Type	Domain	Tradeoff-Curve	Step Size (µm)	N_O	N_P	N_G	Mean GS	(1σ)	Min	Max	All Grains J (ODF)	All Grains J (MDF)	All Grains S	All Grains M	1 point per Grain J (ODF)	1 point per Grain J (MDF)	1 point per Grain S	1 point per Grain M
15-43	Mylonite	Mafic Matrix Montaged	0.4	2.0	36874	15459	320	19.0	±8.8	3.7	48.5	1.388	1.009	-0.171	0.030	1.555	1.009	-0.247	0.032
16-142C	Mylonite	Mafic Matrix	0.5	2.0	400404	380064	2770	22.8	±18	3.6	135.8	2.376	1.183	-0.546	0.136	2.062	1.126	-0.424	0.118
15-52A	Mylonite	Mafic Matrix	0.3	2.0	52085	30822	549	23.2	±10	4.1	61.7	2.157	1.122	-0.447	0.114	2.301	1.167	-0.520	0.136
16-17E	Mylonite	Mafic Matrix	0.4	1.0	667540	512312	5383	12.0	±7.1	1.7	87.5	1.093	1.000	-0.045	0.007	1.079	1.000	-0.040	0.007
15-73A	Mylonite	Whole Sample	0.5	1.0	102747	60270	327	13.8	±9.4	2.2	77.1	2.193	1.025	-0.376	0.048	1.586	1.016	-0.284	0.041
15-73A	Mylonite	Actinolite Layer	0.5	1.0	24870	18773	66	15.1	±11	2.8	78.4	6.067	1.143	-0.950	0.071	2.702	1.036	-0.696	0.049
15-73A	Mylonite	Fine Grained Matrix	0.5	1.0	80935	47727	305	13.4	±7.9	2.2	74.7	2.437	1.032	-0.395	0.052	1.581	1.015	-0.286	0.040
15-59A	Mylonite	Mafic Matrix	0.5	2.0	623947	598470	4035	21.8	±20	3.3	223.8	1.204	1.001	-0.091	0.008	1.057	1.000	-0.029	0.004
15-59A	Mylonite	Mafic Matrix	0.4	5.0	50459	38023	1472	31.2	±19	10.4	170.6	1.283	1.004	-0.128	0.019	1.202	1.004	-0.096	0.020
15-59A	Mylonite	Mafic Matrix	0.3	5.0	18985	17722	682	30.1	±17	11.3	172.7	1.655	1.004	-0.249	0.014	1.295	1.004	-0.140	0.021
15-59A	Mylonite	Mafic Matrix	0.3	5.0	24119	20831	776	33.2	±18	12.2	170.8	1.660	1.016	-0.276	0.036	1.429	1.014	-0.192	0.038
16-142E	Cataclasite	Mafic Matrix Montaged	0.5	2.0	190620	153614	3254	14.8	±9.6	3.6	115.1	1.160	1.001	-0.075	0.010	1.109	1.001	-0.053	0.008
15-50E	Cataclasite	Mafic Matrix	0.3	1.0	32839	29326	134	18.7	±10	3.7	60.4	2.589	1.019	-0.569	0.031	1.925	1.013	-0.422	0.039
16-50RD	Cataclasite	Mafic Matrix	0.3	2.0	29596	19683	277	26.2	±11	5.8	63.9	1.324	1.001	-0.148	0.007	1.399	1.002	-0.188	0.013
16-151E	Cataclasite	Dark Matrix	0.4	2.0	65694	35518	821	17.1	±9	4.5	76.4	1.197	1.001	-0.094	0.009	1.229	1.002	-0.110	0.012

Table S4.2 (continued)

Sample#	Rock Type	Domain	Tradeoff-Curve	Step Size (μm)	N_O	N_P	N_G	Mean GS	(1σ)	Min	Max	All Grains J (ODF)	All Grains J (MDF)	All Grains S	All Grains M	1 point per Grain J (ODF)	1 point per Grain J (MDF)	1 point per Grain S	1 point per Grain M
16-125A	Ultracataclasite	UCAT Matrix	0.1	0.5	100167	237	37	1.6	±0.5	1.0	3.0	1.415	1.007	-0.168	0.021	6.282	1.159	-1.279	0.056
16-142D	Ultracataclasite	UCAT Matrix	0.2	0.6	24865	4116	164	3.0	±2.1	1.2	14.0	1.260	1.002	-0.116	0.005	1.503	1.002	-0.242	0.006
16-142B	Gouge	Matrix	0.3	0.6	30410	12664	244	3.7	±3	1.1	18.7	1.441	1.002	-0.169	0.006	1.586	1.004	-0.264	0.013
16-142A	Gouge	Matrix	0.4	0.5	221658	151589	2351	3.9	±3.1	0.7	56.6	1.275	1.001	-0.099	0.003	1.201	1.001	-0.096	0.006
16-126B	Schist	Mafic Matrix	0.4	1.5	213165	189910	1116	20.3	±14	2.7	148.7	3.953	1.065	-0.499	0.066	1.478	1.008	-0.176	0.029
16-182	Schist/Mylonite?	Mafic Matrix	0.3	2.0	164960	121725	1188	27.1	±16	3.9	180.0	1.372	1.006	-0.165	0.024	1.319	1.008	-0.149	0.029
15-72A	Schist	Mafic Matrix	0.5	2.0	119483	109578	1733	16.2	±12	3.7	109.8	1.832	1.045	-0.340	0.067	1.721	1.052	-0.305	0.068

Table S4.2. EBSD-based grain-size statistics and fabric strengths (J-index, S-index and M-index) for epidote. N_O—number of orientations; N_P—number of pixels; N_G—number of grains; Mean GS—mean grain size; 1σ—standard deviation; Min, Max—minimum and maximum measured grain sizes, respectively.

Albite

Sample#	Rock Type	Domain	Tradeoff-Curve	Step Size (μm)	N_O	N_P	N_G	Mean GS	(1σ)	Min	Max	All Grains J (ODF)	All Grains J (MDF)	All Grains S	All Grains M	1 point per Grain J (ODF)	1 point per Grain J (MDF)	1 point per Grain S	1 point per Grain M
15-43	Schist	Mafic Matrix	0.4	2.0	170016	120357	2415	16.7	±11.0	3.6	99.8	1.814	1.023	-0.323	0.031	1.745	1.017	-0.309	0.027
16-142C	Mylonite	Montaged Mafic Matrix	0.5	2.0	108869	87195	2368	13.0	±8.6	3.3	66.6	1.443	1.008	-0.206	0.017	1.340	1.004	-0.171	0.013
15-52A	Mylonite	Mafic Matrix	0.3	2.0	22353	16053	227	21.7	±14.0	3.6	83.8	3.138	1.040	-0.675	0.036	2.520	1.029	-0.622	0.030
16-17E	Mylonite	Matrix	0.4	1.0	454765	222597	5336	8.5	±4.6	1.8	61.5	1.418	1.013	-0.219	0.022	1.539	1.022	-0.277	0.028
15-59A	Mylonite	Mafic Matrix	0.5	2.0	5753	4914	118	12.5	±9.3	3.6	56.8	21.897	3.987	-2.102	0.326	13.885	2.237	-1.812	0.211
15-59A	Mylonite	Mafic Matrix	0.4	5.0	8296	5187	256	28.5	±19.0	9.7	99.9	2.470	1.015	-0.515	0.019	2.178	1.017	-0.517	0.025
15-59A	Mylonite	Mafic Matrix	0.3	5.0	4670	3956	190	25.9	±14.0	11.2	85.4	4.961	1.081	-0.909	0.035	2.721	1.026	-0.667	0.027
16-125B	Cataclasite/Ultramylonite	Mafic Matrix	0.3	1.0	50774	38749	732	8.7	±6.5	1.8	46.7	1.984	1.009	-0.369	0.019	1.712	1.007	-0.319	0.017
16-125B	Cataclasite/Ultramylonite	Mafic Matrix	0.2	0.5	272017	213089	1770	6.8	±6.9	0.8	55.8	1.781	1.007	-0.300	0.017	1.656	1.006	-0.273	0.013
16-142E	Cataclasite	Montaged Mafic Matrix	0.5	2.0	238202	172818	3692	14.4	±11.0	3.3	106.1	1.491	1.011	-0.226	0.023	1.370	1.007	-0.191	0.018
16-142E	Ultramylonite	Ultramylonite Layer	0.5	2.0	1967	1241	84	9.9	±3.9	4.4	22.4	3.115	1.030	-0.722	0.027	3.651	1.042	-0.954	0.026
15-50E	Cataclasite	Mafic Matrix	0.3	1.0	69721	58896	360	13.1	±12.0	1.8	67.7	3.599	1.069	-0.764	0.041	2.520	1.023	-0.562	0.028
16-50RD	Cataclasite	Mafic Matrix	0.3	2.0	22338	15439	295	18.9	±13.0	3.6	65.5	2.594	1.028	-0.539	0.031	3.198	1.029	-0.653	0.024
16-151E	Cataclasite	Dark Matrix	0.4	1.0	268945	232190	2483	10.4	±7.8	1.8	56.9	1.429	1.005	-0.204	0.015	1.318	1.003	-0.164	0.011
16-151E	Cataclasite	Dark Matrix	0.4	2.0	89562	63191	1428	16.6	±9.4	3.3	74.9	1.550	1.009	-0.255	0.022	1.453	1.008	-0.230	0.020
16-125A	Ultracataclasite	UCAT Matrix	0.3	0.5	6412	3044	163	2.5	±1.5	1.0	10.3	2.114	1.008	-0.340	0.014	2.846	1.023	-0.711	0.028

Table S4.3 (continued)

Sample#	Rock Type	Domain	Tradeoff-Curve	Step Size (μm)	N_O	N_P	N_G	Mean GS	(1σ)	Min	Max	All Grains J (ODF)	All Grains J (MDF)	All Grains S	All Grains M	1 point per Grain J (ODF)	1 point per Grain J (MDF)	1 point per Grain S	1 point per Grain M
16-142D	Ultracataclasite	UCAT Matrix	0.2	0.6	2497	944	114	2.1	±0.8	1.1	5.6	1.929	1.007	-0.324	0.012	3.608	1.046	-0.886	0.026
16-142B	Gouge	Matrix	0.3	0.6	17292	13270	508	2.9	±2.4	1.1	16.8	3.595	1.040	-0.682	0.024	2.416	1.011	-0.493	0.012
16-142A	Gouge	Matrix	0.4	0.5	47391	35808	1081	2.8	±2.3	0.9	20.0	2.412	1.021	-0.464	0.025	2.065	1.007	-0.385	0.009
16-126A	Schist/Mylonite?	Mafic Matrix	0.3	0.8	166814	114747	1312	8.7	±6.6	1.3	68.6	1.736	1.012	-0.284	0.021	1.633	1.011	-0.284	0.019
16-126B	Schist	Mafic Matrix	0.4	1.5	39122	22449	623	11.5	±7.2	2.5	41.4	1.645	1.008	-0.285	0.016	1.728	1.011	-0.334	0.019
16-169	Schist	Mafic Matrix	0.3	1.5	110051	78042	2168	12.2	±7.0	2.7	65.6	1.510	1.004	-0.226	0.012	1.408	1.004	-0.200	0.014
16-176	Schist	Mafic Matrix	0.3	2.0	11691	4851	130	17.8	±9.0	4.8	49.4	2.197	1.013	-0.441	0.017	3.107	1.033	-0.801	0.024
16-182	Schist/Mylonite?	Mafic Matrix	0.3	2.0	50956	25171	367	24.5	±14.0	4.0	94.2	2.229	1.061	-0.515	0.050	2.673	1.105	-0.691	0.065
15-72A	Schist	Mafic Matrix	0.5	2.0	96519	75656	2593	12.3	±7.0	3.3	57.9	1.503	1.010	-0.230	0.021	1.413	1.007	-0.203	0.019

Table S4.3. EBSD-based grain-size statistics and fabric strengths (J-index, S-index and M-index) for albite. N_O—number of orientations; N_P—number of pixels; N_G—number of grains; Mean GS—mean grain size; 1σ—standard deviation; Min, Max—minimum and maximum measured grain sizes, respectively.

Titanite

Sample#	Rock Type	Domain	Tradeoff-Curve	Step Size (μm)	N_O	N_P	N_G	Mean GS	(1σ)	Min	Max	All Grains J (ODF)	All Grains J (MDF)	All Grains S	All Grains M	1 point per Grain J (ODF)	1 point per Grain J (MDF)	1 point per Grain S	1 point per Grain M
16-142C	Mylonite	Montaged Mafic Matrix	0.5	2.0	43512	35236	1211	12.2	7.0	3.3	56.9	2.318	1.171	-0.507	0.096	2.044	1.133	-0.429	0.085
15-52A	Mylonite	Mafic Matrix	0.3	2.0	4023	1233	73	13.1	5.1	4.7	30.9	2.357	1.129	-0.591	0.087	3.366	1.179	-0.914	0.114
15-73A	Mylonite	Mafic Matrix	0.5	1.0	182312	73344	2114	7.8	3.4	2.0	30.2	2.023	1.144	-0.412	0.080	2.141	1.165	-0.453	0.085
15-73A	Mylonite	Mafic Matrix	0.5	1.0	36330	18659	447	8.3	3.4	2.4	22.7	2.787	1.340	-0.658	0.118	3.576	1.570	-0.873	0.151
15-73A	Mylonite	Fine Grained Matrix	0.5	1.0	148002	60466	1791	7.6	3.3	2.0	30.4	1.892	1.112	-0.371	0.071	1.959	1.123	-0.399	0.074
16-17E	Mylonite	Mafic Matrix	0.4	1.0	24395	5565	336	5.8	2.5	1.9	15.0	1.157	1.002	-0.075	0.010	1.373	1.002	-0.179	0.011
15-59A	Mylonite	Mafic Matrix	0.5	2.0	85909	62208	3350	10.5	4.8	3.3	43.5	1.473	1.033	-0.209	0.038	1.404	1.024	-0.181	0.032
15-59A	Mylonite	Mafic Matrix	0.4	5.0	2488	177	34	16.4	2.8	12.0	23.8	1.380	1.013	-0.179	0.025	4.372	1.200	-1.149	0.091
15-59A	Mylonite	Mafic Matrix	0.3	5.0	723	96	19	17.0	3.3	12.0	25.5	1.723	1.031	-0.338	0.043	5.582	1.282	-1.366	0.109
15-59A	Ultramylonite?	Mafic Matrix	0.3	5.0	1028	81	16	18.8	3.7	13.7	25.6	1.485	1.009	-0.219	0.021	7.436	1.620	-1.645	0.194
16-142E	Cataclasite	Montaged Mafic Matrix	0.5	2.0	17517	9227	642	9.1	4.3	3.3	44.4	1.279	1.004	-0.123	0.010	1.314	1.006	-0.158	0.011
16-142E	Ultramylonite	Ultramylonite Layer	0.5	2.0	460	230	22	8.0	3.2	4.5	15.6	3.301	1.053	-0.756	0.035	5.334	1.171	-1.299	0.057
15-50E	Cataclasite	Mafic Matrix	0.3	1.0	1961	1051	30	9.2	4.5	2.4	18.4	3.194	1.056	-0.672	0.041	3.557	1.034	-0.922	0.021
16-50RD	Cataclasite	Mafic Matrix	0.3	2.0	3161	781	39	13.8	6.4	5.6	34.0	1.594	1.003	-0.263	0.009	3.415	1.060	-0.935	0.060
16-151E	Cataclasite	Mafic Matrix	0.4	1.0	6824	3288	169	5.9	2.5	1.9	16.2	1.746	1.027	-0.310	0.037	1.832	1.028	-0.377	0.037
16-151E	Cataclasite	Mafic Matrix	0.4	2.0	1776	356	36	9.2	3.2	4.8	17.8	1.887	1.024	-0.351	0.038	3.747	1.076	-0.991	0.045

Table S4.4 (continued)

											All Grains				1 point per Grain			
Sample#	**Rock Type**	**Domain**	**Tradeoff-Curve**	**Step Size (μm)**	**N_O**	**N_P**	**N_G**	**Mean GS**	**(1σ)**	**Min**	**Max**	**J (ODF)**	**J (MDF)**	**S**	**M**	**J (ODF)**	**J (MDF)**	**S**	**M**
16-125A	Ultracataclasite	UCAT Matrix	0.3	0.5	57747	463	49	2.1	0.6	1.1	3.5	1.191	1.002	-0.089	0.006	2.649	1.022	-0.698	0.022
16-142D	Ultracataclasite	UCAT Matrix	0.2	0.6	12604	932	109	2.2	0.8	1.2	4.9	1.199	1.002	-0.091	0.009	1.809	1.005	-0.383	0.016
16-142B	Gouge	Matrix	0.3	0.6	10744	1889	118	2.7	1.4	1.2	8.3	1.215	1.002	-0.099	0.008	1.796	1.007	-0.364	0.016
16-142A	Gouge	Matrix	0.4	0.5	59202	26103	1266	2.6	1.5	0.9	16.6	1.140	1.000	-0.064	0.005	1.095	1.000	-0.047	0.002
16-126A	Schist/Mylonite?	Mafic Matrix	0.3	0.8	40846	12956	321	7.6	3.7	1.8	25.5	1.309	1.009	-0.145	0.021	1.455	1.011	-0.219	0.027
16-126B	Schist	Mafic Matrix	0.4	1.5	20265	6685	389	9.3	4.2	3.2	31.9	1.445	1.022	-0.201	0.039	1.538	1.019	-0.256	0.036
PNG16-169	Schist	Mafic Matrix	0.3	1.5	4948	1236	114	7.5	2.8	3.5	14.6	1.249	1.001	-0.116	0.007	1.890	1.014	-0.420	0.030
16-182	Schist/Mylonite?	Mafic Matrix	0.3	2.0	10012	2115	118	13.5	5.5	5.0	32.7	1.475	1.016	-0.227	0.029	2.148	1.022	-0.493	0.032
15-72A	Schist	Mafic Matrix	0.5	2.0	5904	1401	168	7.1	3.3	3.7	37.8	1.427	1.011	-0.186	0.029	1.838	1.024	-0.385	0.045

Table S4.4. EBSD-based grain-size statistics and fabric strengths (J-index, S-index and M-index) for titanite. N_O—number of orientations; N_P—number of pixels; N_G—number of grains; Mean GS—mean grain size; 1σ—standard deviation; Min, Max—minimum and maximum measured grain sizes, respectively.

Mafic Mylonites:

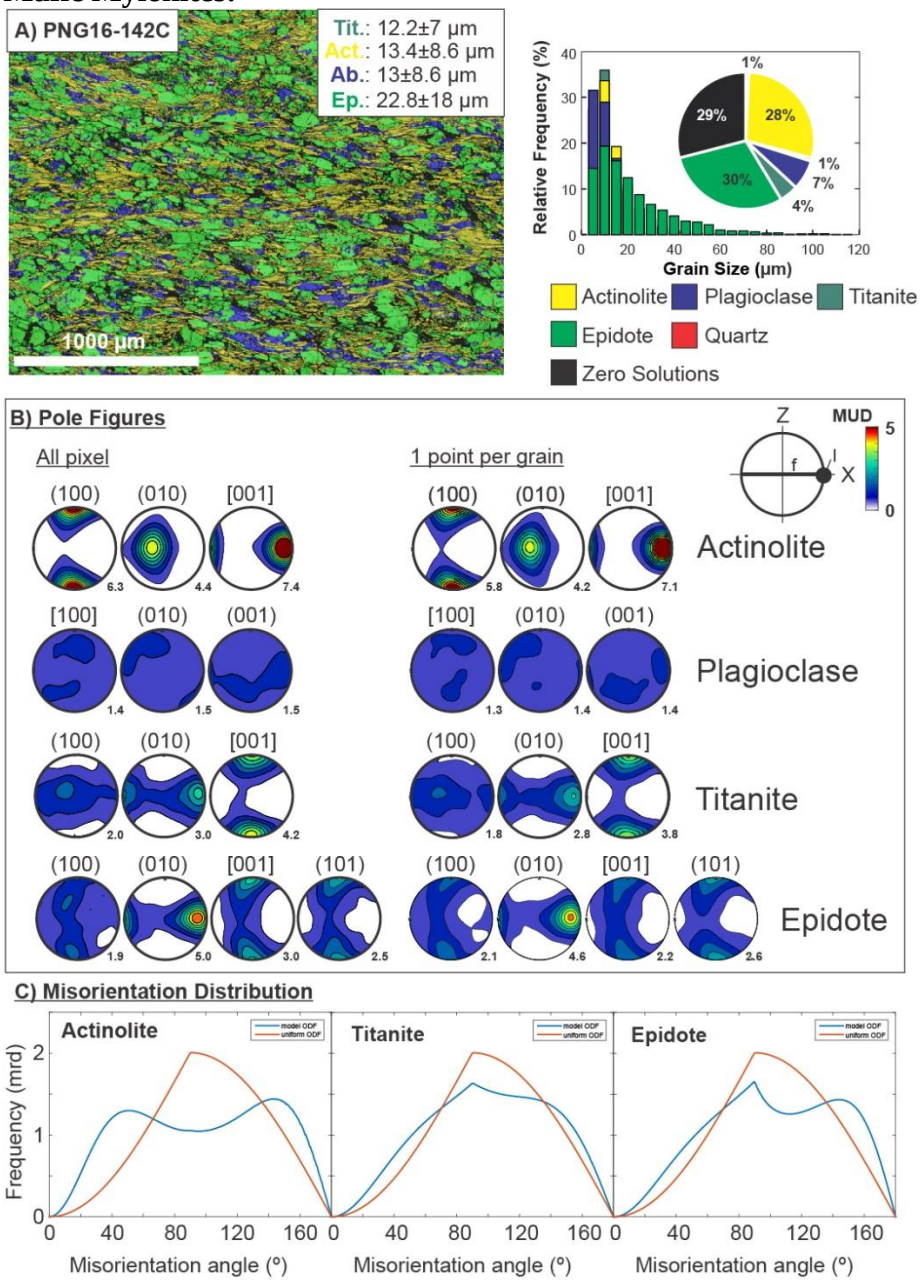

Figure S4.1. EBSD data for mylonite sample PNG16-142C (exhumed beneath active Mai'iu fault). A) EBSD-based phase map (2 µm step size) of the mylonite sample and average grain sizes of titanite, actinolite, epidote and albite (left-hand site); grain-size histogram (relative frequency[%] vs. grain size [µm]) and phase fraction (%; pie diagram) of selected minerals (right-hand side). B) Contoured pole figures of selected crystallographic axes and poles; left—based on all pixels; right—based on one point per grain. MUD—Multiples of uniform distribution; l—lineation; f—foliation. C) Misorientation distribution plot (misorientation angle versus frequency [mrd=multiples of random density]) of selected minerals for uncorrelated grains (blue curves), and a theoretical random distribution (red curves). ODF—Orientation density functions.

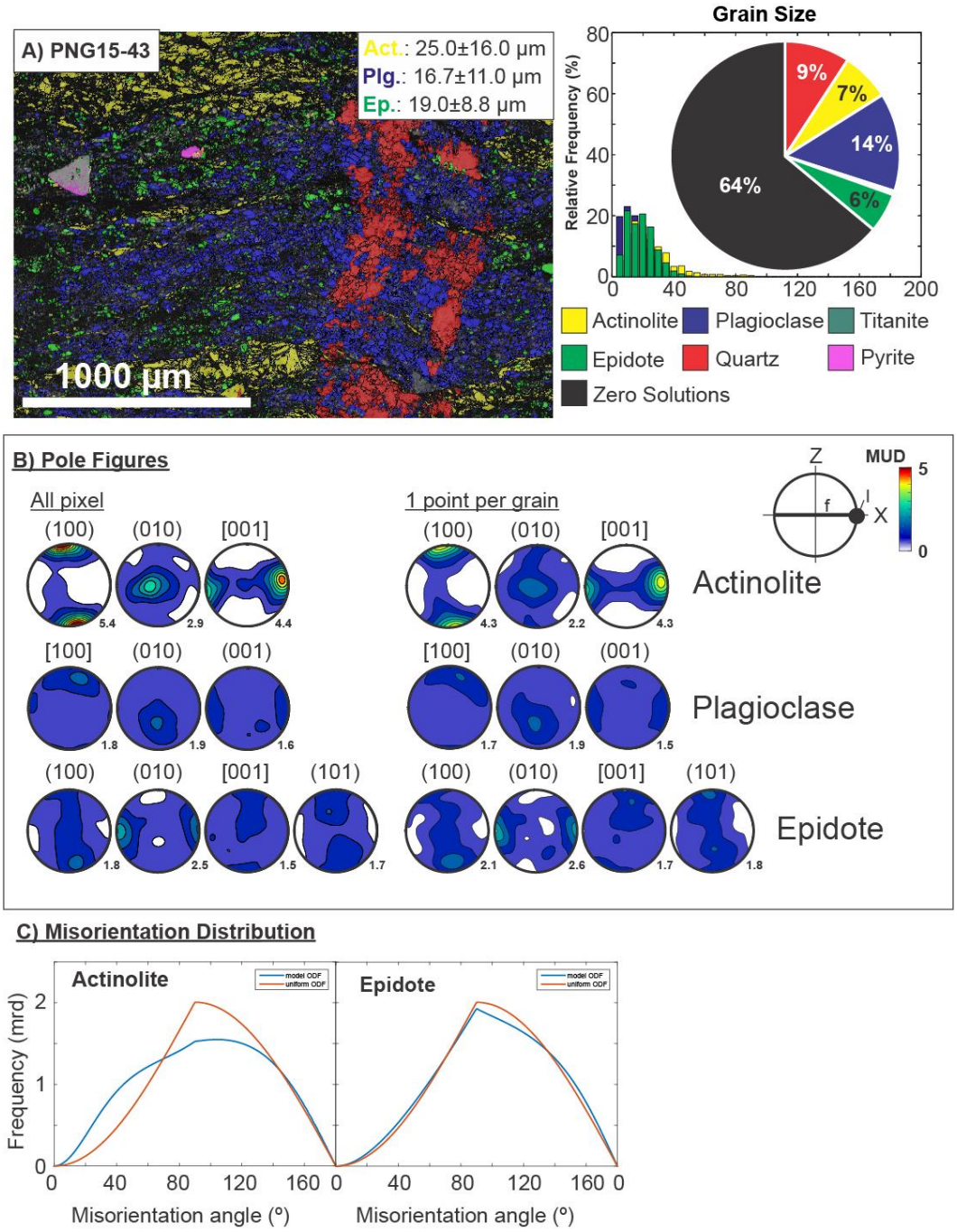

Figure S4.2. EBSD data for mylonite sample PNG15-43 (~700 m south of the active Mai'iu fault trace). A) EBSD-based phase map (2 µm step size) and average grain sizes of actinolite, epidote and albite (left-hand site); grain-size histogram (relative frequency[%] vs. grain size [µm]) and phase fraction (%; pie diagram) of selected minerals (right-hand side). B) Contoured pole figures of selected crystallographic axes and poles; left—based on all pixels; right—based on one point per grain. MUD—Multiples of uniform distribution; l—lineation; f—foliation. C) Misorientation distribution plot (misorientation angle versus frequency [mrd=multiples of random density]) of selected minerals for uncorrelated grains (blue curves), and a theoretical random distribution (red curves). ODF—Orientation density functions.

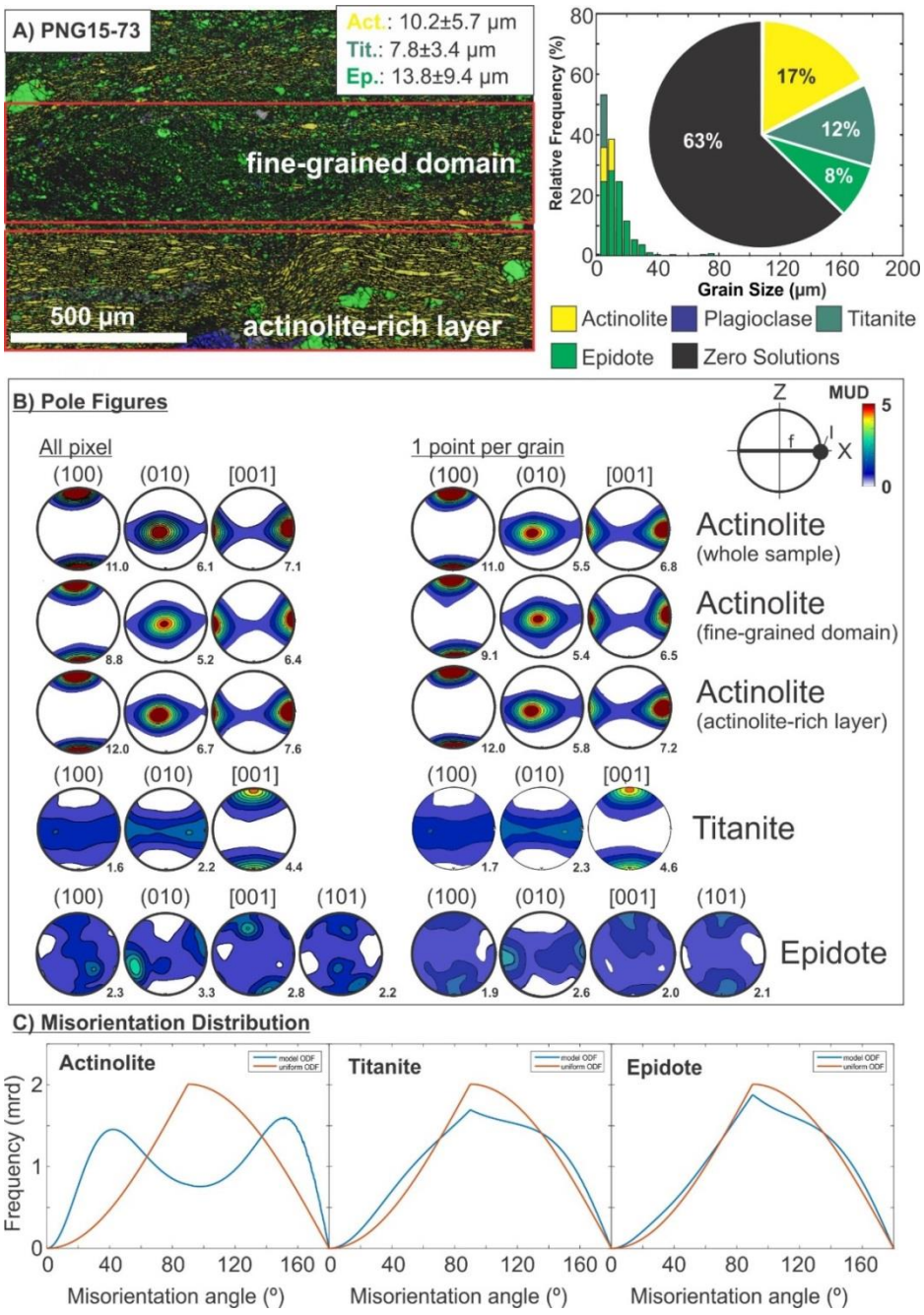

Figure S4.3. EBSD data for mylonite sample PNG15-73 (~10 m south of the active Mai'iu fault trace). A) EBSD-based phase map (1 µm step size) and average grain sizes of titanite, actinolite and epidote based on the whole map (left-hand site); grain-size histogram (relative frequency[%] vs. grain size [µm]) and phase fraction (%; pie diagram) of selected minerals based on the whole map (right-hand side). B) Contoured pole figures of selected crystallographic axes and poles; left—based on all pixels; right—based on one point per grain. MUD—Multiples of uniform distribution; l—lineation; f—foliation. C) Misorientation distribution plot (misorientation angle versus frequency [mrd=multiples of random density]) of selected minerals based on the whole map for uncorrelated grains (blue curves), and a theoretical random distribution (red curves). ODF—Orientation density functions.

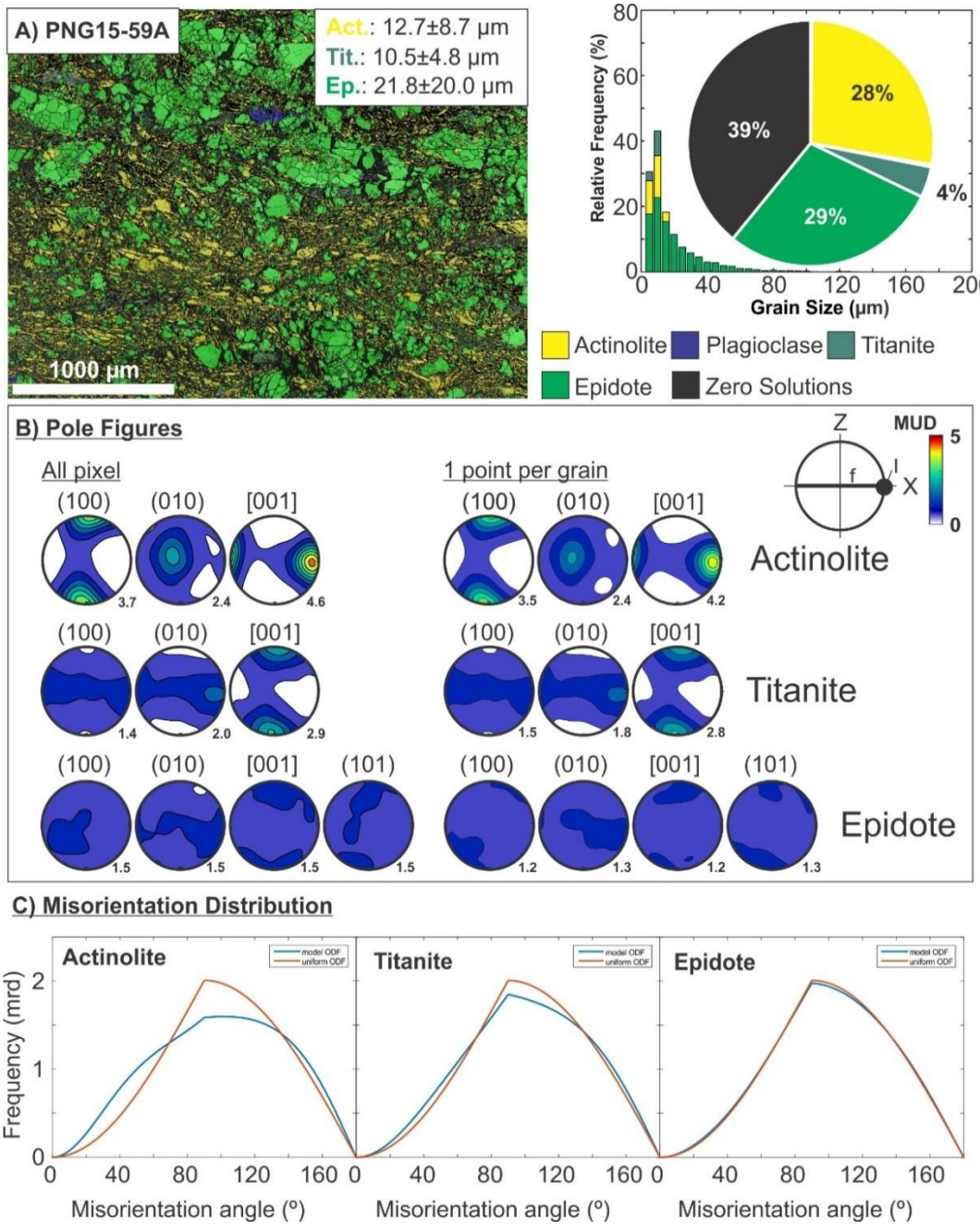

Figure S4.4. EBSD data for an epidote-rich domain of mylonite sample PNG15-59A (~50 m south of the active Mai'iu fault trace). A) EBSD-based phase map (2 µm step size) and average grain sizes of titanite, actinolite and epidote (left-hand site); grain-size histogram (relative frequency[%] vs. grain size [µm]) and phase fraction (%; pie diagram) of selected minerals (right-hand side). B) Contoured pole figures of selected crystallographic axes and poles; left—based on all pixels; right—based on one point per grain. MUD—Multiples of uniform distribution; l—lineation; f—foliation. C) Misorientation distribution plot (misorientation angle versus frequency [mrd=multiples of random density]) of selected minerals for uncorrelated grains (blue curves), and a theoretical random distribution (red curves). ODF—Orientation density functions.

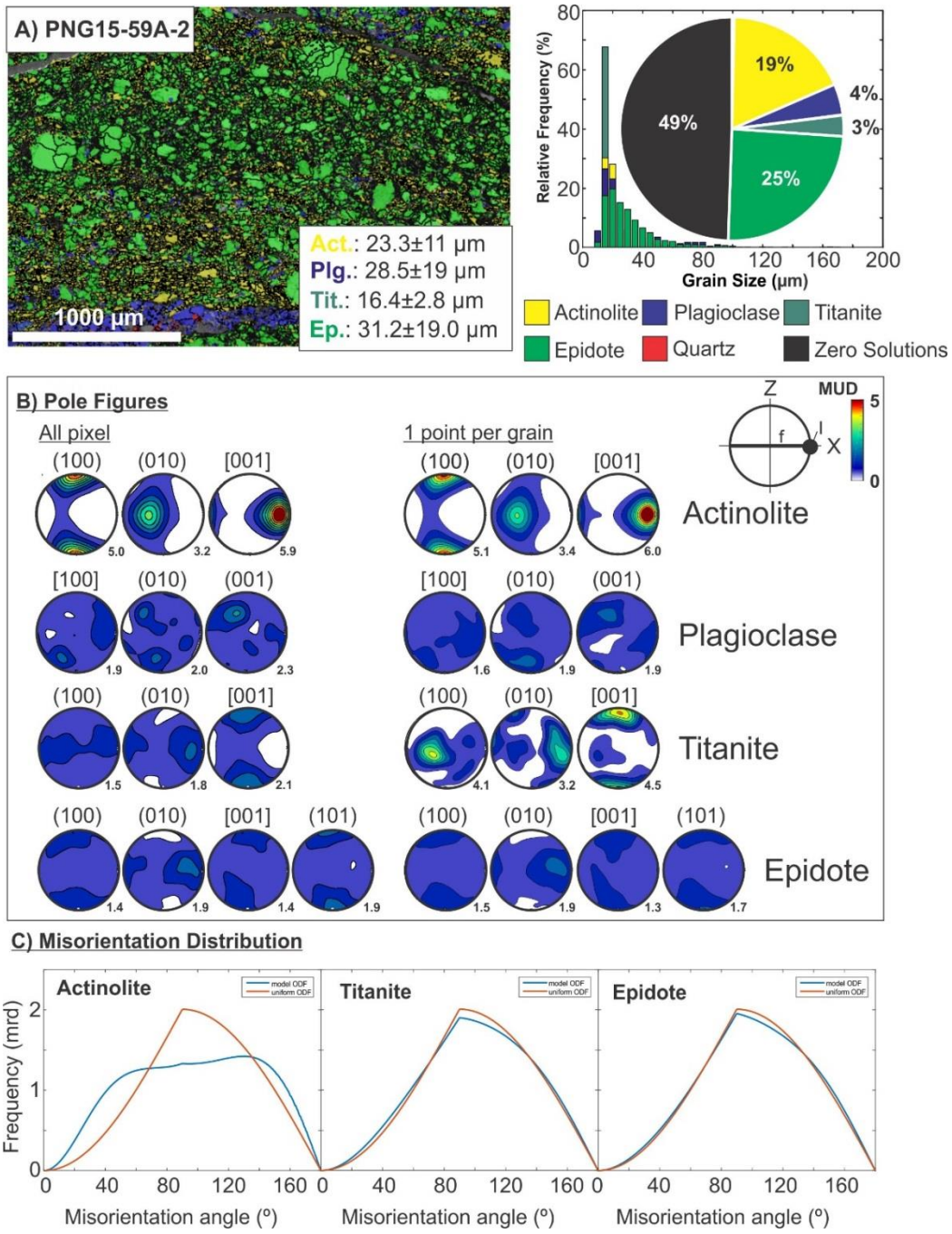

Figure S4.5. EBSD data for mylonite sample PNG15-59A-2 (~50 m south of the active Mai'iu fault trace). A) EBSD-based phase map (5 µm step size) and average grain sizes of titanite, actinolite, epidote and albite (left-hand site); grain-size histogram (relative frequency[%] vs. grain size [µm]) and phase fraction (%; pie diagram) of selected minerals (right-hand side). B) Contoured pole figures of selected crystallographic axes and poles; left—based on all pixels; right—based on one point per grain. MUD—Multiples of uniform distribution; l—lineation; f—foliation. C) Misorientation distribution plot (misorientation angle versus frequency [mrd=multiples of random density]) of selected minerals for uncorrelated grains (blue curves), and a theoretical random distribution (red curves). ODF—Orientation density functions.

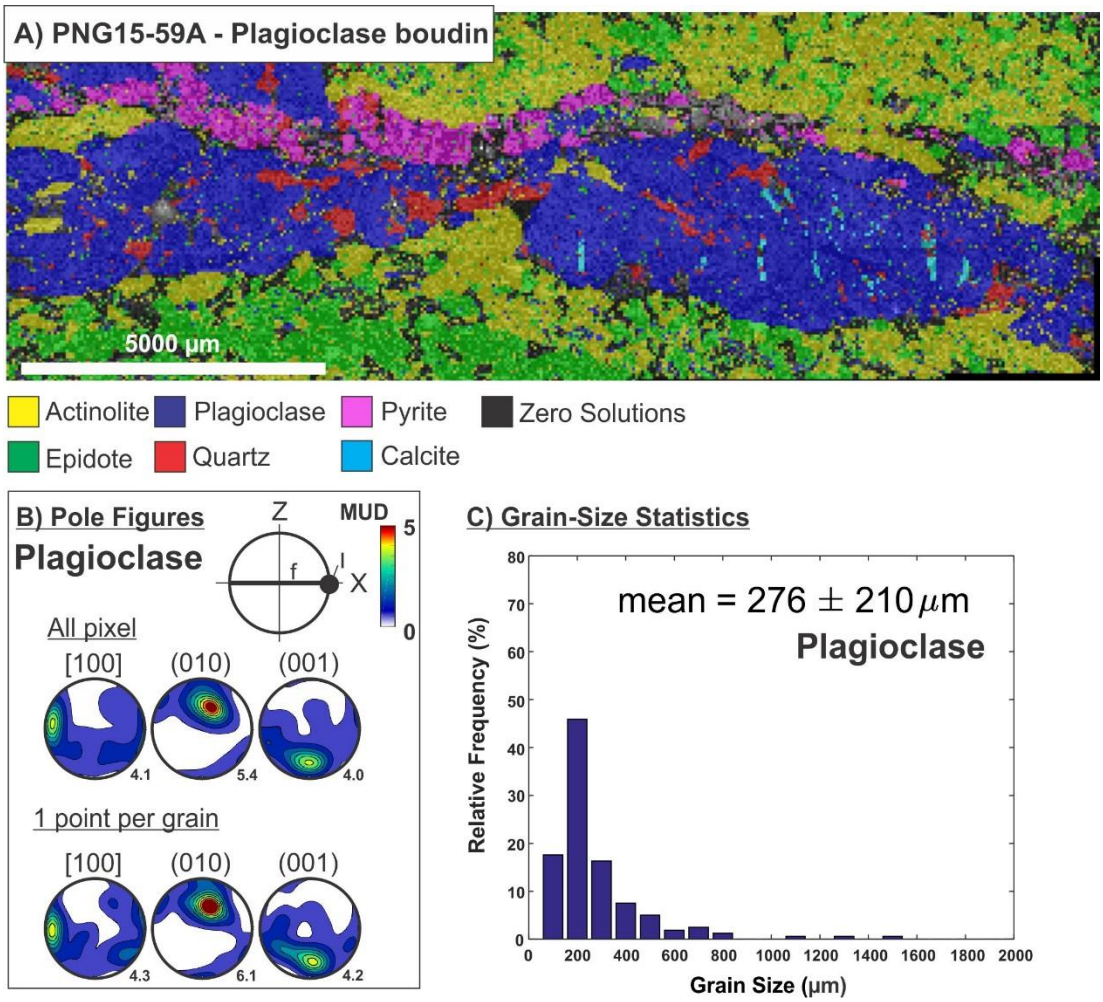

Figure S4.6. EBSD data for of albitic boudin in mylonite sample PNG15-59A (albite only; ~50 m south of the active Mai'iu fault trace). A) Phase map (50 µm step size). B) Contoured pole figures of selected crystallographic axes and poles in albite based on all pixels (top row) and based on one point per grain (bottom row). C) Albite grain size statistics.

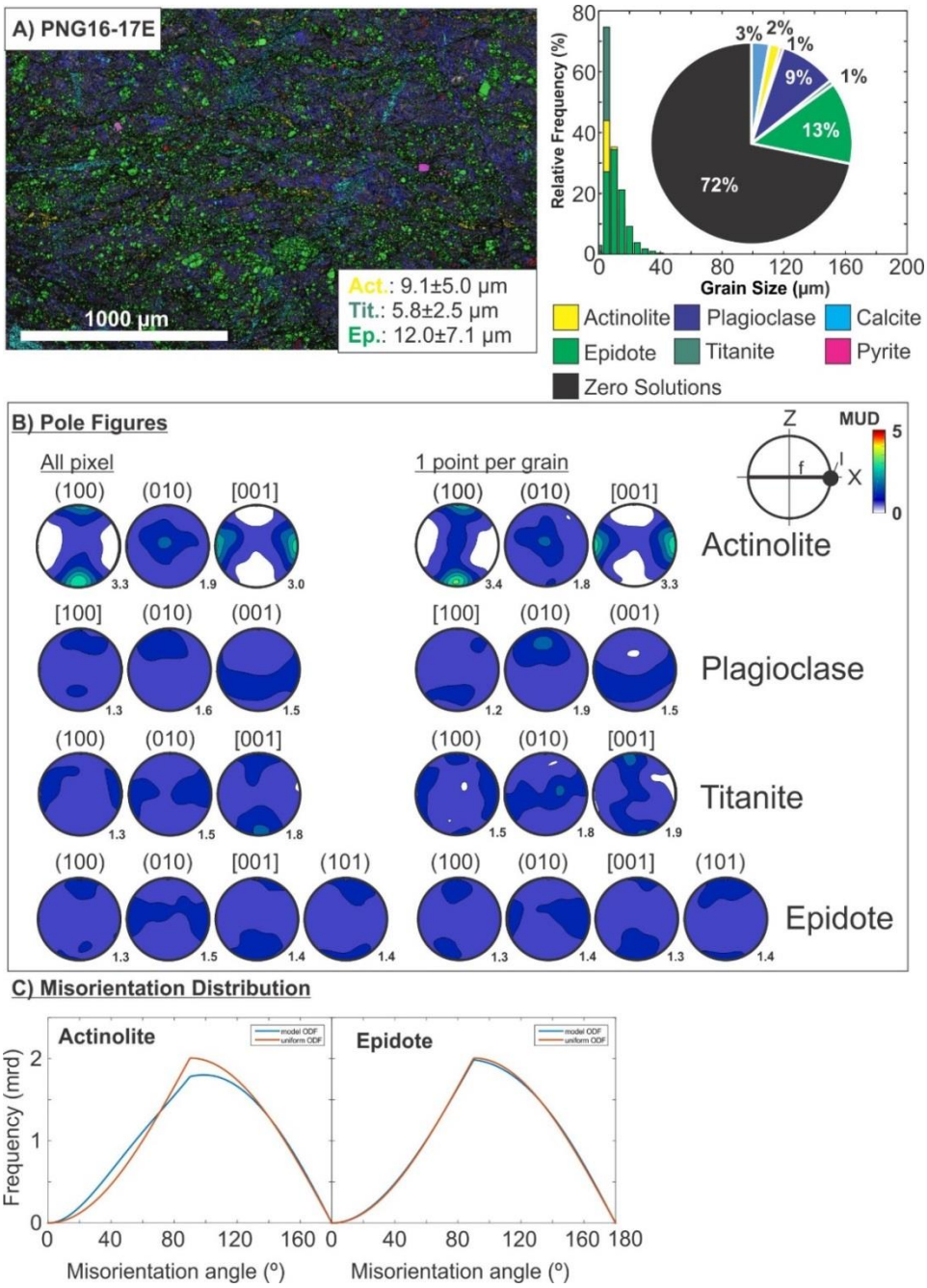

Figure S4.7. EBSD analysis of (ultra?)mylonite sample PNG16-17E (~50 cm structurally beneath the foliated cataclasite unit close to the inactive Mai'iu fault trace). A) EBSD-based phase map (1 µm step size) and average grain sizes of titanite, actinolite and epidote (left-hand site); grain-size histogram (relative frequency[%] vs. grain size [µm]) and phase fraction (%; pie diagram) of selected minerals (right-hand side). B) Contoured pole figures of selected crystallographic axes and poles; left—based on all pixels; right—based on one point per grain. MUD—Multiples of uniform distribution; l—lineation; f—foliation. C) Misorientation distribution plot (misorientation angle versus frequency [mrd=multiples of random density]) of selected minerals for uncorrelated grains (blue curves), and a theoretical random distribution (red curves). ODF—Orientation density functions.

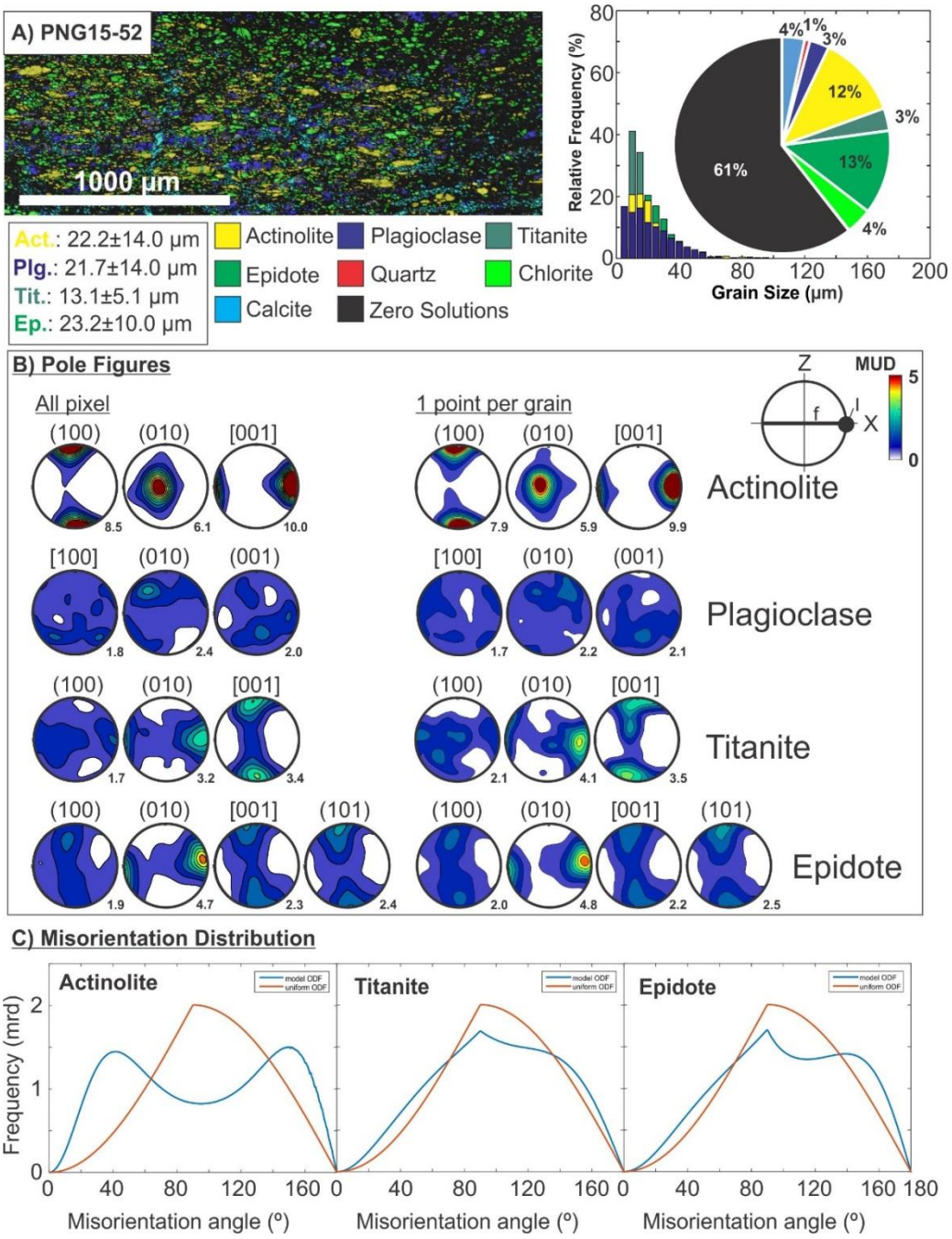

Figure S4.8. EBSD data for mylonite sample PNG15-52 (~5 m south of the active Mai'iu fault trace). A) EBSD-based phase map (2 µm step size) and average grain sizes of titanite, actinolite, epidote and albite (left-hand site); grain-size histogram (relative frequency[%] vs. grain size [µm]) and phase fraction (%; pie diagram) of selected minerals (right-hand side). B) Contoured pole figures of selected crystallographic axes and poles; left—based on all pixels; right—based on one point per grain. MUD—Multiples of uniform distribution; l—lineation; f—foliation. C) Misorientation distribution plot (misorientation angle versus frequency [mrd=multiples of random density]) of selected minerals for uncorrelated grains (blue curves), and a theoretical random distribution (red curves). ODF—Orientation density functions.

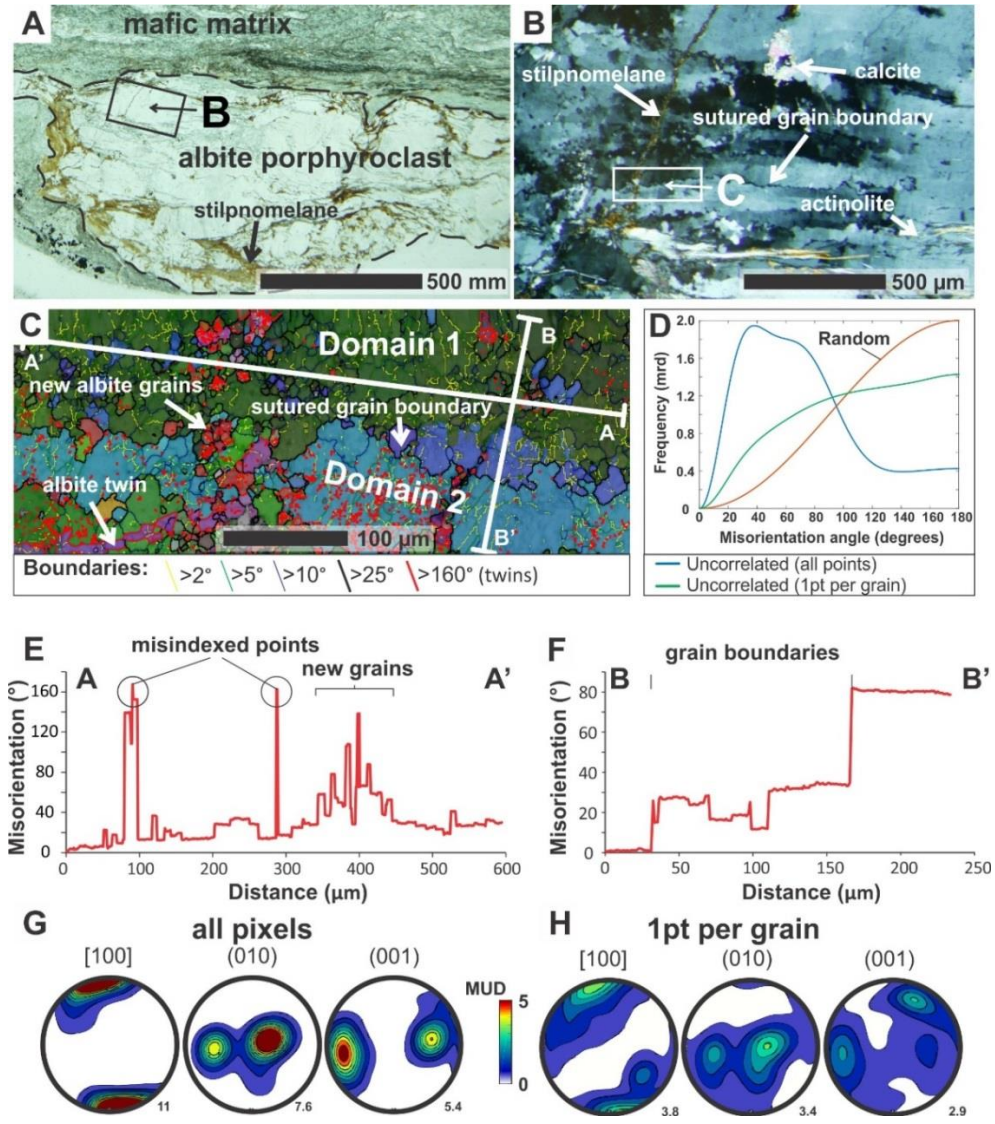

Figure S4.9. Microstructural analysis of an albite porphyroclast in the mafic mylonite sample PNG15-73. A) Optical photomicrograph of an albite porphyroclast (up to 2 cm in diameter). Stilpnomelane grew at the outer rim and along fractures of this porphyroclast. B) Optical photomicrograph (XPOL) of the deformed albite porphyroclast showing strong internal lattice distortion, intergrown actinolite fibres, and stilpnomelane ±calcite in fractures. C) EBSD (all Euler colors) map of the host albite grain (Domain 1), albite grain with bulged and sutured grain boundaries (Domain 2), and smaller albite aggregates (step size: 1 µm). D) Misorientation distribution plot (misorientation angle versus frequency [mrd=multiples of random density]) for all collected points and one point per grain (uncorrelated), and a theoretical random distribution. Note, misindexed points were excluded from this analysis. E) and F) misorientation profiles (misorientation angle relative to the starting point) across the different albite domains. G) and H) Lower-hemisphere, equal-area pole plots of selected crystallographic directions (Schmidt projection) of all collected points (pixels; mostly controlled by the orientation of the parent albite grain); and one point per grain (embraces the orientations of recrystallized grains in the analyzed section).

Foliated Cataclasites:

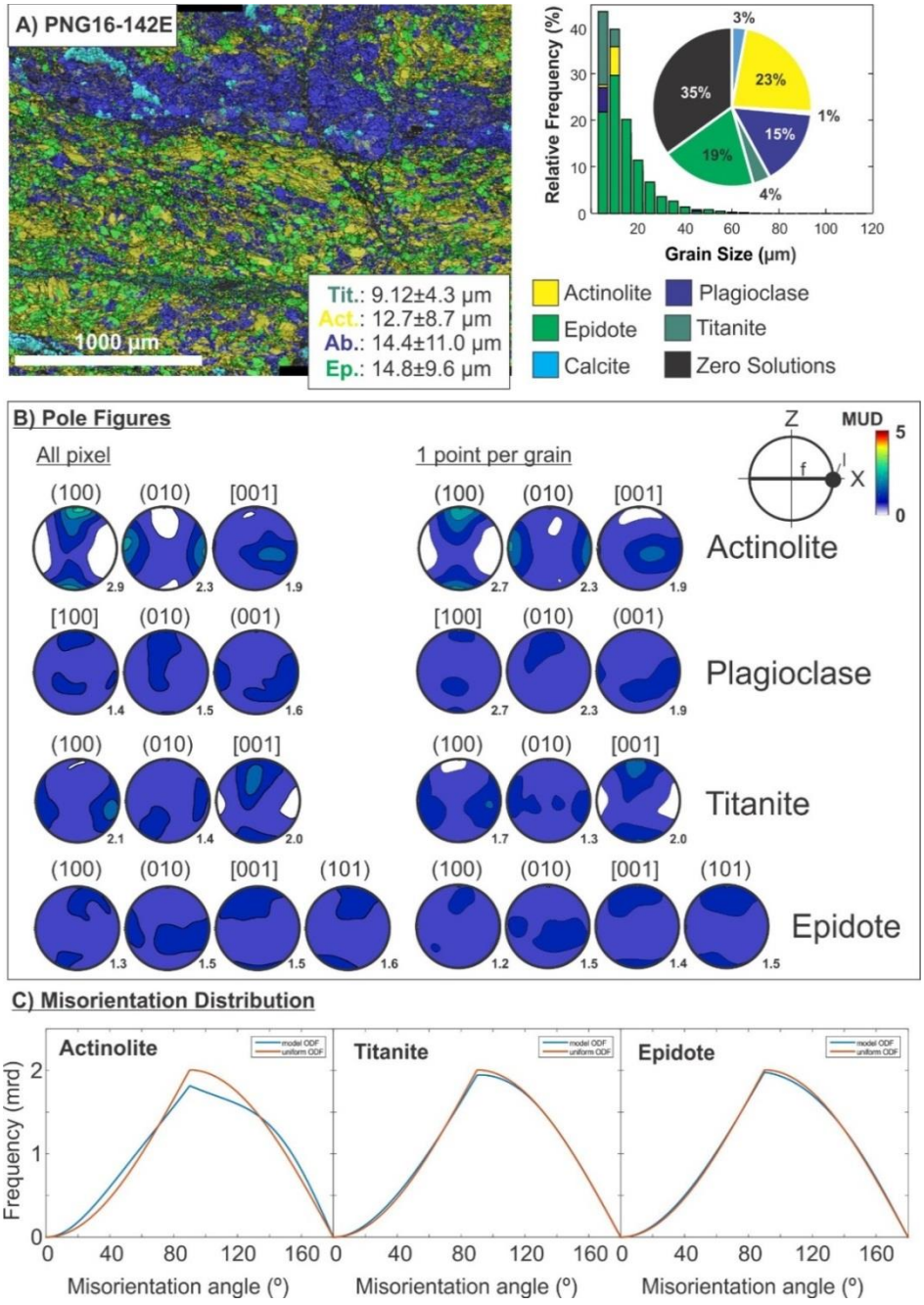

Figure S4.10. EBSD data for foliated cataclasite sample PNG16-142E (at active Mai'iu fault trace). A) EBSD-based phase map (2 µm step size) and average grain sizes of titanite, actinolite, epidote and albite (left-hand site); grain-size histogram (relative frequency[%] vs. grain size [µm]) and phase fraction (%; pie diagram) of selected minerals (right-hand side). B) Contoured pole figures of selected crystallographic axes and poles; left—based on all pixels; right—based on one point per grain. MUD—Multiples of uniform distribution; l—lineation; f—foliation. C) Misorientation distribution plot (misorientation angle versus frequency [mrd=multiples of random density]) of selected minerals for uncorrelated grains (blue curves), and a theoretical random distribution (red curves). ODF—Orientation density functions.

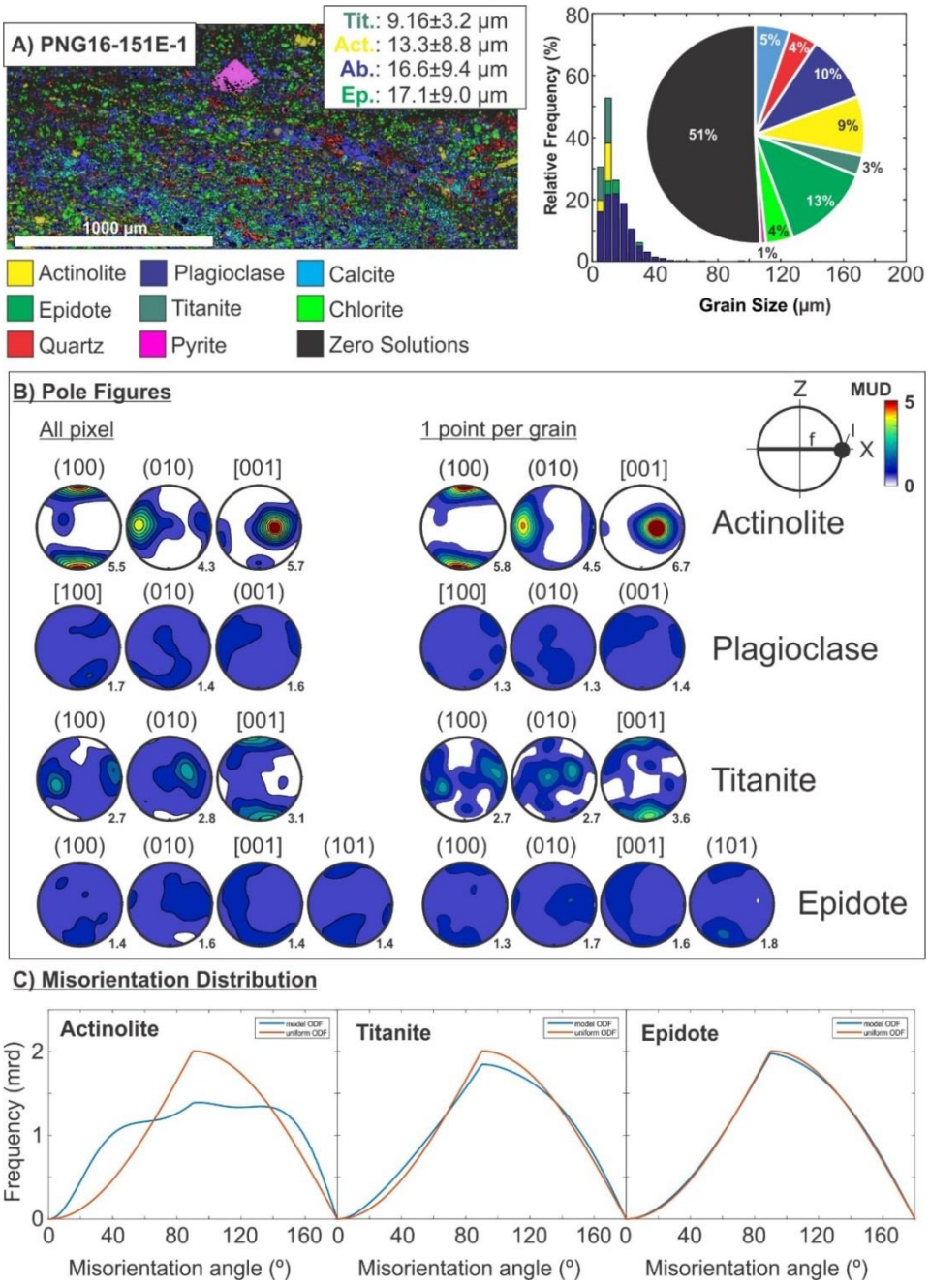

Figure S4.11. EBSD data for of foliated cataclasite sample PNG16-151E-1 (~2 m south of active Mai'iu fault trace). A) EBSD-based phase map (2 µm step size) and average grain sizes of titanite, actinolite, epidote and albite (left-hand site); grain-size histogram (relative frequency[%] vs. grain size [µm]) and phase fraction (%; pie diagram) of selected minerals (right-hand side). B) Contoured pole figures of selected crystallographic axes and poles; left—based on all pixels; right—based on one point per grain. MUD—Multiples of uniform distribution; l—lineation; f—foliation. C) Misorientation distribution plot (misorientation angle versus frequency [mrd=multiples of random density]) of selected minerals for uncorrelated grains (blue curves), and a theoretical random distribution (red curves). ODF—Orientation density functions.

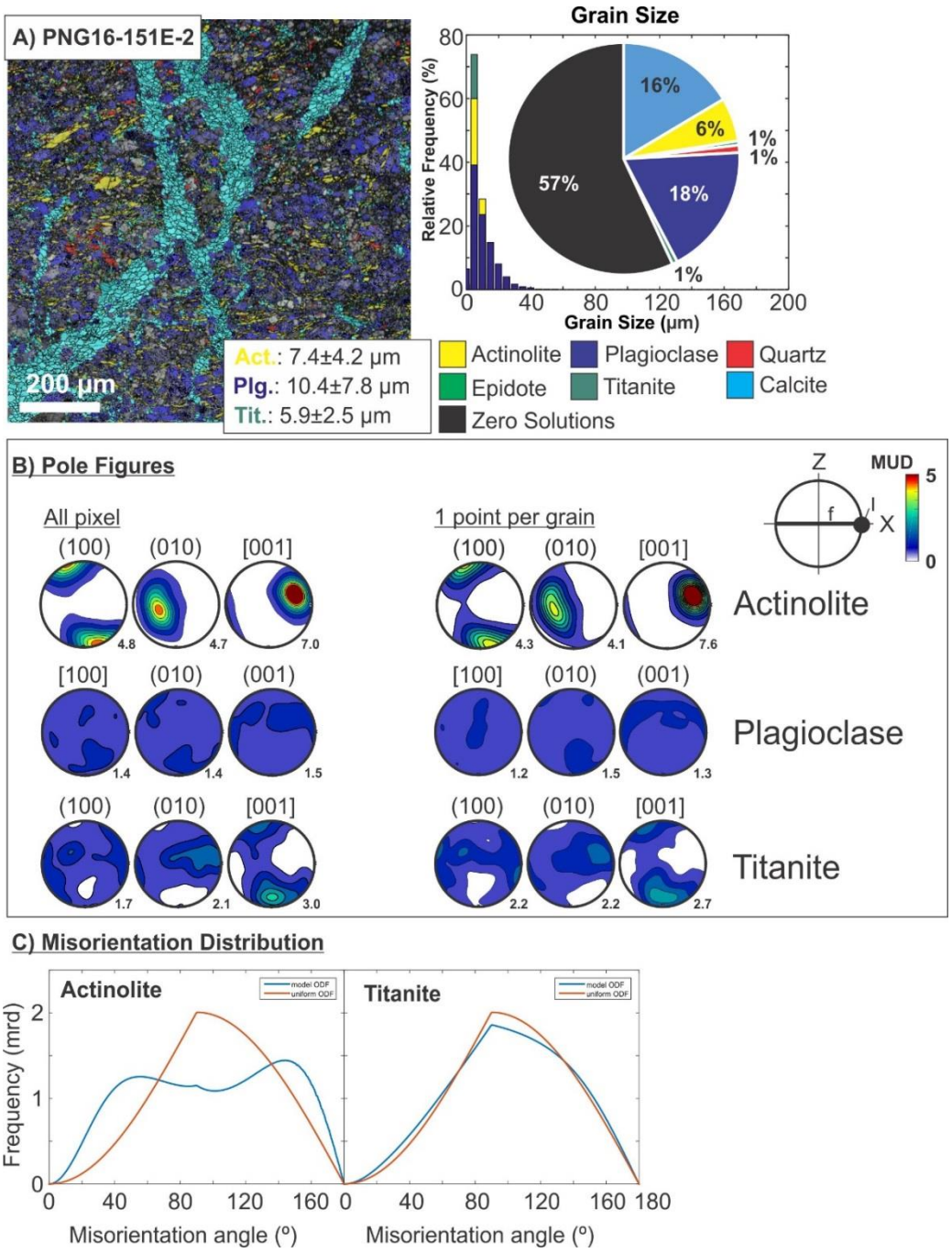

Figure S4.12. EBSD data for of foliated cataclasite sample PNG16-151E-2 (~2 m south of active Mai'iu fault trace). A) EBSD-based phase map (1 µm step size) and average grain sizes of titanite, actinolite and albite (left-hand site); grain-size histogram (relative frequency[%] vs. grain size [µm]) and phase fraction (%; pie diagram) of selected minerals (right-hand side). B) Contoured pole figures of selected crystallographic axes and poles; left—based on all pixels; right—based on one point per grain. MUD—Multiples of uniform distribution; l—lineation; f—foliation. C) Misorientation distribution plot (misorientation angle versus frequency [mrd=multiples of random density]) of selected minerals for uncorrelated grains (blue curves), and a theoretical random distribution (red curves). ODF—Orientation density functions.

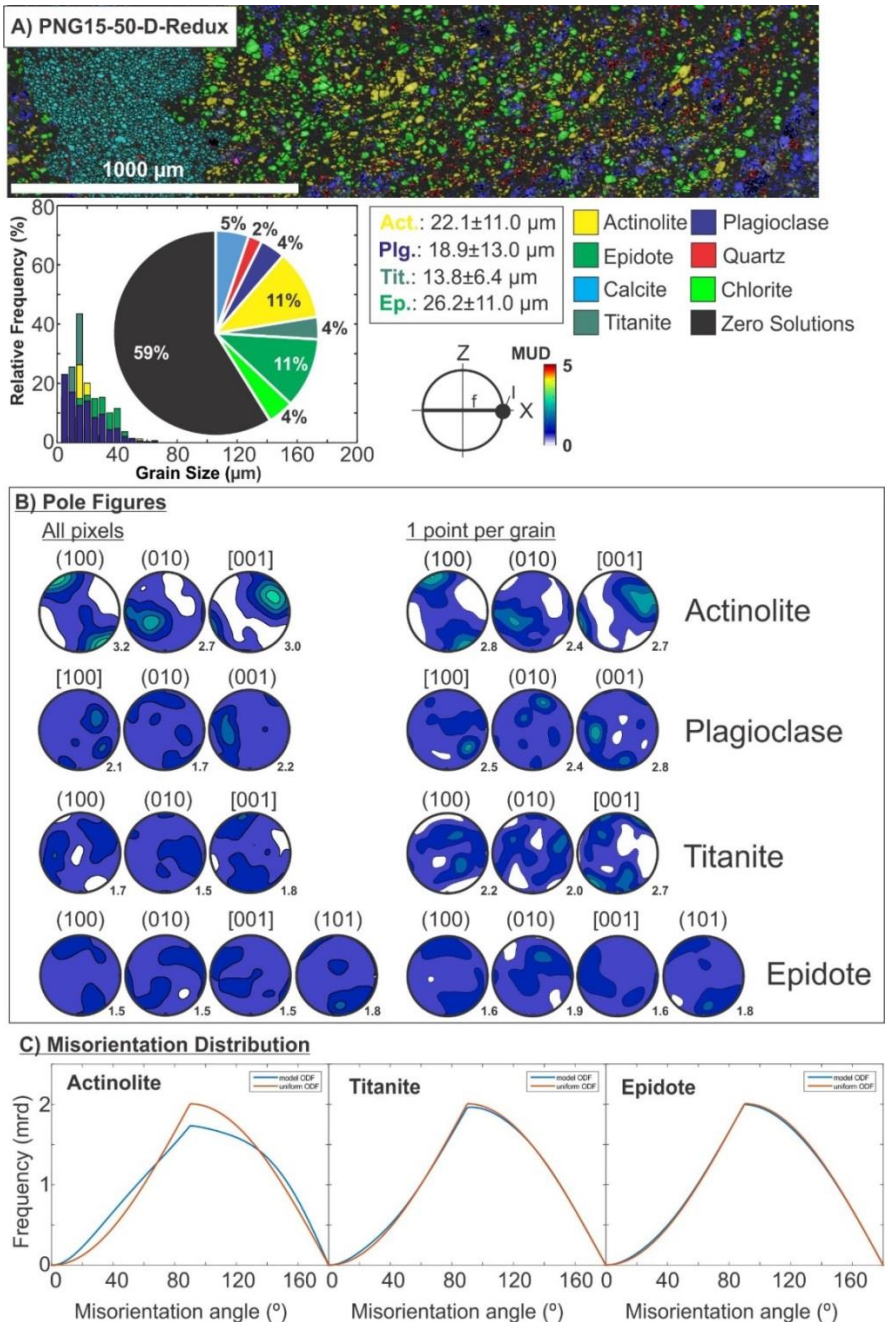

Figure S4.13. EBSD data for of foliated cataclasite sample PNG15-50D-Redux (~20 cm below ultracataclasite layer at active Mai'iu fault trace). A) EBSD-based phase map (2 µm step size; top); average grain sizes of titanite, actinolite, epidote and albite, grain-size histogram (relative frequency[%] vs. grain size [µm]) and phase fraction (%; pie diagram) of selected minerals (below phase map). B) Contoured pole figures of selected crystallographic axes and poles; left—based on all pixels; right—based on one point per grain. MUD—Multiples of uniform distribution; l—lineation; f—foliation. C) Misorientation distribution plot (misorientation angle versus frequency [mrd=multiples of random density]) of selected minerals for uncorrelated grains (blue curves), and a theoretical random distribution (red curves). ODF—Orientation density functions.

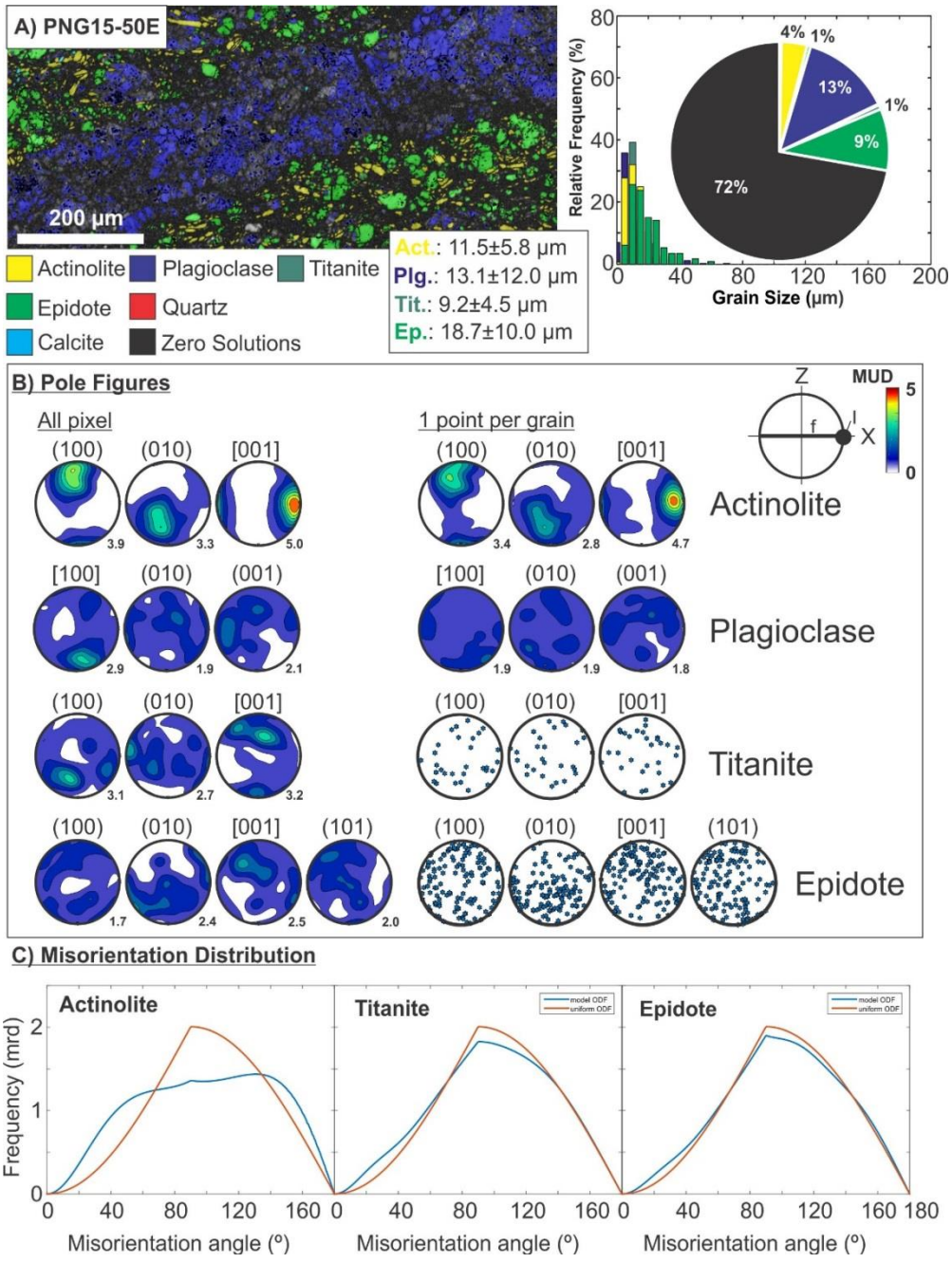

Figure S4.14. EBSD data for foliated cataclasite sample PNG15-50E (~20 cm below ultracataclasite layer at active Mai'iu fault trace). A) EBSD-based phase map (1 µm step size) and average grain sizes of titanite, actinolite, epidote and albite (left-hand site); grain-size histogram (relative frequency[%] vs. grain size [µm]) and phase fraction (%; pie diagram) of selected minerals (right-hand side). B) Contoured pole figures of selected crystallographic axes and poles; left—based on all pixels; right—based on one point per grain. MUD—Multiples of uniform distribution; l—lineation; f—foliation. C) Misorientation distribution plot (misorientation angle versus frequency [mrd=multiples of random density]) of selected minerals for uncorrelated grains (blue curves), and a theoretical random distribution (red curves). ODF—Orientation density functions.

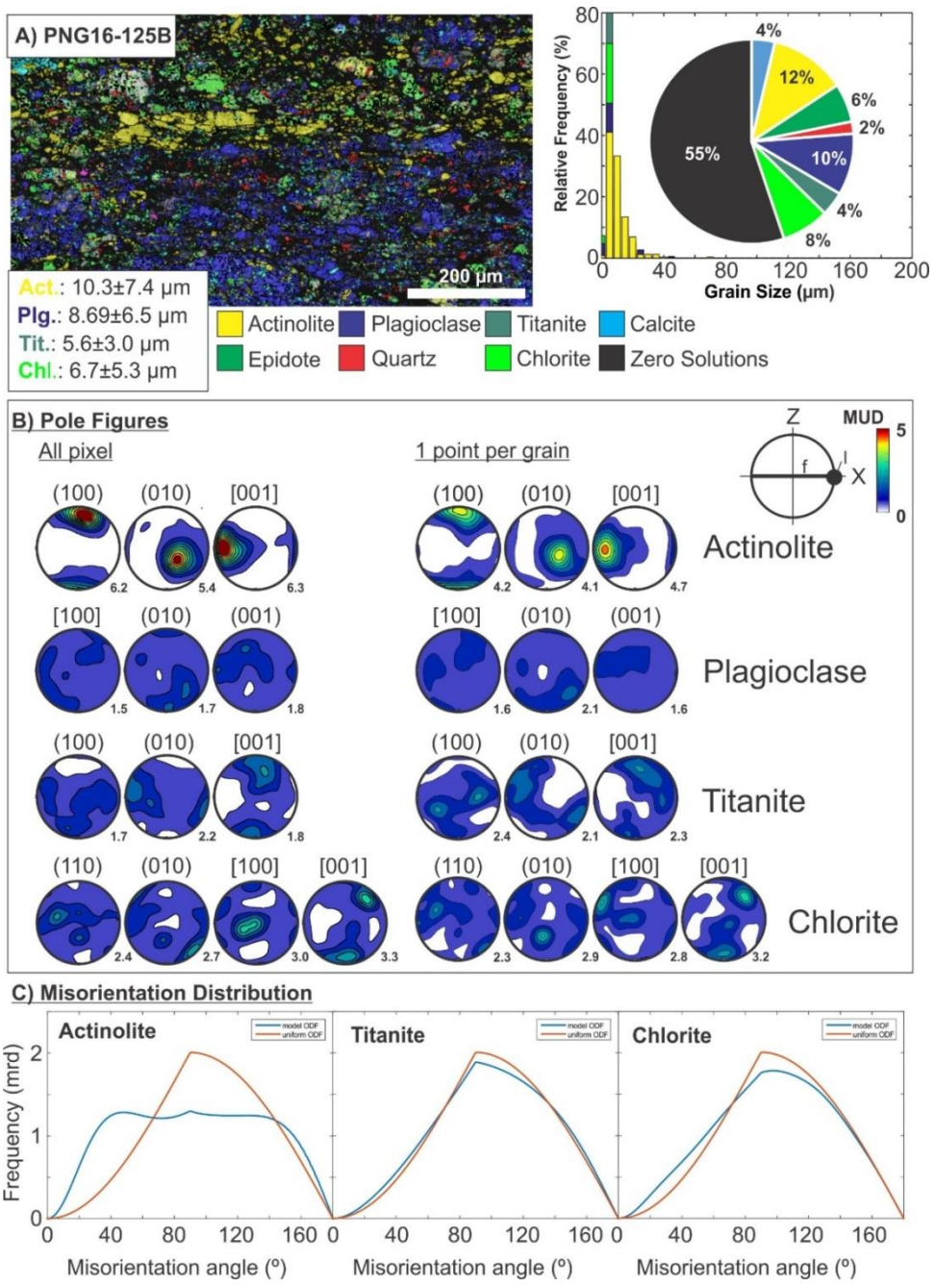

Figure S4.15. EBSD data for of cataclasite sample PNG16-125B (just south of active(?) Mai'iu fault trace, close to Gwoira fault). A) EBSD-based phase map (1 µm step size) and average grain sizes of titanite, actinolite, epidote and albite (left-hand site); grain-size histogram (relative frequency[%] vs. grain size [µm]) and phase fraction (%; pie diagram) of selected minerals (right-hand side). B) Contoured pole figures of selected crystallographic axes and poles; left—based on all pixels; right—based on one point per grain. MUD—Multiples of uniform distribution; l—lineation; f—foliation. C) Misorientation distribution plot (misorientation angle versus frequency [mrd=multiples of random density]) of selected minerals for uncorrelated grains (blue curves), and a theoretical random distribution (red curves). ODF—Orientation density functions.

Ultracataclasites:

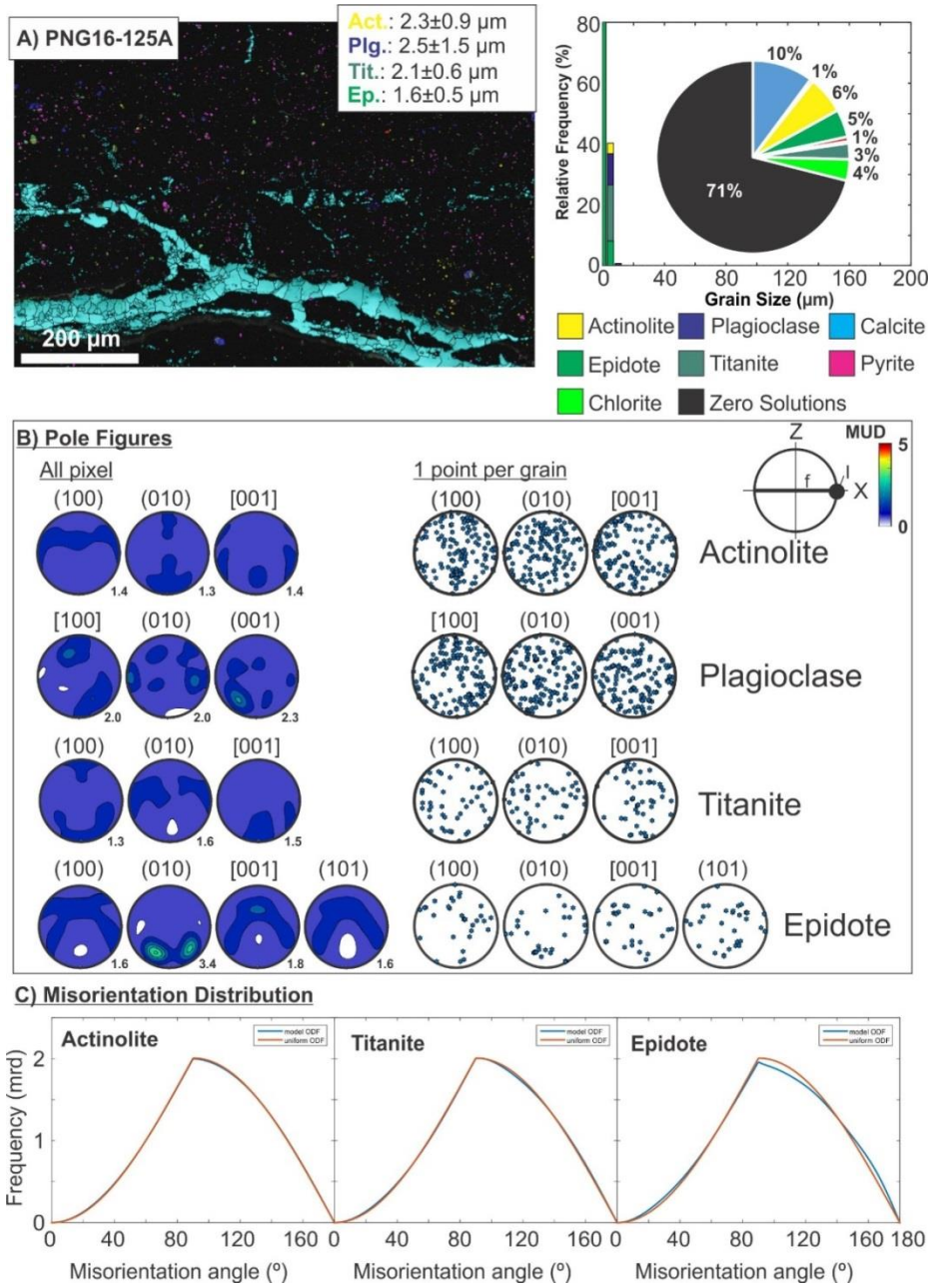

Figure S4.16. EBSD data for ultracataclasite sample PNG16-125A. A) EBSD-based phase map (0.5 µm step size) and average grain sizes of titanite, actinolite, epidote and albite (left-hand site); grain-size histogram (relative frequency[%] vs. grain size [µm]) and phase fraction (%; pie diagram) of selected minerals (right-hand side). B) Contoured pole figures of selected crystallographic axes and poles; left—based on all pixels; right—based on one point per grain. MUD—Multiples of uniform distribution; l—lineation; f—foliation. C) Misorientation distribution plot (misorientation angle versus frequency [mrd=multiples of random density]) of selected minerals for uncorrelated grains (blue curves), and a theoretical random distribution (red curves). ODF—Orientation density functions.

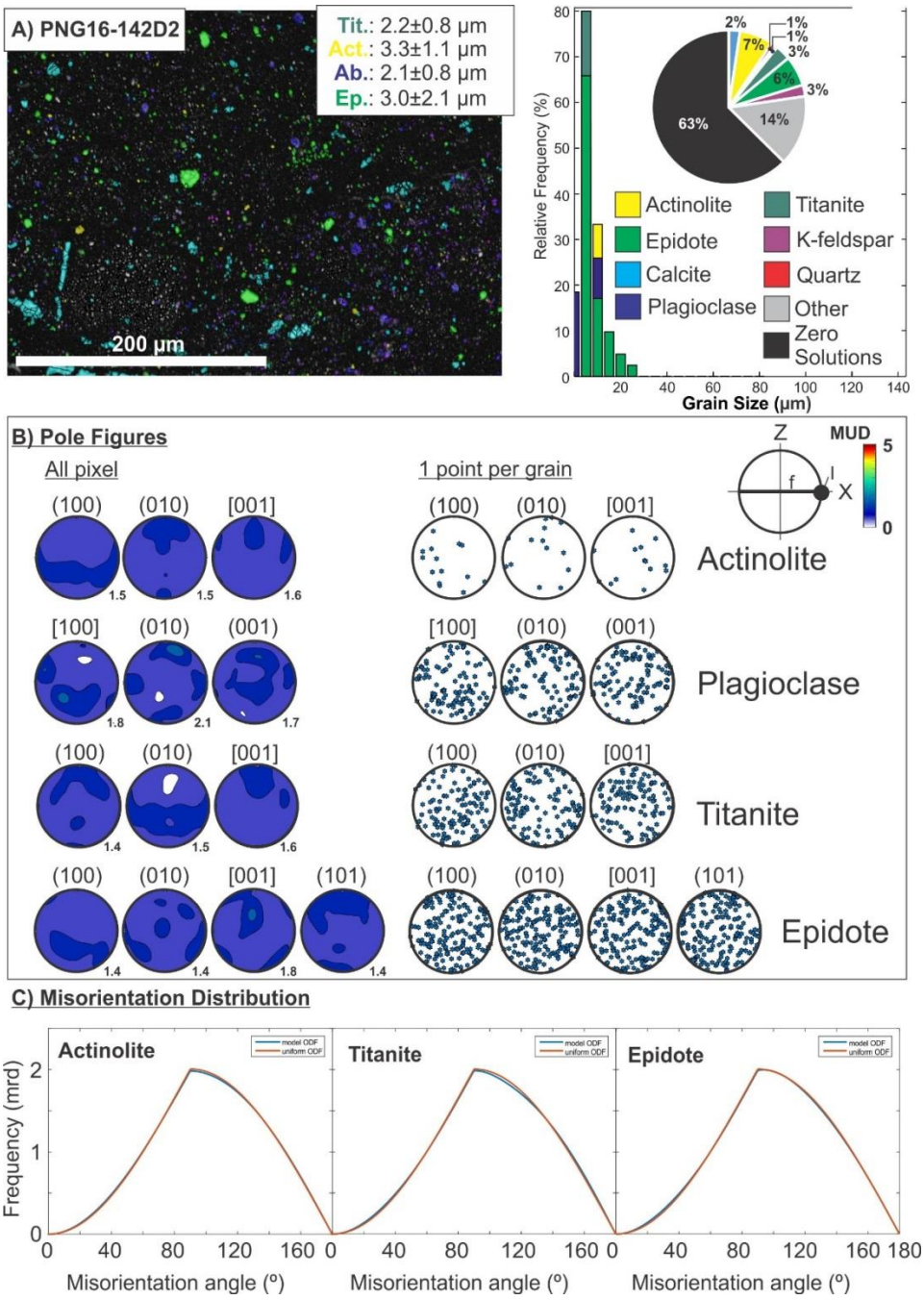

Figure S4.17. EBSD data for ultracataclasite sample PNG16-142D2. A) EBSD-based phase map (0.6 µm step size) and average grain sizes of titanite, actinolite, epidote and albite (left-hand site); grain-size histogram (relative frequency[%] vs. grain size [µm]) and phase fraction (%; pie diagram) of selected minerals (right-hand side). B) Contoured pole figures of selected crystallographic axes and poles; left—based on all pixels; right—based on one point per grain. MUD—Multiples of uniform distribution; l—lineation; f—foliation. C) Misorientation distribution plot (misorientation angle versus frequency [mrd=multiples of random density]) of selected minerals for uncorrelated grains (blue curves), and a theoretical random distribution (red curves). ODF—Orientation density functions.

Mafic Gouges:

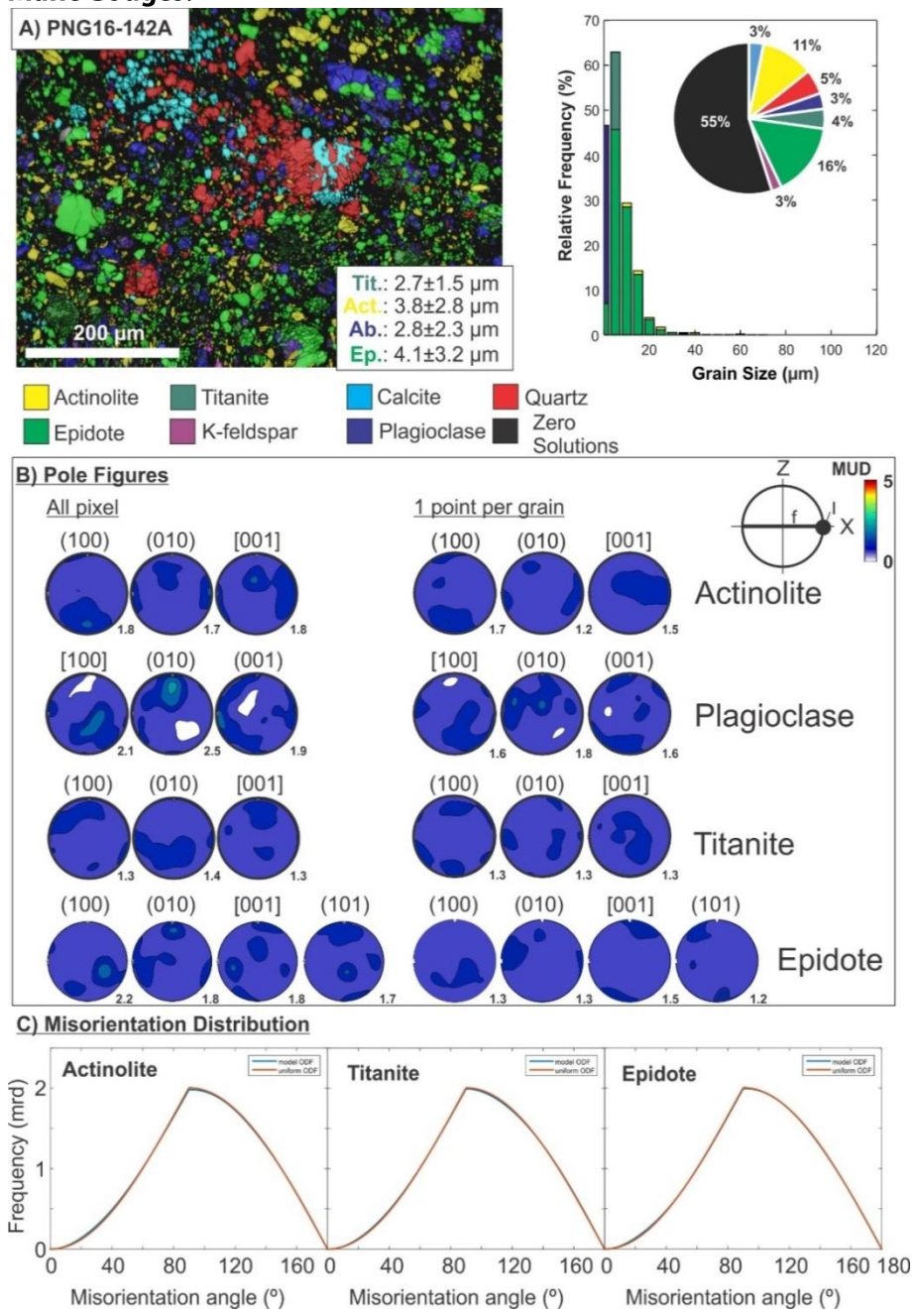

Figure S4.18. EBSD data for gouge sample PNG16-142A (active Mai'iu fault trace). A) EBSD-based phase map (0.5 µm step size) and average grain sizes of titanite, actinolite, epidote and albite (left-hand site); grain-size histogram (relative frequency[%] vs. grain size [µm]) and phase fraction (%; pie diagram) of selected minerals (right-hand side). B) Contoured pole figures of selected crystallographic axes and poles; left—based on all pixels; right—based on one point per grain. MUD—Multiples of uniform distribution; l—lineation; f—foliation. C) Misorientation distribution plot (misorientation angle versus frequency [mrd=multiples of random density]) of selected minerals for uncorrelated grains (blue curves), and a theoretical random distribution (red curves). ODF—Orientation density functions.

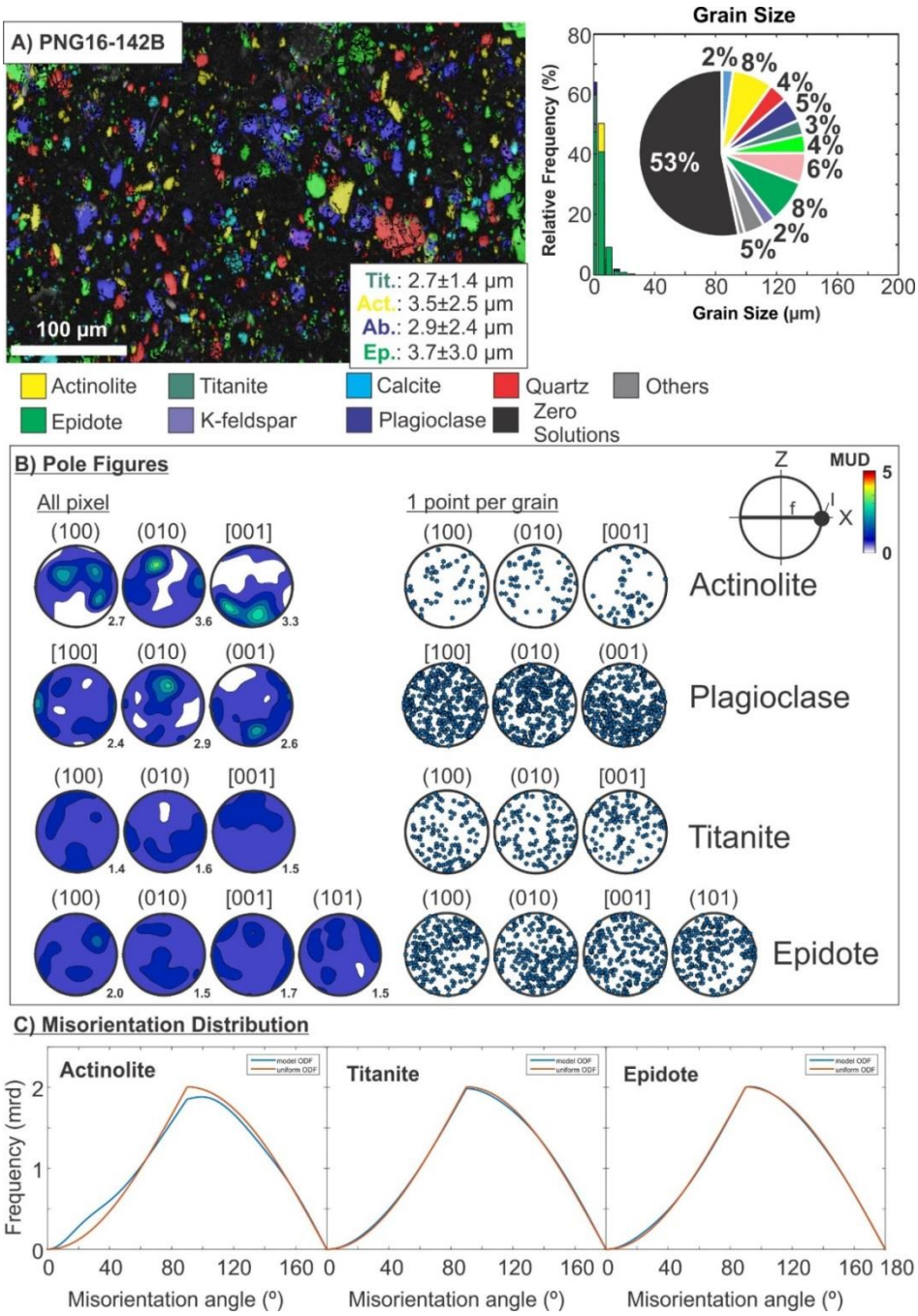

Figure S4.19. EBSD data for of gouge sample PNG16-142B (active Mai'iu fault trace). A) EBSD-based phase map (0.6 µm step size) and average grain sizes of titanite, actinolite, epidote and albite (left-hand site); grain-size histogram (relative frequency[%] vs. grain size [µm]) and phase fraction (%; pie diagram) of selected minerals (right-hand side). B) Contoured pole figures of selected crystallographic axes and poles; left—based on all pixels; right—based on one point per grain. MUD—Multiples of uniform distribution; l—lineation; f—foliation. C) Misorientation distribution plot (misorientation angle versus frequency [mrd=multiples of random density]) of selected minerals for uncorrelated grains (blue curves), and a theoretical random distribution (red curves). ODF—Orientation density functions.

Non-mylonitic mafic schist:

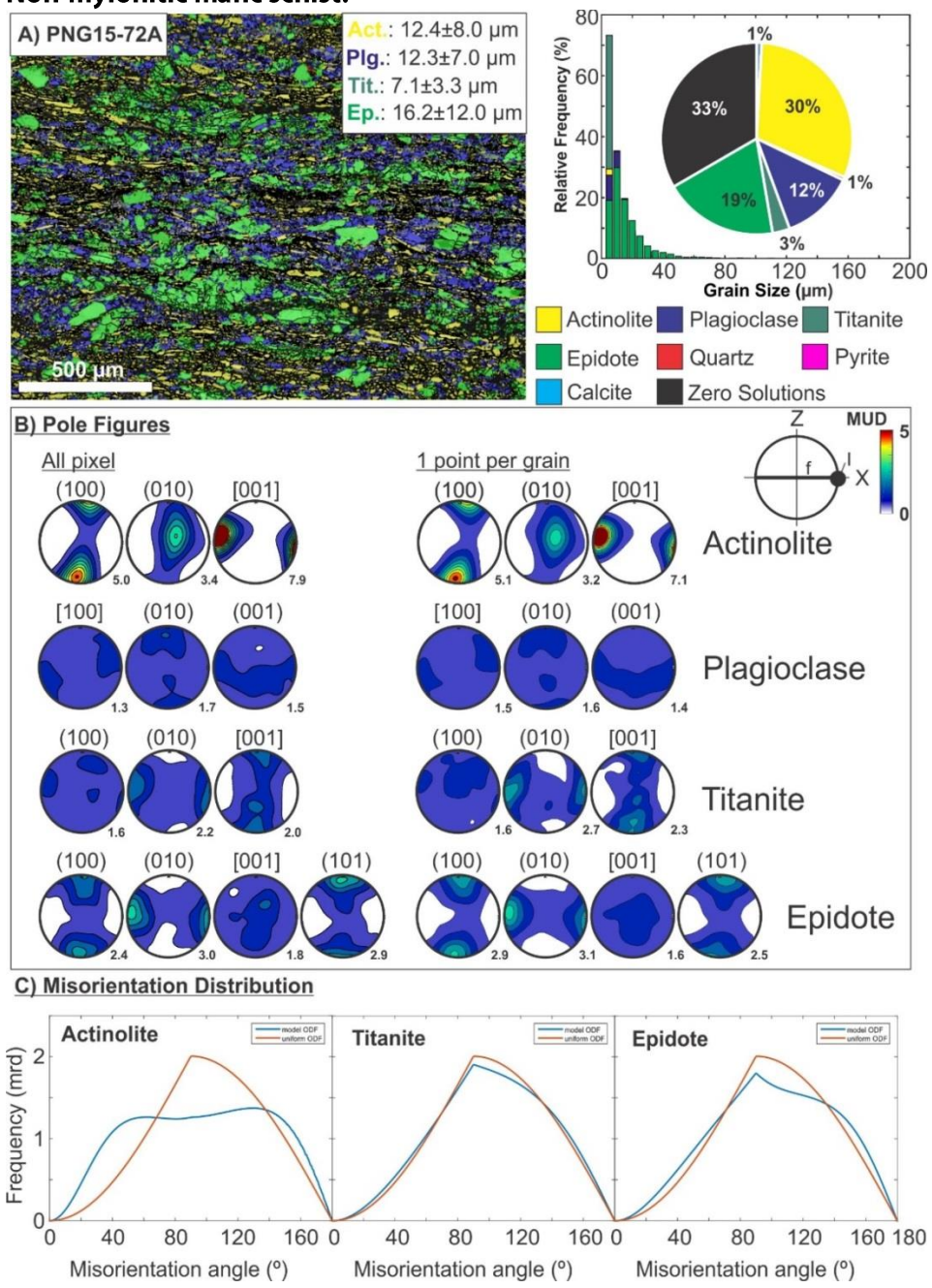

Figure S4.20. EBSD data for a non-mylonitic schist (PNG15-72A). A) EBSD-based phase map (2 µm step size) and average grain sizes of titanite, actinolite, epidote and albite (left-hand site); grain-size histogram (relative frequency[%] vs. grain size [µm]) and phase fraction (%; pie diagram) of selected minerals (right-hand side). B) Contoured pole figures of selected crystallographic axes and poles; left—based on all pixels; right—based on one point per grain. MUD—Multiples of uniform distribution; l—lineation; f—foliation. C) Misorientation distribution plot (misorientation angle versus frequency [mrd=multiples of random density]) of selected minerals for uncorrelated grains (blue curves), and a theoretical random distribution (red curves). ODF—Orientation density functions.

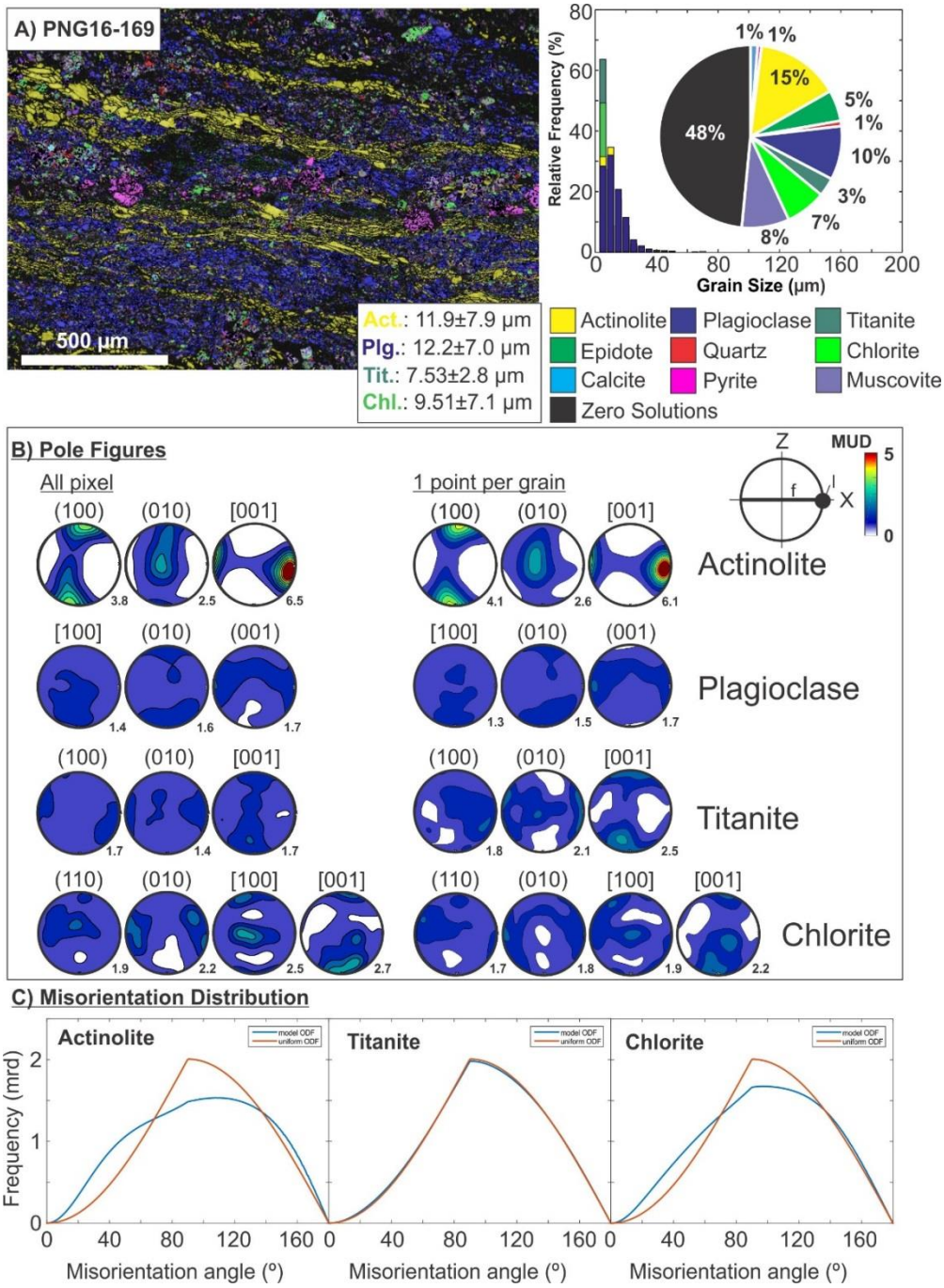

Figure S4.21. EBSD data for a non-mylonitic schist (~5.7 km south of the active Mai'iu fault trace; PNG16-169). A) EBSD-based phase map (1.5 µm step size) and average grain sizes of titanite, actinolite and albite (left-hand site); grain-size histogram (relative frequency[%] vs. grain size [µm]) and phase fraction (%; pie diagram) of selected minerals (right-hand side). B) Contoured pole figures of selected crystallographic axes and poles; left—based on all pixels; right—based on one point per grain. MUD—Multiples of uniform distribution; l—lineation; f—foliation. C) Misorientation distribution plot (misorientation angle versus frequency [mrd=multiples of random density]) of selected minerals for uncorrelated grains (blue curves), and a theoretical random distribution (red curves). ODF—Orientation density functions.

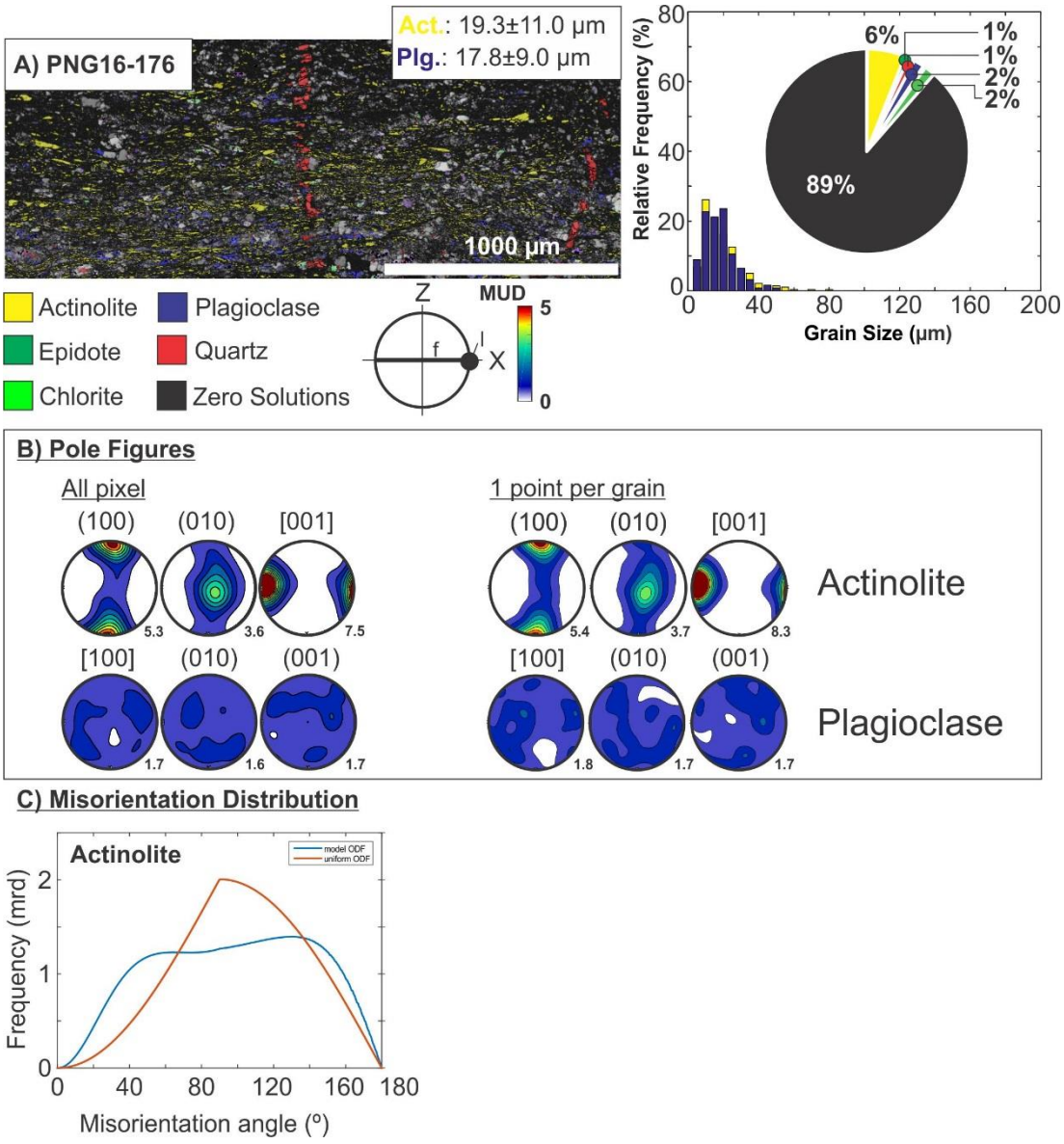

Figure S4.22. EBSD data for a non-mylonitic schist (~4.5 km south of the active Mai'iu fault trace; PNG16-176). A) EBSD-based phase map (2 µm step size) and average grain sizes of actinolite and albite (left-hand site); grain-size histogram (relative frequency[%] vs. grain size [µm]) and phase fraction (%; pie diagram) of selected minerals (right-hand side). B) Contoured pole figures of selected crystallographic axes and poles; left—based on all pixels; right—based on one point per grain. MUD—Multiples of uniform distribution; l—lineation; f—foliation. C) Misorientation distribution plot (misorientation angle versus frequency [mrd=multiples of random density]) of selected minerals for uncorrelated grains (blue curves), and a theoretical random distribution (red curves). ODF—Orientation density functions.

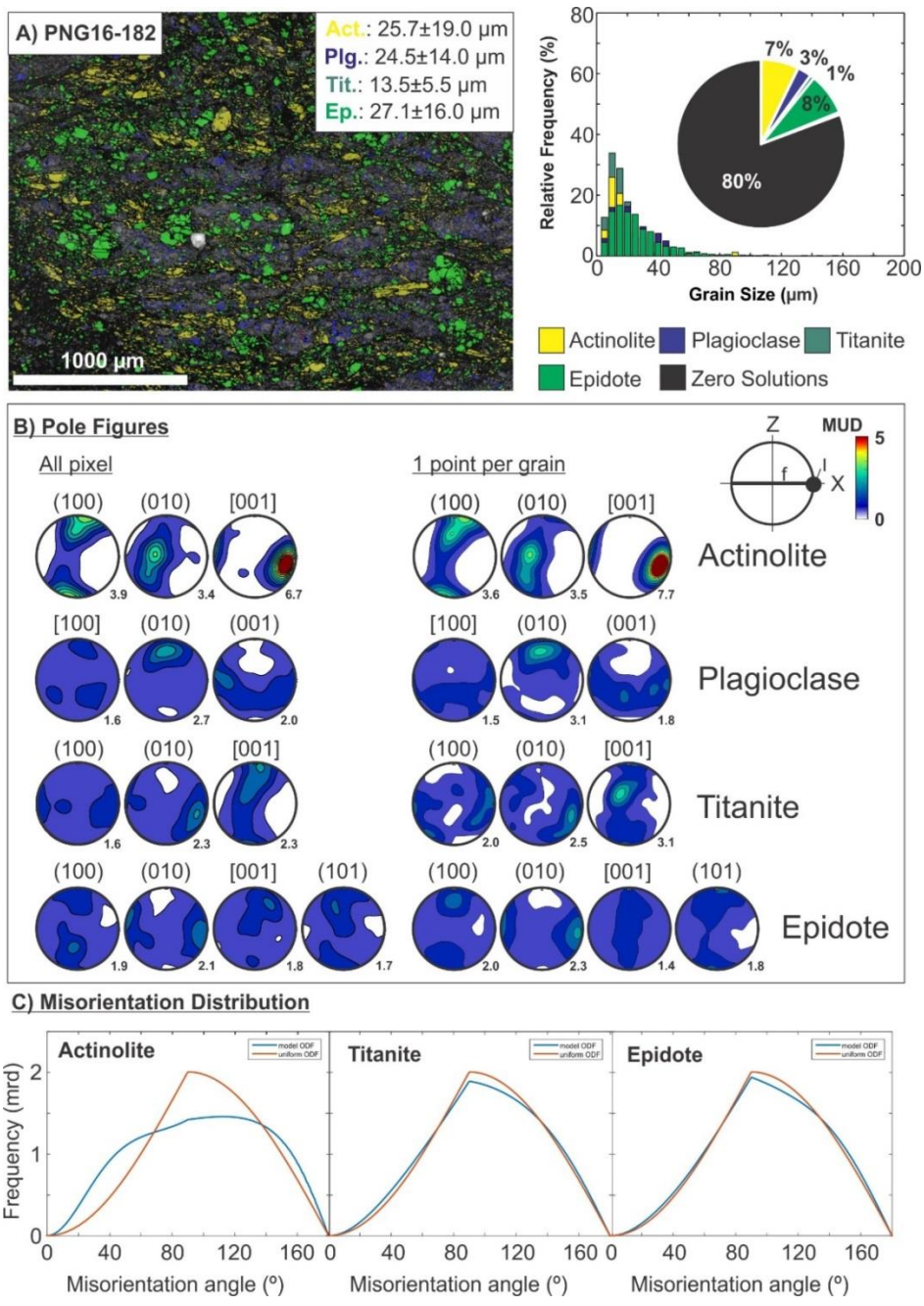

Figure S4.23. EBSD data for a non-mylonitic schist (~1.8 km south of the active Mai'iu fault trace; PNG16-182). A) EBSD-based phase map (2 µm step size) and average grain sizes of titanite, actinolite, epidote and albite (left-hand site); grain-size histogram (relative frequency[%] vs. grain size [µm]) and phase fraction (%; pie diagram) of selected minerals (right-hand side). B) Contoured pole figures of selected crystallographic axes and poles; left—based on all pixels; right—based on one point per grain. MUD—Multiples of uniform distribution; l—lineation; f—foliation. C) Misorientation distribution plot (misorientation angle versus frequency [mrd=multiples of random density]) of selected minerals for uncorrelated grains (blue curves), and a theoretical random distribution (red curves). ODF—Orientation density functions.

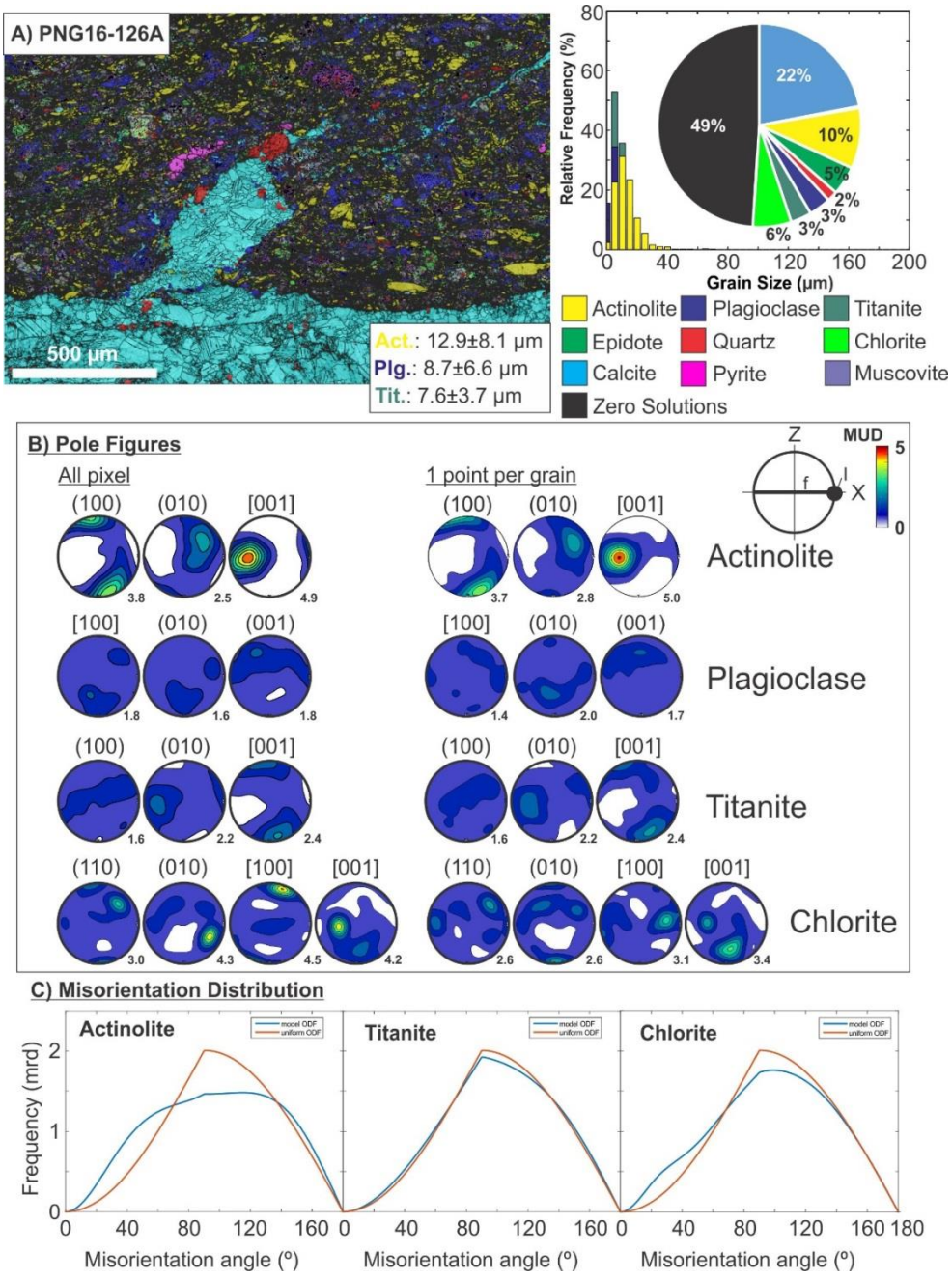

Figure S4.24. EBSD data for of a non-mylonitic schist (just south of active(?) Mai'iu fault trace, close to Gwoira fault; PNG16-126A). A) EBSD-based phase map (0.75 µm step size) and average grain sizes of titanite, actinolite and albite (left-hand site); grain-size histogram (relative frequency[%] vs. grain size [µm]) and phase fraction (%; pie diagram) of selected minerals (right-hand side). B) Contoured pole figures of selected crystallographic axes and poles; left—based on all pixels; right—based on one point per grain. MUD—Multiples of uniform distribution; l—lineation; f—foliation. C) Misorientation distribution plot (misorientation angle versus frequency [mrd=multiples of random density]) of selected minerals for uncorrelated grains (blue curves), and a theoretical random distribution (red curves). ODF—Orientation density functions.

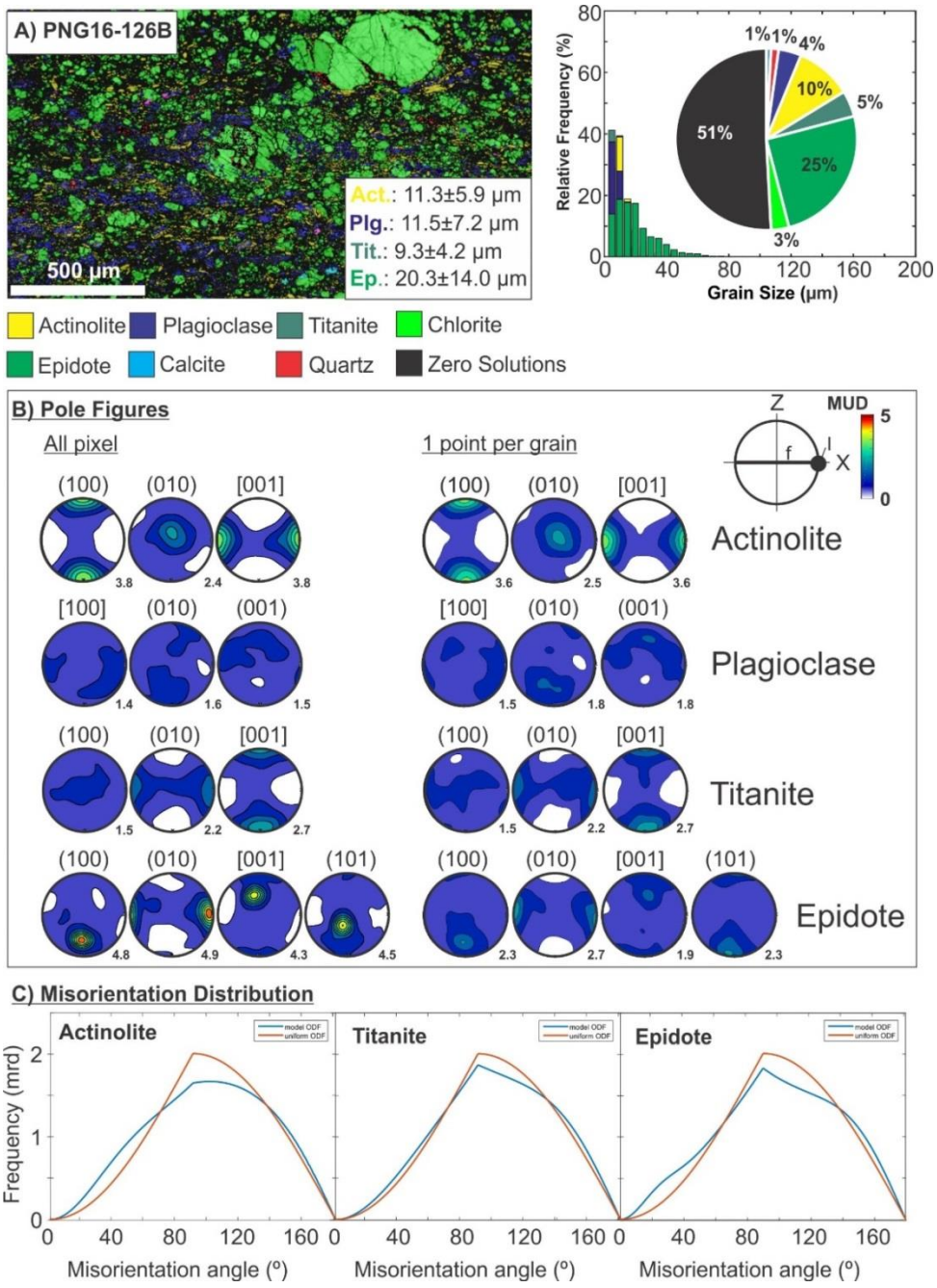

Figure S4.25. EBSD data for a non-mylonitic schist (just south of active(?) Mai'iu fault trace, close to Gwoira fault; PNG16-126B). A) EBSD-based phase map (1. 5 µm step size) and average grain sizes of titanite, actinolite, epidote and albite (left-hand site); grain-size histogram (relative frequency[%] vs. grain size [µm]) and phase fraction (%; pie diagram) of selected minerals (right-hand side). B) Contoured pole figures of selected crystallographic axes and poles; left—based on all pixels; right—based on one point per grain. MUD—Multiples of uniform distribution; l—lineation; f—foliation. C) Misorientation distribution plot (misorientation angle versus frequency [mrd=multiples of random density]) of selected minerals for uncorrelated grains (blue curves), and a theoretical random distribution (red curves). ODF—Orientation density functions.

Text S5. Temperature-Dependent Magnetic Susceptibility Experiment on Ultracataclasite

Temperature-dependent magnetic susceptibility experiments were conducted on the ultracataclasite sample PNG16-142D on a Bartington MS2 furnace system at the paleomagnetic laboratory at the School of Chemical and Physical Sciences, Victoria University of Wellington, in order to determine the Curie temperature(s) of the constituent ferromagnetic/ferrimagnetic phase(s) and therefore the magnetic mineralogy of this sample. We crushed the sample to a fine powder with mortar and pestle and extracted ~3.5 g of material for the sample holder. The extracted material was heated and cooled and its magnetic susceptibility was monitored throughout this process. The magnetic susceptibility was measured once the material in the sample holder reached 40°C, with measurements taken every 10°C. A peak temperature of 700°C was set for the experiment, before cooling back to 40°C. The results of this experiment are shown in Figure S5.1 and additional SEM back-scatter images and EDS analyses of the ultracataclasite (PNG16-142D) and magnetite-bearing veins and clasts in Figure S5.2, Figure S5.3, Figure S5.4 and Figure S5.5.

The thermomagnetic curves of the ultracataclasite sample at pressures of 1 atm are nearly reversible suggesting that up to temperatures of 700°C, no alteration occurred to the magnetic mineralogy during the experiment and none of the paramagnetic phases altered to ferromagnetic/ferromagnetic ones (Figure S5.1). During heating we observe an almost linear increase in magnetic susceptibility up to 380°C, above where the magnetic susceptibility shows a sharp linear increase up to 480°C. A peak with little variation of magnetic susceptibility is evident between 490 and 520°C just below the magnetite Curie point (Hopkinson peak). The susceptibility curve shows a strong drop from ~540°C down to 580°C and shallows to a Curie temperature of ~620–640°C close to the one of maghemite (TC≈645°C; Özdemir, 1990; Dunlop & Özdemir, 1997). The cooling run is below the heating run and shows a sharp increase in magnetic susceptibility from ~600°C to 500°C and reaches a plateau at ~480°C. The susceptibility drops again at ~450°C and the curve starts to flatten around ~300°C. We infer from this experiment that the principal magnetic mineral in the ultracataclasite is a stable (reversible heating and cooling curves), single domain (fine grained) magnetite. The observed Curie temperature above 580°C and below 645°C indicates cation deficient magnetite, slightly oxidized to maghemite (Özdemir & Banerjee, 1984; Dunlop & Özdemir, 1997).

SEM-EDS analyses show that opaque minerals occur as veins and coatings of and/or swirled into rounded fragments of ultracataclasite in the ultracataclasite matrix (Figure S5.2). Single, µm-sized opaque grains are rare in the ultracataclasites. Elemental analyses by EDS of the fine-grained opaque veins show high concentrations of Fe and small amounts of Ti, Si, K, Al and Mg (Figure S5.3, Figure S5.4). While the mineralogy of the opaque veins cannot be unambiguously identified using EDS, we infer that magnetite in the veins is too fine-grained (<1 µm diameter) to be imaged using that method; moreover, it has probably been in part oxidized to maghemite and intermingled with the ultra-fine grained, smectite-rich ultracataclasite matrix.

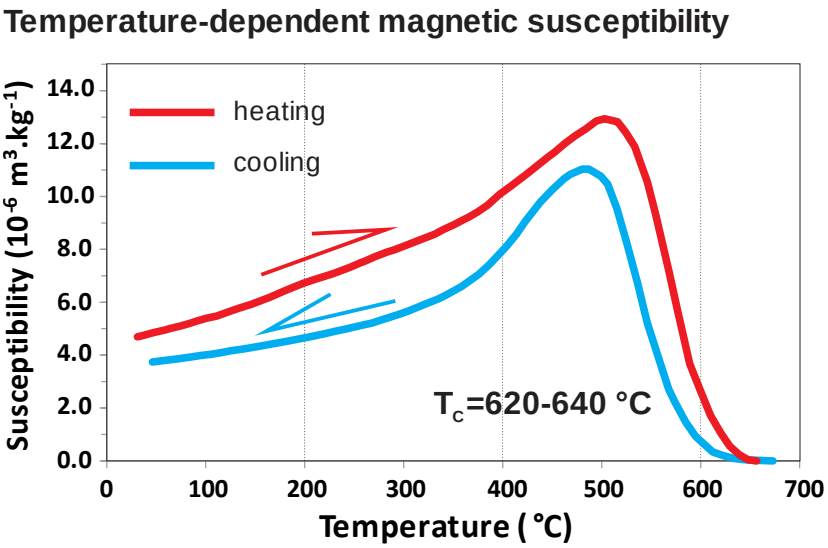

Figure S5.1. Curves of temperature versus magnetic susceptibility for sample PNG16-142D (ultracataclasite). The red and blue lines denote heating and cooling, respectively, from 40°C to 700°C and vice versa. T_C refers to the Curie temperature.

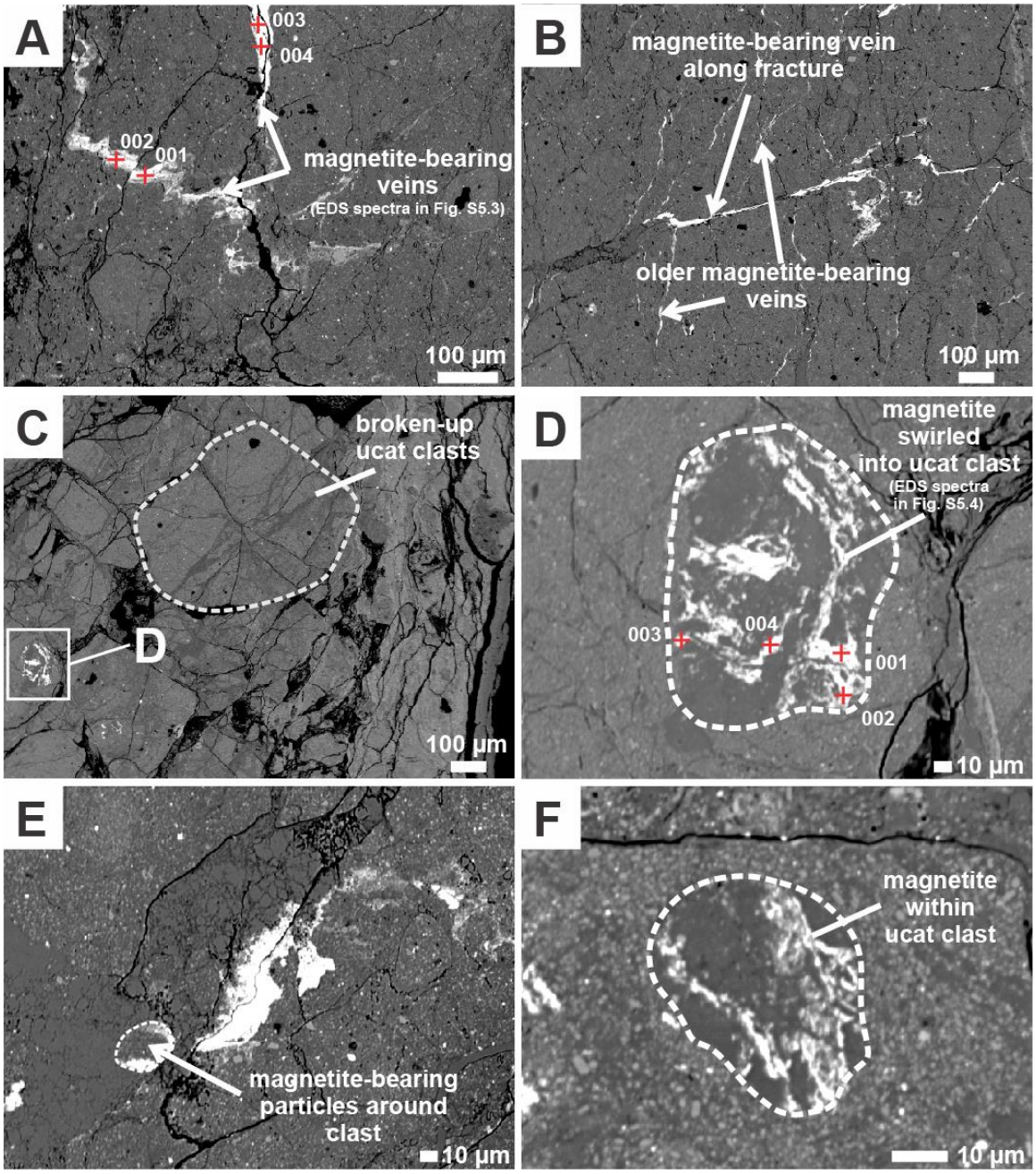

Figure S5.2. Backscatter electron images of magnetite-bearing veins and clasts in ultracataclasite (PNG16-142D). Magnetite appears white on the images. A) Magnetite in veins in association with fractured ultracataclasite and within the non-fractured ultracataclasite. Sample spots for the EDS analysis are indicated by red crosses. The spectra can be seen in Figure S5.3. B) Magnetite-bearing veins along fractures in the ultracataclasite. C) Broken ultracataclasites clast and an older, reworked clast with magnetite-bearing veins. D) Close up of C. This close-up shows the magnetite-bearing veins are folded ('swirled') within the clast. Sample spots for the EDS analysis in Figure S5.4 are indicated by red crosses. E) Magnetite-bearing particles surround a small clast.

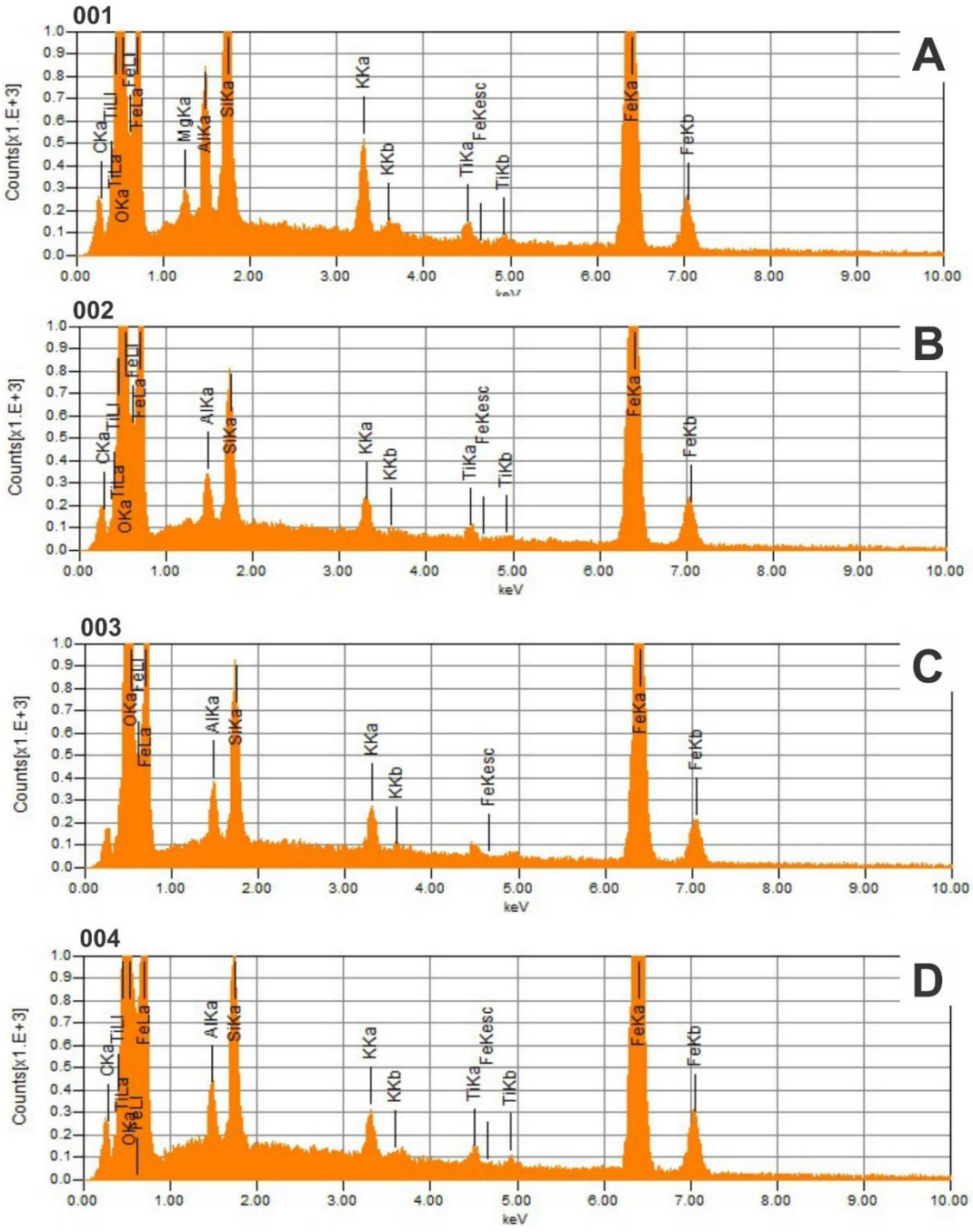

Figure S5.3. EDS-spectra of magnetite-bearing veins in Figure 5.2A (PNG16-142D).

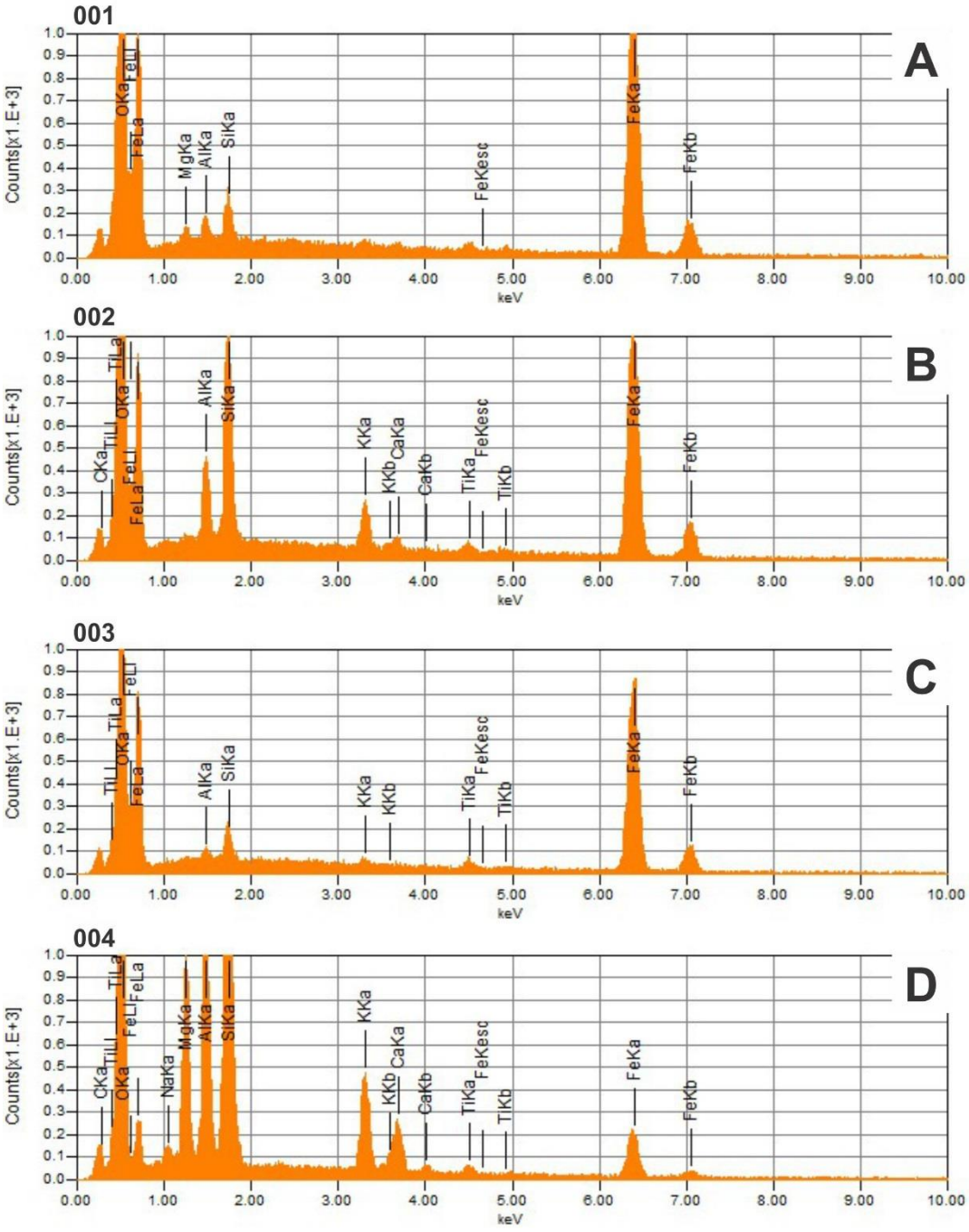

Figure S5.4. EDS-spectra of a magnetite-bearing clast in Figure S5.2D (PNG16-142D).

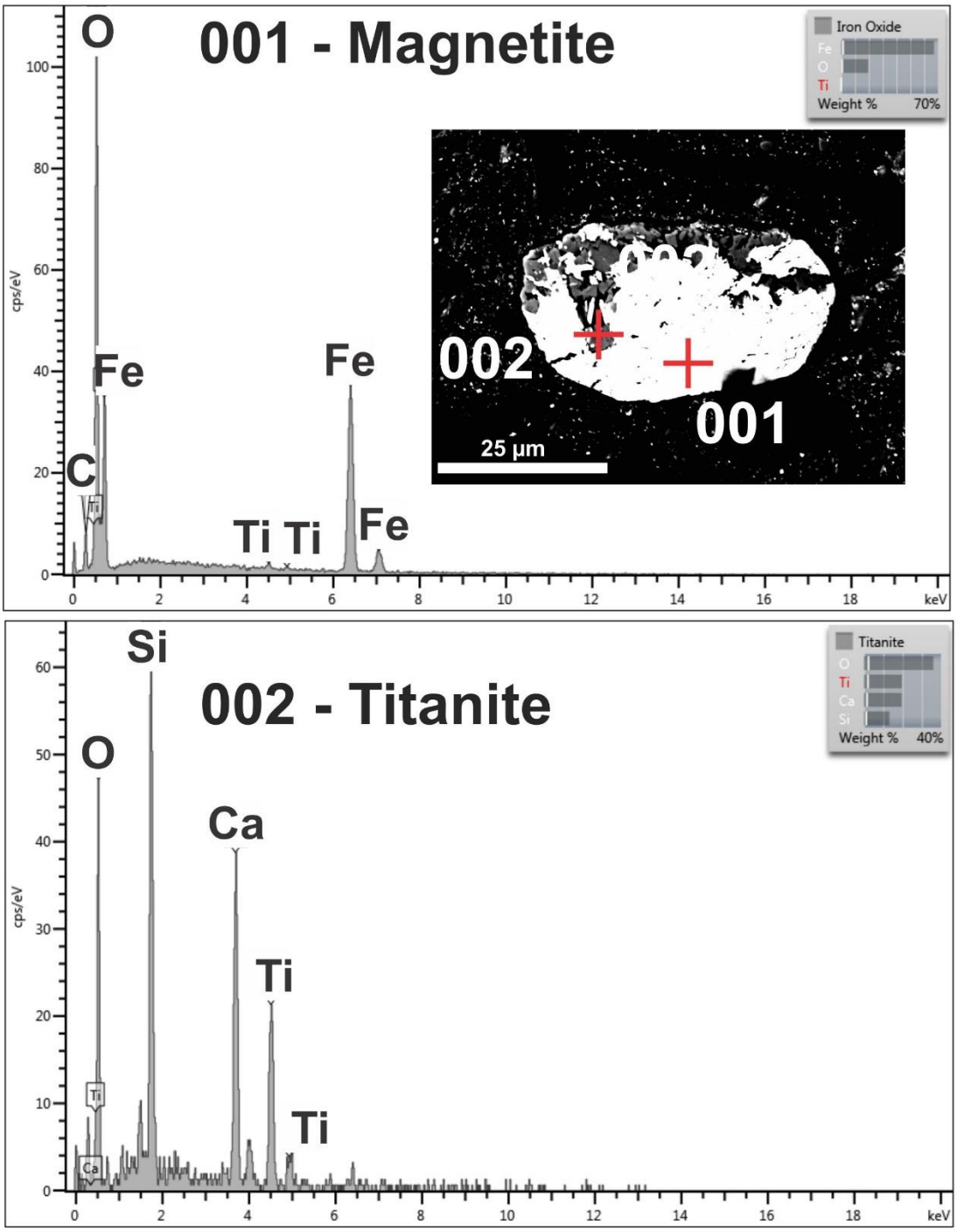

Figure S5.5. EDS analysis of a single magnetite grain in the ultracataclasite matrix (PNG16-142D).

Text S6. TEM Analysis of a Mirror-like Facet on Gabbroic Clast

The hangingwall contact atop the Mai'iu fault truncates cm- to dm-sized pebbles and cobbles in the Gwoira Conglomerate. We analyzed the mirror polish of one fault-truncated dolerite cobble with TEM in order to describe the composition, thickness and grain-size of the shiny, fault-truncated surface, and the origin of striation on these surfaces. A TEM foil was cut perpendicular to the shiny surface and was prepared using a FEI Quanta 3D FEG-SEM with focused ion beam (FIB) at University of Vienna, Department of Lithospheric Research. TEM used a JEOL 2011 STEM equipped with a double-tilt analytical holder and a Gatan MSC digital camera for imaging at the University of New Brunswick, Microscopy and Microanalysis Facility. The results of this method are presented in the main manuscript.

Text S7. Identification of Mineral Phases in Representative Mai'iu Fault Rocks using XRD

A collection of 15 fault rock samples of ultracataclasites, gouges and serpentinite schist were analysed with X-Ray Diffraction by Mark Raven at CSIRO Land and Water Flagship, Mineral Resources Flagship, at the Centre for Australian Forensic Soil Science (CAFSS), in Urrbrae, South Australia. For these, 1.5 g sub-samples were ground for 10 minutes in a McCrone micronizing mill under ethanol. The resulting slurries were oven dried at 60°C then thoroughly mixed in an agate mortar and pestle before being lightly pressed into aluminium sample holders for X-ray diffraction analysis. XRD patterns from the micronized materials showed variable hydration of the interlayer which causes problems with quantification. As the samples did not appear to contain any water soluble phases they were calcium saturated and the data re-analysed. XRD patterns were recorded with a PANalytical X'Pert Pro Multi-purpose Diffractometer using Fe filtered Co Ka radiation, auto divergence slit, 2° anti-scatter slit and fast X'Celerator Si strip detector. The diffraction patterns were recorded in steps of 0.016° 2 theta with a 0.4 second counting time per step, and logged to data files for analysis. Table S7.1 (below) lists the phases that were identified in each sample. These XRD-results are also published in Little et al. (2019).

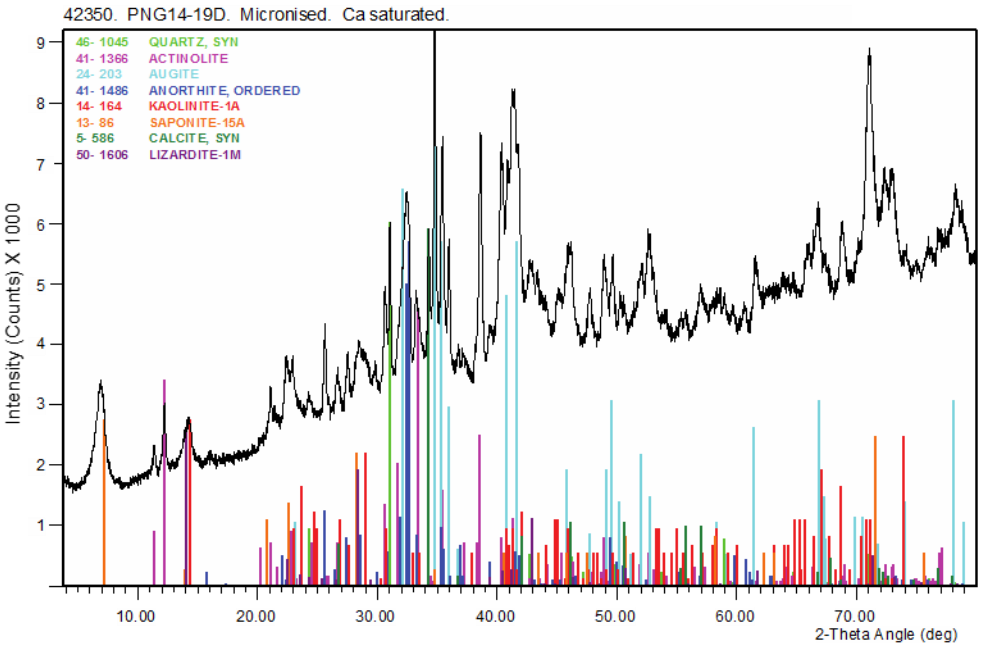
42350. PNG14-19D. Micronised. Ca saturated.
46- 1045 QUARTZ, SYN
41- 1366 ACTINOLITE
24- 203 AUGITE
41- 1486 ANORTHITE, ORDERED
14- 164 KAOLINITE-1A
13- 86 SAPONITE-15A
5- 586 CALCITE, SYN
50- 1606 LIZARDITE-1M
Intensity (Counts) X 1000
2-Theta Angle (deg)

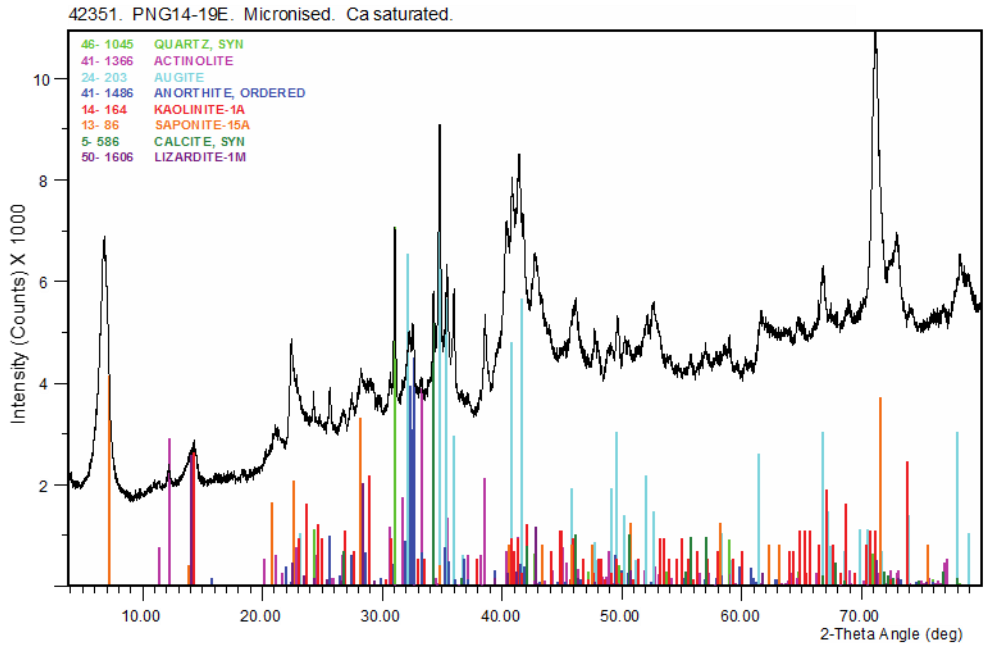
42351. PNG14-19E. Micronised. Ca saturated.
46- 1045 QUARTZ, SYN
41- 1366 ACTINOLITE
24- 203 AUGITE
41- 1486 ANORTHITE, ORDERED
14- 164 KAOLINITE-1A
13- 86 SAPONITE-15A
5- 586 CALCITE, SYN
50- 1606 LIZARDITE-1M
Intensity (Counts) X 1000
2-Theta Angle (deg)

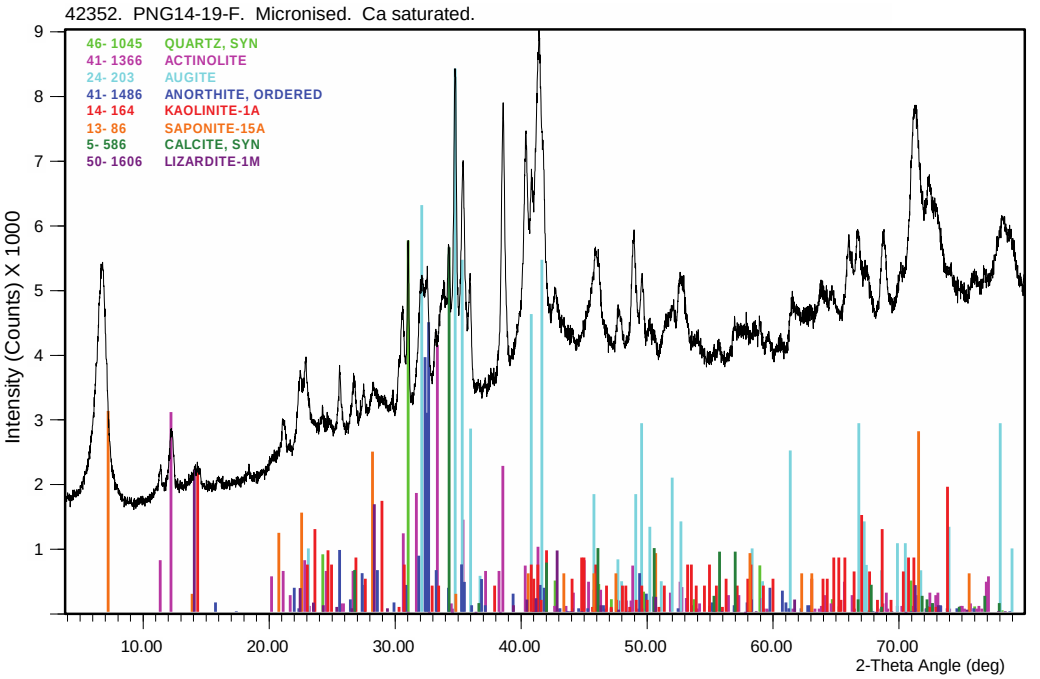
42352. PNG14-19-F. Micronised. Ca saturated.
46- 1045 QUARTZ, SYN
41- 1366 ACTINOLITE
24- 203 AUGITE
41- 1486 ANORTHITE, ORDERED
14- 164 KAOLINITE-1A
13- 86 SAPONITE-15A
5- 586 CALCITE, SYN
50- 1606 LIZARDITE-1M
Intensity (Counts) X 1000
2-Theta Angle (deg)

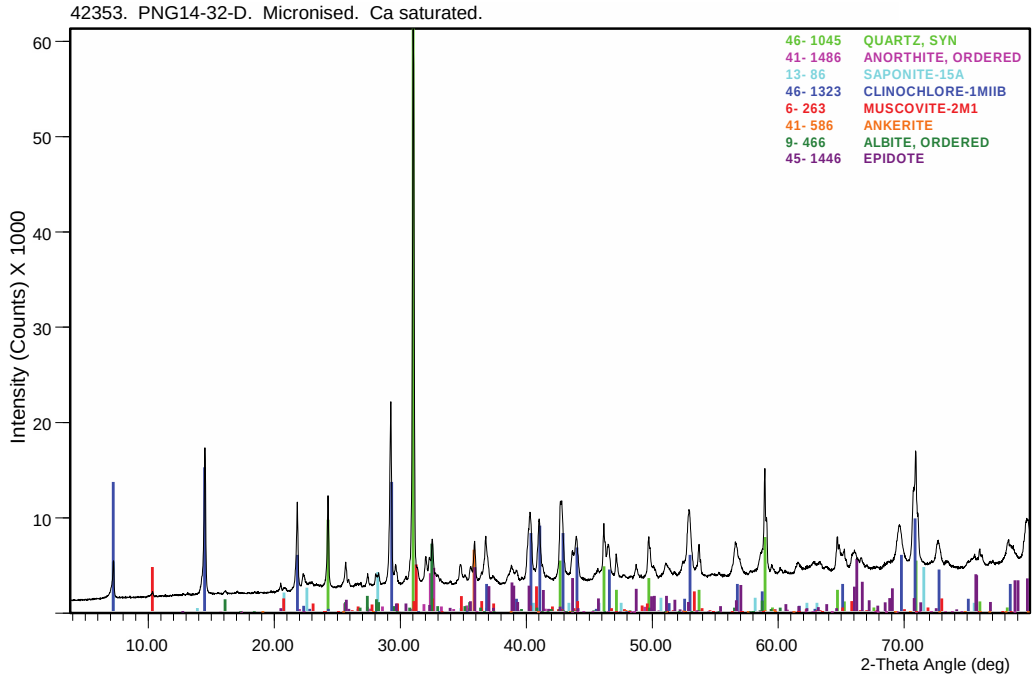
42353. PNG14-32-D. Micronised. Ca saturated.
46- 1045 QUARTZ, SYN
41- 1486 ANORTHITE, ORDERED
13- 86 SAPONITE-15A
46- 1323 CLINOCHLORE-1MIIB
6- 263 MUSCOVITE-2M1
41- 586 ANKERITE
9- 466 ALBITE, ORDERED
45- 1446 EPIDOTE
Intensity (Counts) X 1000
2-Theta Angle (deg)

42354. PNG14-32-E Green. Micronised. Ca saturated.

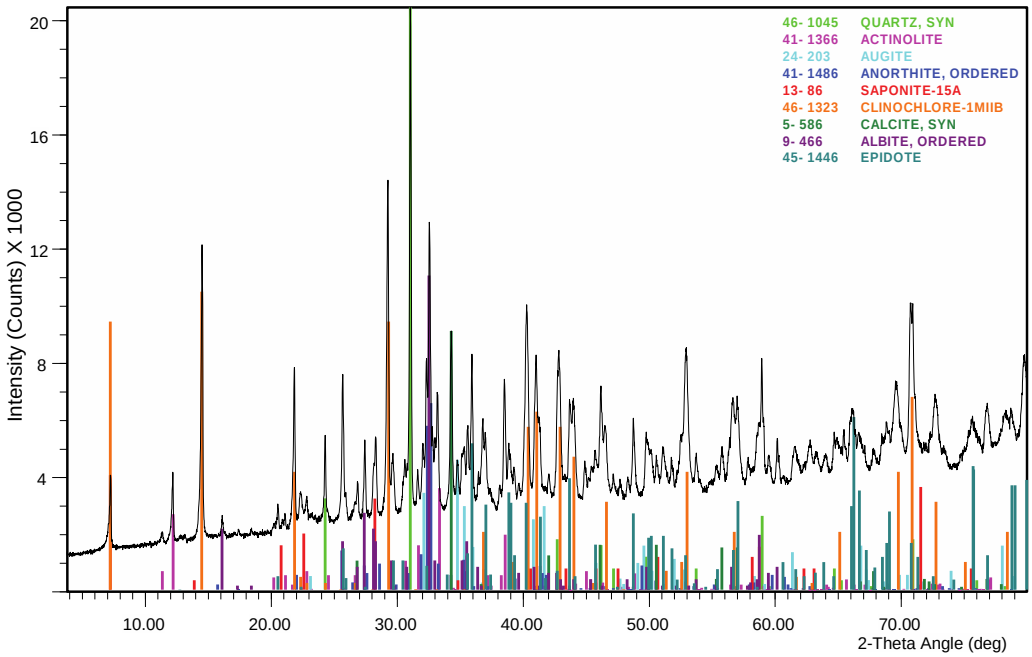

42355. PNG14-32-E Red. Micronised. Ca saturated.

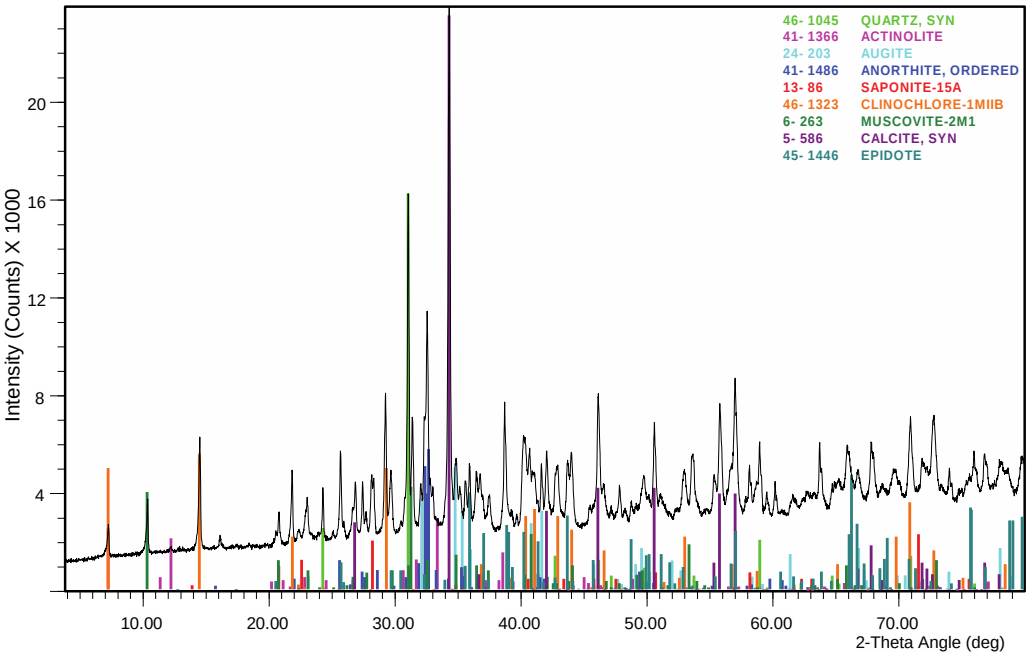

42356. PNG14-32-F. Micronised. Ca saturated.

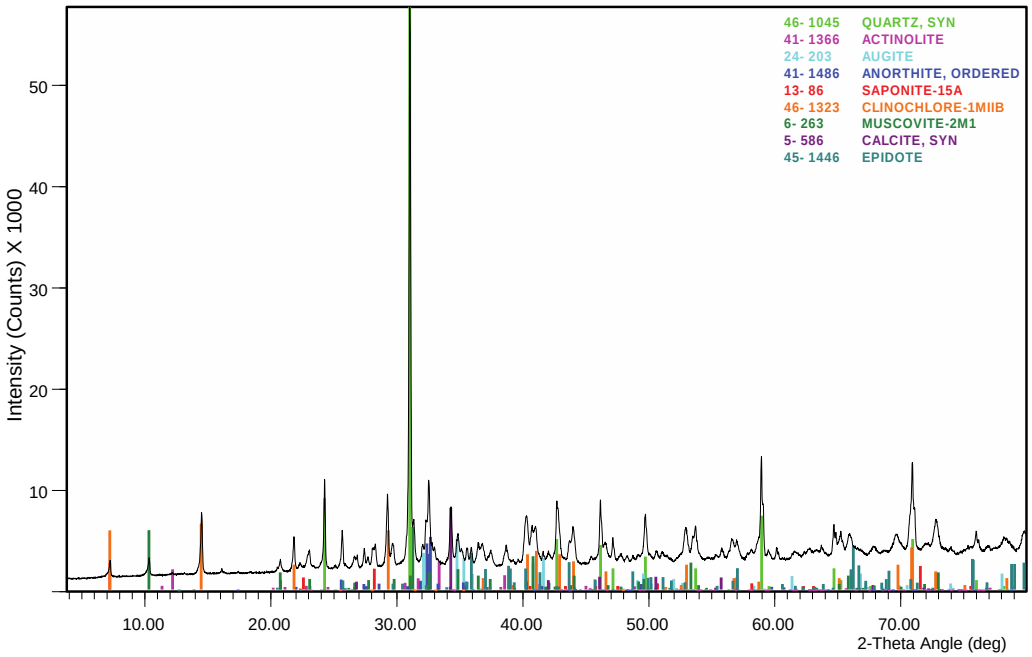

42357. PNG14-33-A. Micronised. Ca saturated.

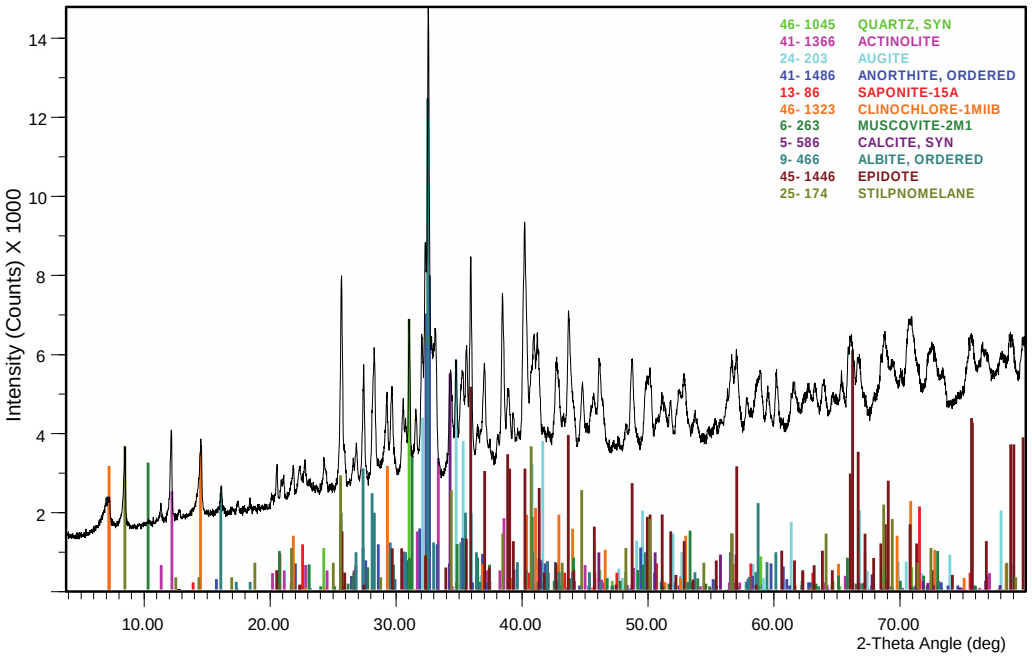

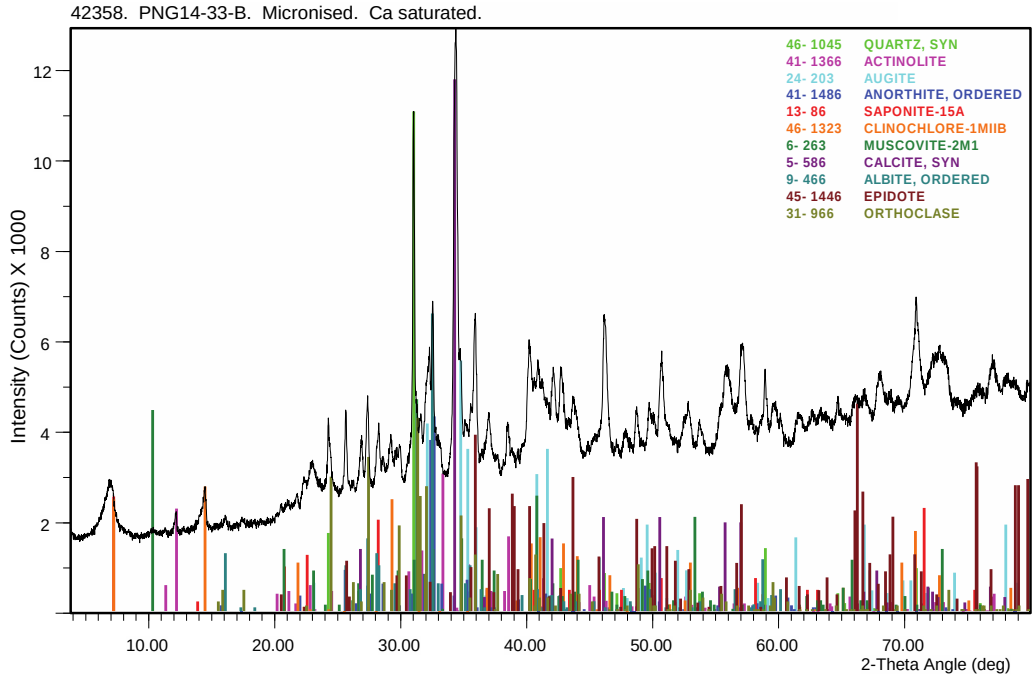
42358. PNG14-33-B. Micronised. Ca saturated.
46- 1045 QUARTZ, SYN
41- 1366 ACTINOLITE
24- 203 AUGITE
41- 1486 ANORTHITE, ORDERED
13- 86 SAPONITE-15A
46- 1323 CLINOCHLORE-1MIIB
6- 263 MUSCOVITE-2M1
5- 586 CALCITE, SYN
9- 466 ALBITE, ORDERED
45- 1446 EPIDOTE
31- 966 ORTHOCLASE
Intensity (Counts) X 1000
2-Theta Angle (deg)

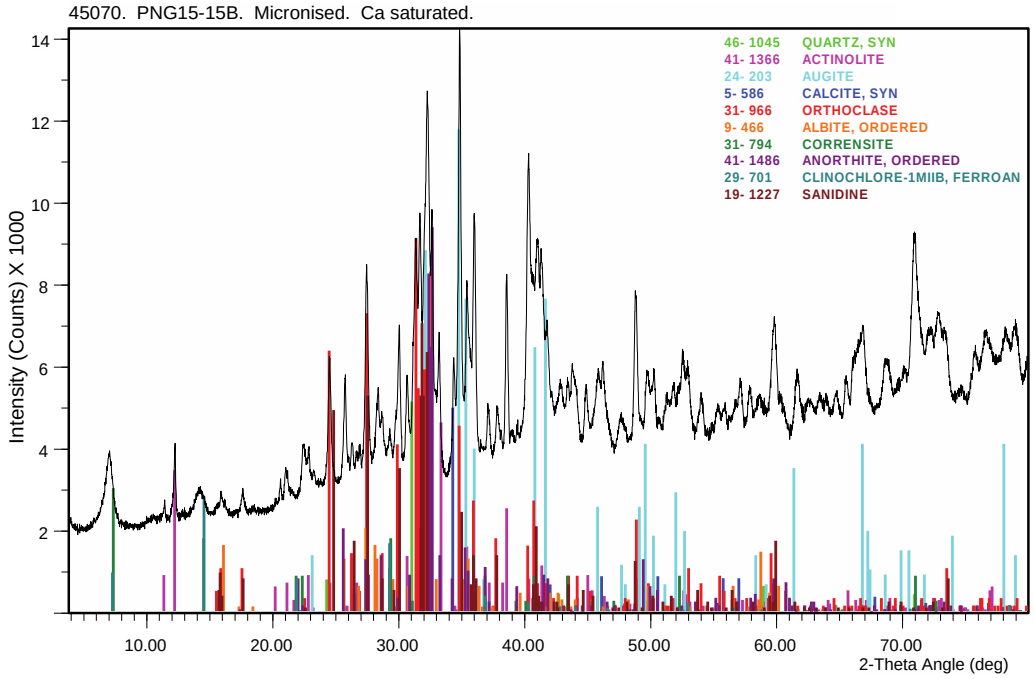
45070. PNG15-15B. Micronised. Ca saturated.
46- 1045 QUARTZ, SYN
41- 1366 ACTINOLITE
24- 203 AUGITE
5- 586 CALCITE, SYN
31- 966 ORTHOCLASE
9- 466 ALBITE, ORDERED
31- 794 CORRENSITE
41- 1486 ANORTHITE, ORDERED
29- 701 CLINOCHLORE-1MIIB, FERROAN
19- 1227 SANIDINE
Intensity (Counts) X 1000
2-Theta Angle (deg)

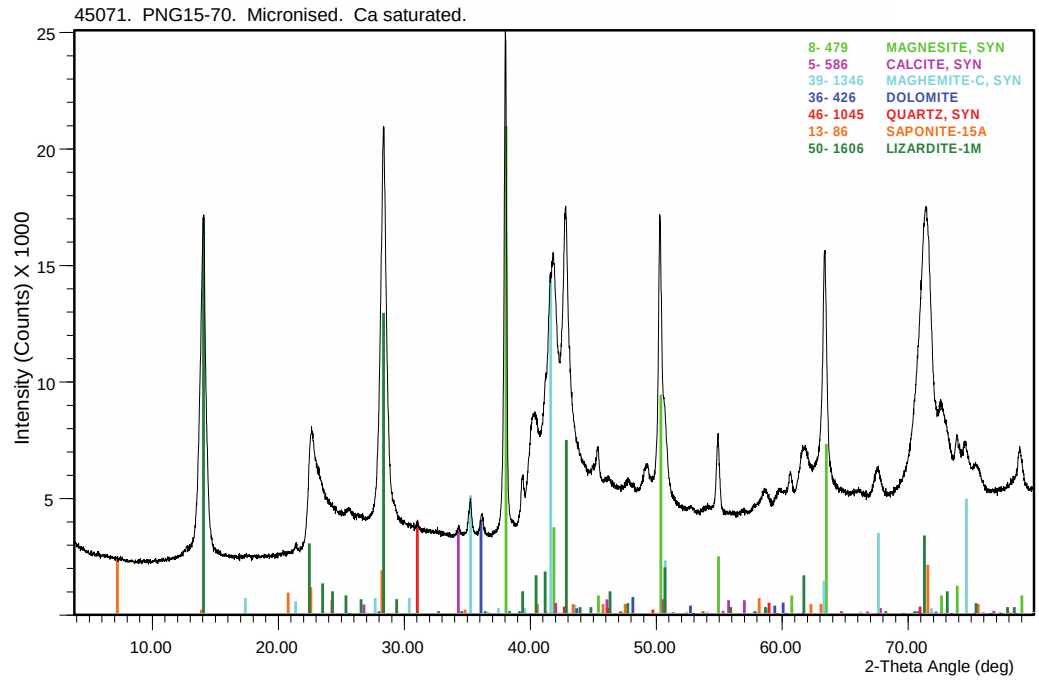
45071. PNG15-70. Micronised. Ca saturated.
8- 479 MAGNESITE, SYN
5- 586 CALCITE, SYN
39- 1346 MAGHEMITE-C, SYN
36- 426 DOLOMITE
46- 1045 QUARTZ, SYN
13- 86 SAPONITE-15A
50- 1606 LIZARDITE-1M
Intensity (Counts) X 1000
2-Theta Angle (deg)

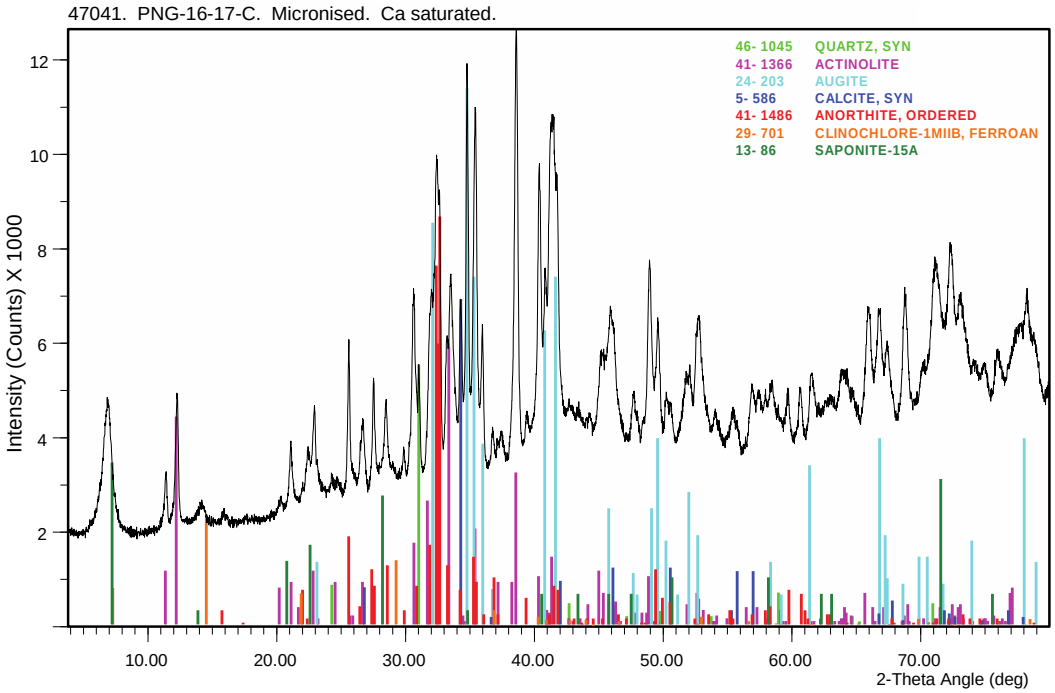
47041. PNG-16-17-C. Micronised. Ca saturated.
46- 1045 QUARTZ, SYN
41- 1366 ACTINOLITE
24- 203 AUGITE
5- 586 CALCITE, SYN
41- 1486 ANORTHITE, ORDERED
29- 701 CLINOCHLORE-1MIIB, FERROAN
13- 86 SAPONITE-15A
Intensity (Counts) X 1000
2-Theta Angle (deg)

47042. PNG-16-30-B. Micronised. Ca saturated.

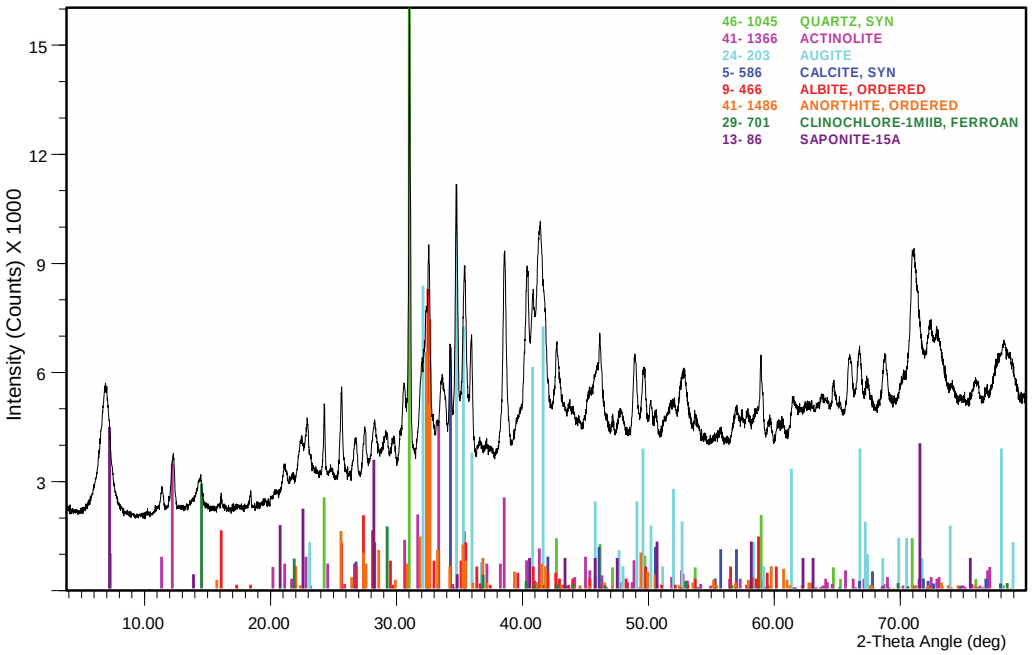

47043. PNG-16-108-G. Micronised. Ca saturated.

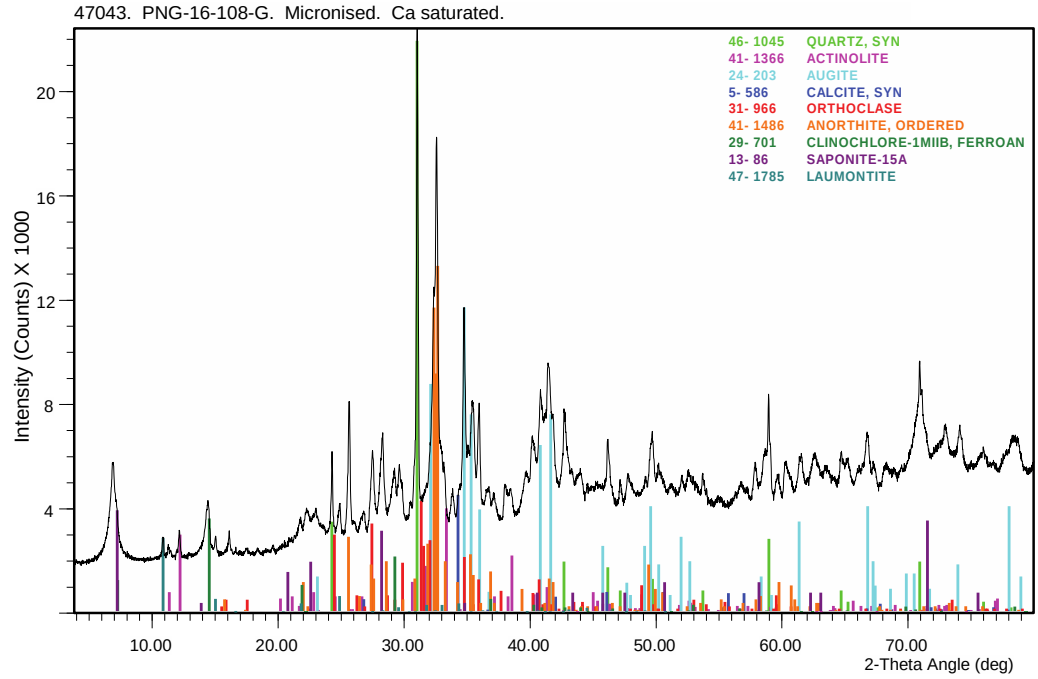

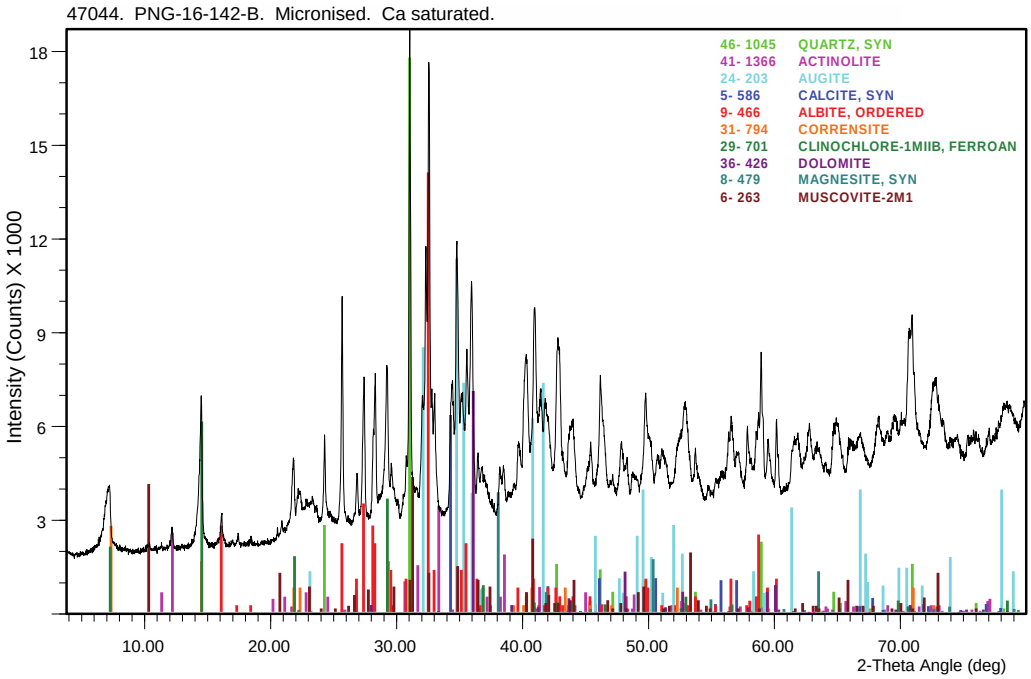

Figure S7.1. Whole rock, Ca-saturated X-ray diffraction patterns.

CSIRO ID	Field Sample No.	Fault Rock Unit	Fault	Degrees South (WGS84) Latitude	Degrees East (WGS84) Longitude
42350	PNG-14-19-D	ultracataclasite	inactive Mai'iu F.	149.44082	-9.82862
42351	PNG14-19-E	gouge	inactive Mai'iu F.	149.44082	-9.82862
42352	PNG-14-19-F	gouge	inactive Mai'iu F.	149.44082	-9.82862
42353	PNG-14-32-D	gouge	Biniguni Splay F.	149.38230	-9.67883
42354	PNG-14-32-E-g	gouge	Biniguni Splay F.	149.38230	-9.67883
42355	PNG-14-32-E-r	gouge	Biniguni Splay F.	149.38230	-9.67883
42356	PNG-14-32-F	gouge	Biniguni Splay F.	149.38230	-9.67883
42357	PNG-14-33-A	gouge	active Mai'iu F.	149.35904	-9.67726
42358	PNG-14-33-B	gouge	active Mai'iu F.	149.35904	-9.67726
45070	PNG-15-50-B	ultracataclasite	active Mai'iu F.	149.28669	-9.67778
45071	PNG-15-70	serpentininite	active Mai'iu F.	149.61246	-9.82863
47041	PNG-16-17-C	ultracataclasite	inactive Mai'iu F.	149.44028	-9.82967
47042	PNG-16-30-B	gouge	inactive Mai'iu F.	149.44059	-9.82499
47043	PNG-16-108-G	gouge	active Gwoira F.	149.46712	-9.77150
47044	PNG-16-142-B	gouge	active Mai'iu F.	149.35913	-9.67729

CSIRO ID	Notes
42350	Near lower transition into foliated cataclasite unit
42351	Upper of two gouge layers. Light grey, 1.5 cm thick
42352	Lower of of two gouge layers. Dark grey, 17 cm thick
42353	Porphyroclastic gouge layer 1m thick. Greenish grey.
42354	Green-colored gouge in variegated gouge layer >1 m thick
42355	Maroon-colored gouge in variegated gouge layer >1 m thick
42356	White-colored gouge in variegated gouge layer >1 m thick
42357	Lower of two gouge layers. Green, 10 cm thick.
42358	Upper of two gouge layers. Grey, 5 cm thick.
45070	Exhumed pavement surface at base of scarp
45071	Serpentinite fault slice structurally atop exhumed Mai'iu fault near Mt Masasoru
47041	Same fault outcrop as location PNG-14-19
47042	Upper gouge layer. Grey, 2 cm thick.
47043	Collected 21 cm below PDS
47044	Upper of two gouge layers. Purple-grey, 5 cm thick. Same as PNG-14-33-B

CSIRO ID	Whole Rock Mineralogy
42350	Corrensite/Saponite, Augite, Amphibole, Plagioclase, Kaolin, Calcite, Quartz
42351	Corrensite/Saponite, Augite, Amphibole, Plagioclase, Kaolin, Calcite, Quartz
42352	Corrensite/Saponite, Augite, Amphibole, Plagioclase, Kaolin, Calcite, Quartz
42353	Chlorite, Quartz, Epidote, Plagioclase, Mica, Titanite
42354	Chlorite, Plagioclase, Amphibole, Epidote, Quartz, Calcite, Titanite
42355	Calcite, Mica, Plagioclase, Epidote, Chlorite, Quartz, Titanite, Hematite, Amphibole
42356	Quartz, Chlorite, Mica, Plagioclase, Calcite, Epidote, Titanite, Amphibole, Hematite
42357	Plagioclase, Epidote, Amphibole, Corrensite/Saponite, Chlorite, Stilpnomelane, Titanite, Calcite, Quartz, K-feldspar
42358	Corrensite/Saponite, Calcite, Montmorillonite, Plagioclase, Epidote, K-feldspar, Amphibole, Quartz, Dolomite/Ankerite, Chlorite, Mica
45070	Corrensite, K-feldspar, Plagioclase, Amphibole, Augite, Chlorite, Calcite, Quartz
45071	Serpentine (Lizardite), Magnesite, Saponite, Quartz, Calcite, Dolomite/Ankerite, Maghemite
47041	Saponite, Amphibole, Plagioclase, Augite, Calcite, Chlorite, Quartz
47042	Saponite, Amphibole, Plagioclase, Augite, Calcite, Chlorite, Quartz
47043	Saponite, Amphibole, Plagioclase, Augite, Quartz, Chlorite, K-feldspar, Laumontite, Calcite, Magnesite
47044	Saponite, Plagioclase, Augite, Amphibole, Chlorite/Corrensite, Dolomite/Ankerite, Quartz, Calcite, Mica, Magnesite

Table S7.1. Mineral Phases in Mai'iu fault rocks determined by X-Ray Diffraction.

Text S8. Bulk Whole rock Major Element Compositions of Mafic Fault Rocks Using XRF

Whole rock major element concentrations (Table S8.1) were determined based on X-ray fluorescence (XRF) spectrometry with a SPECTRO X-LAB 2000 at the Department of Earth & Ocean Sciences, University of Waikato, on fused glass disks cast using a 10:1 flux ratio in lithium borate flux. Trace element concentrations were measured with a Thermo-Scientific Element2 sector-field inductively coupled plasma mass spectrometry (ICP-MS) at the School of Geography, Environment and Earth Sciences, Victoria University Wellington. A gravimetric multi-element synthetic mixture was employed to calibrate the unknowns and to monitor for drift. The accuracy of the unknowns was determined with a secondary reference material (AGV-2).

Sample#	PNG-16-17_2D	PNG-16-17z	PNG-14-19e	PNG-14-19F
Formation	Goropu Metabasalt	Goropu Metabasalt	Goropu Metabasalt	Goropu Metabasalt
Sequence	Non-Mylonitic	Mafic Mylonite	Gouge	Gouge
wt.%				
SiO2	45.56	48.84	42.93	43.80
TiO2	1.33	1.63	0.86	0.81
Al2O3	14.74	12.32	11.45	11.16
Fe2O3	11.45	11.95	11.23	10.84
MnO	0.19	0.22	0.22	0.23
MgO	7.60	6.75	16.80	16.58
CaO	11.49	9.37	7.54	8.40
Na2O	2.08	2.96	0.94	0.90
K2O	0.14	0.04	0.08	0.03
P2O5	0.14	0.19	0.11	0.11
SO3	0.07	0.17	0.07	0.13
SrO (Sr - PPM)	82.00	271.00	53.00	71.00
BaO (Ba - PPM)	94.00	81.00	42.00	45.00
CO2 (%)	4.24	4.91	7.04	6.27
Total (%)	99.04	99.38	99.28	99.26
ppm				
Cr	309.38	200.54	1303.54	1346.79
Ni	67.49	51.19	709.16	758.27
Cs	0.05	0.03	0.17	0.10
Ba	17.30	21.11	23.80	16.47
Rb	2.86	0.27	1.69	0.48
Sr	140.70	267.79	96.00	112.01
Pb	0.28	1.01	2.08	2.28
Th	0.21	0.56	0.79	0.75
U	0.10	0.18	0.21	0.20
Zr	162.60	103.73	127.05	123.87
Nb	4.80	6.65	2.35	2.27
Hf	2.16	2.81	1.72	1.67
Ta	0.45	0.63	0.28	0.26
Y	22.08	23.65	17.23	17.11
V	308.84	290.29	207.72	197.23
Sc	41.95	33.89	29.47	29.54
Co	51.98	36.24	72.64	74.47
Cu	107.17	99.43	93.24	95.15
Zn	92.07	172.19	74.86	76.38
Ga	19.17	16.57	13.00	12.10
La	4.67	6.19	4.64	4.54
Ce	11.89	15.77	10.93	10.66
Pr	1.79	2.34	1.54	1.51
Nd	9.34	11.42	7.71	7.50
Sm	3.04	3.36	2.28	2.32
Eu	2.29	1.26	1.59	1.57
Gd	3.66	4.03	2.75	2.77
Tb	0.68	0.79	0.52	0.52
Dy	4.41	4.89	3.42	3.38
Ho	0.91	1.02	0.72	0.71
Er	2.67	2.98	2.12	2.14
Tm	0.38	0.42	0.31	0.31
Yb	2.34	2.67	1.93	1.94
Lu	0.37	0.41	0.29	0.30
Au	0.22	0.36	0.13	0.16

Table S8.1. Chemical analyses of Mai'iu fault rock samples comprising a non-mylonitic, almost undeformed Goropu Metabasalt, a mylonite and two gouge samples. Note, the increase in Cr and Ni in the gouge sample relative to the other samples (highlighted in yellow). Also compare with Smith (2013).

Text S9. Chlorite and Albite Compositions Using EPMA

Wavelength dispersive analysis of chlorite and albite was carried out on a JEOL electron microprobe at the School of Geography, Environmental and Earth Science, Victoria University of Wellington. We used an acceleration voltage of 15 kV and a sample current of 12 nA. Synthetic and natural mineral standards were used for calibration comprising the elements Si, Al, Mg, Mn, Fe, Zn, Ni, Cr, Na, K and Ca for chlorite and Si, Al, Mg, Mn, Fe, Ni, Ti, Na, K and Ca for plagioclase (albite). Errors in the raw data were reduced by ZAF correction. The results from this analysis can be found in Table S9.1 ('Albite_EPMA_Data.xlsx') and Table S9.2 ('Chlorite_EPMA_data.xlsx') that are uploaded as separate files. The former shows the results for albite; and latter shows the results of all analysed chlorite grains in the mafic mylonites, foliated cataclasites and chlorite veins.

Table S9.1 (Albite_EPMA_Data.xlsx). Feldspar compositions in mafic mylonites and foliated cataclasites.

Table S9.2 (Chlorite_EPMA_data.xlsx). Chlorite compositions, calculated temperatures and proportions of chlorite to swelling component (X) in analysed mylonite, foliated cataclasites and chlorite veins.